



UNIVERSITY  
OF TRENTO - Italy

---

Department of Materials Engineering  
and Industrial Technologies

Doctoral School in Materials Science and Engineering  
XXIV cycle

# **Coating for energetic and sensing applications**

PhD Candidate: Marta Buffa

Tutors:

Prof. Gianantonio Della Mea

Prof. Alberto Quaranta

April 2012



# Contents

OVERVIEW .....	1
----------------	---

## CHAPTER 1

Wavelength Shifters and Luminescent Solar Concentrators .....	3
---	---

1.1 Introduction .....	3
------------------------	---

1.2 The Italian market.....	3
-----------------------------	---

1.3 The sun and its potential.....	5
------------------------------------	---

1.4 Types of photovoltaic cells.....	7
--------------------------------------	---

1.4.1 Single –crystal and polycrystalline solar cells.....	7
--	---

1.4.2 Thin film solar cells .....	8
-----------------------------------	---

1.4.3 Cadmium telluride solar cell.....	9
---	---

1.4.4 CIGS.....	9
-----------------	---

1.4.5 a-Si .....	10
------------------	----

1.4.6 Thin film Si .....	10
--------------------------	----

1.4.7 III-V Semiconductors.....	11
---------------------------------	----

1.4.8 Photoelectrochemical solar cells.....	11
---	----

1.5 Optical solar concentrators.....	12
--------------------------------------	----

1.6 LSC.....	13
--------------	----

1.7 WLS.....	16
--------------	----

Bibliography .....	18
--------------------	----

## Contents

CHAPTER 2	
Experimental.....	23
2.1 Introduction .....	23
2.2 Parylene Production.....	23
2.3 Chemical characterisation process .....	25
2.3.1 Fourier Transformate InfraRed.....	25
2.3.2 XRD .....	28
2.4 Optical characterization techniques.....	30
2.4.1 Spectrophotometer .....	31
2.4.2 Fluorescence.....	32
2.4.3 Ocean Optics Spectrometer .....	34
2.5 Physical analysis .....	34
2.5.1 Atomic force microscopy (AFM).....	34
2.6 Electrical measurements.....	38
2.6.1 Cell Preparation .....	41
2.6.2 Integrating sphere .....	42
Bibliography .....	44

## CHAPTER 3

Materials.....	47
3.1 <i>Polysiloxanes: properties and synthesis</i> .....	47
3.1.1 First reaction.....	48
3.1.2 Second reaction.....	49
3.1.3 Third reaction .....	50
3.2 <i>Parylene</i> .....	52
3.2.1 Parylene types .....	52
3.2.2 Properties of parylene.....	53
3.3 <i>Fluorinated Polyimide</i> .....	66
3.3.1 Properties .....	66
3.3.2 Two-step polymerisation.....	68
3.3.3 Formation of the polyamic acid.....	69
3.3.4 Secondary reactions and other factors .....	72
3.3.5 Chemical imidisation and poly iso-imides .....	74
3.3.6 Mechanisms.....	75
3.4 <i>Dyes</i> .....	78
3.4.1 Characteristics .....	78
3.4.2 Coumarins.....	79
3.4.3 Lumogen dyes.....	81
3.4.4 BBOT .....	83
3.4.5 3 Hydroxy flavone.....	84
3.4.5.1 The molecule .....	84

## Contents

<i>3.5 Lanthanide nanoparticles</i> .....	91
3.5.1 Lanthanides properties.....	91
3.5.2 Up conversion.....	96
3.5.3 Down conversion .....	96
3.5.4 NaGdF <sub>4</sub> :Eu <sup>3+</sup> .....	98
<i>Bibliography</i> .....	100
<b>CHAPTER 4</b>	
<b>Results</b> .....	109
<i>4.1 Introduction</i> .....	109
<b>First Part</b> .....	110
<i>4.2 Parylene based samples</i> .....	110
4.2.1 Parylene: deposition parameters .....	112
4.2.2 Parylene N and BBOT.....	113
4.2.3 IR-analysis Parylene + BBOT .....	116
4.2.4 Optical of parylene C + 3HF .....	118
4.2.5 Deposition parameters.....	119
4.2.6 Evaporation of Lumogen yellow 083 .....	121
<i>4.3 Fluorinated polyimide</i> .....	124
4.3.1 Polyimide+3HF.....	125
4.3.2 Other dyes in Fluorinated Polyimides .....	127
<i>4.4 Polysiloxane</i> .....	130
4.4.1 Optical characterizations of BBOT-containing polysiloxanes .....	130

## Contents

4.4.2 Polysiloxane containing 3HF .....	132
4.4.3 3HF in polysiloxane, under Pt catalysis.....	133
4.4.4 3HF in polysiloxane, under Sn catalysis .....	140
4.4.5 3HF in moisture-cured polysiloxane .....	143
4.4.6 Polysiloxane doped with Lumogen.....	146
<i>4.5 Lumogen red in LSC .....</i>	<i>148</i>
<i>4.6 Choosing dye and matrix: summary .....</i>	<i>155</i>
<b>Second part.....</b>	<b>157</b>
<i>4.7 Solar measurements .....</i>	<i>157</i>
<i>4.8 WLS .....</i>	<i>157</i>
4.8.1 3HF embedded in parylene .....	158
4.8.2 3HF embedded in fluorinated polyimide.....	159
4.8.3 3HF embedded in polysiloxane .....	160
<i>4.9 LSC.....</i>	<i>161</i>
<i>4.10 Production procedure of nanophosphors.....</i>	<i>173</i>
4.10.1 Preparation.....	173
4.10.2 The coupling of Gd and Eu.....	174
<i>Bibliography .....</i>	<i>180</i>

## Contents

### CHAPTER 5

#### Conclusions and Further Work..... 189

##### *5.1 Conclusions..... 189*

##### 5.1.1 WLS..... 190

##### 5.1.2 LSC..... 191

##### 5.1.3 Further work..... 192

##### *Bibliography..... 194*

### Appendix A

#### INFRARED ANALYSIS ..... 195

##### *Parylene N..... 195*

##### *Parylene C..... 198*

##### *Polysiloxane..... 201*

##### *3-Hydroxyflavone..... 202*

### APPENDIX B

#### UV-Vis OPTICAL SPECTRA ..... 206

### APPENDIX C

#### UV-Vis SPECTRA OF LUMOGEN DYES IN POLYSILOXANE..... 212

##### *Bibliography..... 217*



# OVERVIEW

---

The aim of this work is the development of materials for the production and enhancements of photovoltaic (PV) devices.

The efficiency of a PV device can be enhanced focusing on the solar cell, optimizing its shape, materials or architecture, or focusing on the incoming radiation, altering its spectrum in order to make it more efficiently exploited by the cell or increasing, by means of a concentrating system, the area over which light is collected. This work focuses on the production and testing of materials for the latter approach, luminescent solar concentration (LSC) and wavelength shifting (WLS).

In the first chapter an overview of the state of art in WLS and LSC systems is provided, along with a general introduction to the history and technology of PV devices.

The second chapter presents the instruments used in this work, in order to make the Reader aware of the potential and limitations of the performed measurements.

The third chapter deals with the properties and production of the materials considered in the present study, namely luminescent species, matrices and rare-earth nanoparticles.

In the fourth chapter experimental results are reported. The interactions between matrices and dyes and their implications are

## *Overview*

discussed. The tests performed applying the most promising matrix-dye combinations to actual solar cells are then described.

The fifth chapter summarizes the project, providing conclusions and cues for future work.

# CHAPTER 1

## Wavelength Shifters and Luminescent Solar Concentrators

---

### *1.1 Introduction*

Solar power is undoubtedly the most abundant source of energy on Earth. The exploitation of it, however, is not trivial. In this chapter an overview of the social and economical aspects of photovoltaic power generation is given, along with a brief outline of the functioning and laboratory-measured efficiency of commercially available solar cells. An introduction to concentrating systems and, in particular, luminescent solar collectors and wavelength shifting materials is also provided.

### *1.2 The Italian market*

The energetic problem is a worldwide critical issue. In Italy, in particular, the increasing demand for hydrocarbon fuels and the competition for supplies represent a high disadvantage for the economy. Italy also makes an intensive use of gas, which is arguably the most expensive among non-renewable energy sources.

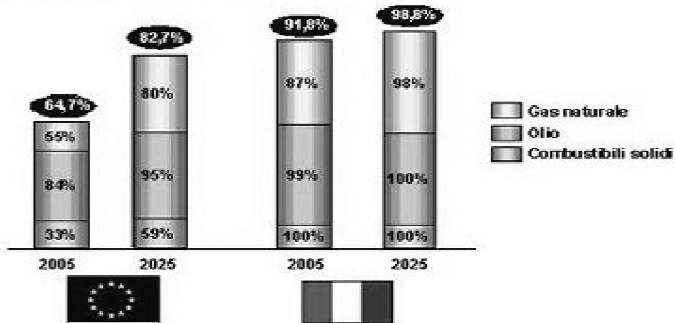
In figure 1.1 is represented the breakdown of energy generation in Italy and the rest of Europe in 2005 and the forecast for 2025. The

huge dependence of Italy on imported fuel is an economical and social risk [wMAE 2011].

More than 90% of the energy currently consumed in Italy is produced from imported sources and this dependence is set to become basically complete by the year 2025. As the increasing demand for imported energy sources is also likely to drive their prices up, the need to tackle this problem is apparent.

### Dipendenza dalle fonti primarie in Italia e in Europa

Rapporto fra import netto per fonte e consumo lordo



**Figure 1.1: Comparison between Europe and Italy in the trend of the dependency on energy imported from foreign countries [WMAE 2011]**

Renewable (i.e. naturally replenished) energy sources include sunlight, wind, biomasses, tides and geothermal. In compliance with the Kyoto protocol (1997) [wKYO 2011] greenhouse gas emissions should be capped so as to prevent dangerous anthropogenic interference with the climate system, which implies that alternatives should be found to fossil fuels.

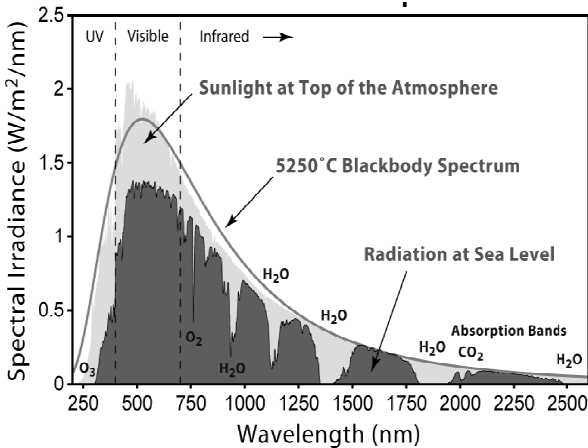
For this reason renewable energies have been gaining ground all over the world in recent years. Indeed, one of their advantages is that power production can be centralized or local, eliminating the need for sizable high-voltage transmission lines [GHAU 06; MOHA 09].

The most powerful renewable energy is hydroelectric, but it requires a large amount of water, a sizable drop in elevation, and often a valley to flood. Geothermal can be meaningfully exploited only in sparse locations. Tides are suitable only where the difference between high and low tide is very large. Wind is a discontinuous source and is available in sizable quantity only in selected places. Biomasses produce CO<sub>2</sub>. Then comes solar power, which is the subject of this thesis.

### *1.3 The sun and its potential*

The intensity of the solar radiation on Earth is about 1353 kW/m<sup>2</sup> (solar constant). Solar radiation reaches the solar photosphere, by and large, with a black-body spectrum corresponding to a temperature of around 6000 K. When the radiation traverses the atmosphere it is attenuated by continuous reflection from air molecules, aerosols, dust, and by absorption by oxygen and ozone, water vapour, and carbon dioxide. The spectrum measured on the surface of the Earth is shown in figure 1.2. The distribution of solar radiation on Earth surface can be found in IEC 60904-3, air mass AM=1.5. Other factors influencing the strength of the solar radiation on Earth surface are latitude, altitude, season, and atmospheric conditions; for example the radiation incident on a horizontal surface is on average 700-1000 kWh/m<sup>2</sup> in northern Europe, 900-

1300 kWh/m<sup>2</sup> in central Europe, 1300-1800 kWh/m<sup>2</sup> in southern Europe and 1800-2300 kWh/m<sup>2</sup> at the equator.



**Figure 1.2: Sunlight spectrum at the top of atmosphere and at ground level, compared to that of a black body at 5250 °C. The gaps in spectrum are due to absorption by chemical species in the atmosphere. [wSPEC 2011]**

It must be remarked that a few limiting factors rule out the possibility that the energetic problem may be solved solely through photovoltaic generation:

- High extension of used terrain
- The discontinuity in the production of power and the problem related to network managing
- The high cost of the semiconductors necessary to produce solar cells.

PV generation, however, can help the daily economy of single or isolated buildings. For all these reasons it is desirable to develop simple and low-cost PV systems.

### *1.4 Types of photovoltaic cells*

Various generations of solar cells have been proposed, from the first silicon cells to multijunction to DSSC; every type has some unique characteristics that make it useful in different situations. This technology is not yet mature because the efficiency is still too low to be economically viable without public subsidization.

#### *1.4.1 Single –crystal and polycrystalline solar cells*

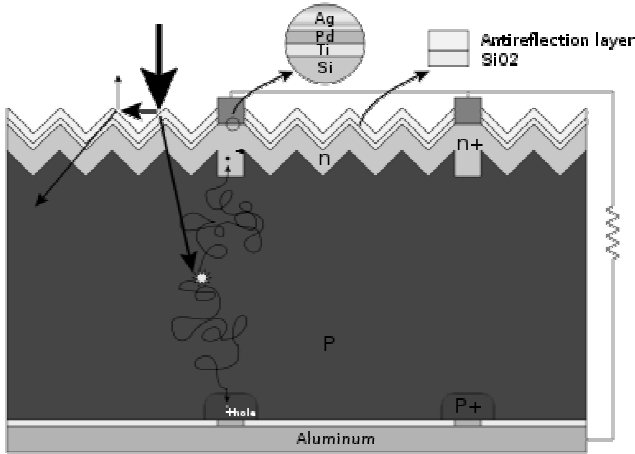
In the mid -50s Chapin, Fuller and Pearson developed the first silicon solar cell that had an efficiency of 6% [KAZM 97].

This type of solar cell is the most common even today; the record laboratory-measured efficiency is 24.7% [GREE 2001], but the crystalline silicon solar cells of commercial use have an efficiency of about 15 % [SHAH 99]

Si solar cells are currently most common because the mature sector of silicon for semiconductors is capable of delivering good grade components.

A sizable reduction in cost for the mature technology of crystalline silicon can be achieved only increasing the manufacturing volume. From the manufacturers' point of view this is subject to the availability of a stable supply of special solar-cell grade silicon, and from the market's point of view this is not actually easy to achieve [GUHA 2000].

This type of cell consists of a layer of antireflective material, one of silica and a silicon bulk that is doped n+ on one side and p+ on the other.



**Figure 1.3: Representation of a typical silicon solar cell.**

### 1.4.2 Thin film solar cells

The so-called second generation photovoltaic devices consist of thin-film materials such as amorphous silicon (a-Si), cadmium telluride (CdTe), copper indium gallium diselenide (CIGS), and thin-film crystalline silicon. These materials can be deposited even on large surfaces. These types of solar cells were mainly developed to reduce manufacturing costs, as the materials can be deposited onto large surfaces (which is beneficial for volume production) and there is no need to process and assemble individual cells. Film semiconductor materials generally have much higher an absorption coefficient than silicon, and therefore a semiconductor layer is



required typically of no more than 1  $\mu\text{m}$  in thickness, which is 100-1000 times less than for Si. The amount of expensive semiconductor material is thus reduced or, equivalently, more expensive semiconductors can be used in thin films. The majority of film panels have significantly lower conversion efficiencies, lagging behind silicon by two to three percentage points.

#### *1.4.3 Cadmium telluride solar cell*

Cadmium telluride solar cells use a cadmium telluride (CdTe) thin film to absorb and convert sunlight into electricity. Cadmium telluride is easy to deposit with thin film techniques and has a nearly optimal band gap (about 1.5 eV). The record efficiency for this type of cells has levelled out at 16.5% since 2001 [WUKE 01]. Wu produced a cell with 16.5% efficiency using advanced front TCO material that made possible a better light absorption, being more conductive than previous cells. The presence of cadmium is somewhat controversial, as its toxicity is at odds with the supposed environmental friendliness of PV power generation. However, production plants for commercial presentation of the CdTe cells are being built, and the expected module efficiencies are in the range of 8 to 9% [SHAH 99].

#### *1.4.4 CIGS*

Copper indium diselenide (CIS) or CIGS, when gallium is added, is perhaps the most promising thin film material at the moment. It holds the record laboratory efficiency of 18.8% among thin film materials [GREE 01] and shows excellent stability. Small amount of cadmium and selenium are present also in the CIGS solar cell, so the concerns associated with CdTe apply, to some extent, to the CIGS

technology as well. Traditional methods of fabrication involve vacuum processes including co-evaporation and sputtering.

### *1.4.5 a-Si*

Amorphous silicon (a-Si or  $\alpha$ -Si) is the non-crystalline allotropic form of silicon. It can be deposited in thin films at low temperatures onto a variety of substrates, offering some unique capabilities for a variety of electronics.

a-Si has been used as a photovoltaic solar cell material for devices which require very little power, such as pocket calculators, because their lower performance (compared to traditional c-Si solar cells) is more than offset by their relative simplicity and low cost.

The main problem with a-Si devices is the degradation in efficiency due to the Stabler-Wronski effect, and stabilized efficiencies of only 4-5% have been obtained for single junction cells (GREE 03). However, decreasing the thickness of the active a-Si layer can enhance the stability of the device. The best-performing commercial a-Si cells utilise a stacked three-layer structure with stabilized efficiencies of 6.4% (GREE 03). The three-junction concept also enables the tuning of the band gap of individual layers to achieve higher efficiencies. A three-junction a-Si tandem-cell technology utilizing a-SiGe alloys in the two lower junctions holds the confirmed record module efficiency of 10.4% (GREE 01).

### *1.4.6 Thin film Si*

One way to reduce the amount of Si in solar cell is to use optical confinement (light trapping). This idea is utilized in the thin film crystalline silicon technology. Amorphous silicon as used in solar

cells is actually a silicon-hydrogen alloy containing 20-30% hydrogen. When a crystalline Si layer with a flat surface is deposited on a Lambertian reflector surface the thickness of the Si layer can be reduced, typically to 5-50  $\mu\text{m}$ . Such a thin Si layer needs a supporting substrate, which can be either low-grade silicon or a foreign material like graphite or glass. Presently the crystalline thin film Si technology is being actively developed in laboratories and the first crystalline silicon thin film product with 12.2% efficiency is about to be commercialized by Astropower (GOET 00).

#### *1.4.7 III-V Semiconductors*

Semiconductors such as GaAs, GaAlAs, GaInAsP, InAs, InSb, and InP are interesting solar cell materials because they have near-optimal band gaps. These materials are extremely expensive, and have so far been used only in solar cells powering satellites, where performance is more important a criterion than cost, and to some extent in concentrating systems where the active surface area of the cells can be reduced significantly, making possible the use of more expensive materials. InGaP is used in high-power and high-frequency electronics because of its superior electron velocity with respect to the more common semiconductors silicon and gallium arsenide.

#### *1.4.8 Photoelectrochemical solar cells*

The oldest type of photovoltaic cell is the photoelectrochemical solar cell, used already by Becquerel in the discovery of the photovoltaic effect in 1839. In the photoelectrochemical solar cell a semiconductor-electrolyte junction is used as a photoactive layer. While energy conversion

efficiencies exceeding 16% have been achieved with the photoelectrochemical solar cells utilizing semiconductor photoelectrodes (MEIS 99), the instability of these devices with respect to photocorrosion has left them, by and large, devoid of any practical relevance. Furthermore, the photoelectrochemical solar cells which use the same semiconductor materials as in the commercial solar cells, such as Si, CuInSe<sub>2</sub> or GaAs, do not offer any real advantages over the established solid-state solar cells.

### *1.5 Optical solar concentrators*

Due to the high cost of PV materials, it is desirable to use devices of smaller area to which solar radiation is concentrated. Optical solar concentrators can be divided into imaging and non-imaging.

Imaging concentrators produce an image of the solar spectrum concentrating parallel rays in a spot or a line through mirrors or lenses. Since only direct sunlight can be focussed, this type of concentrators requires a tracking system. Fresnel lenses presents problem of non-uniform illumination of the PV cell and a cooling system is needed for mirrors, due to the conspicuous heat production.

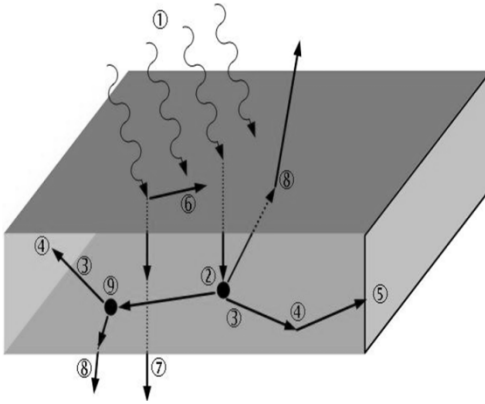
Non imaging concentrators instead focused sun rays to the PV cell but no image of the sun is reproduced. They use direct and diffuse light so there is no need for a tracking system. An example of this type of concentrators is the compound parabolic concentrator. It consists of two reflective parabolic surfaces having their focus points at opposite ends of the PV cell. Rays entering the system inside the acceptance angle are focused onto the PV cell area.

Another example of non-imaging device is the luminescent solar collector (LSC) that was first proposed in 1970s [GOET 77 WEBE 76]. This device was first proposed for greenhouse glazing, but their development has so far been hindered by some relevant practical limitations.

## *1.6 LSC*

A LSC consist of a flat plate or glass, plastic or liquid doped with a luminescent dye [MANS 98]. All the edges of the collector can be covered by a solar cell, or one single edge could host the PV cell while reflective mirrors would be placed on the other edges.

In figure 1.4 the phenomena happening inside a LSC are illustrated. The sun light incident on the LSC (1) is absorbed by the dye molecules (2). Light is subsequently re-emitted at a longer wavelength (3) and is transported to the edges via total internal reflection (4). Light is finally absorbed by the solar cell (5). Other mechanisms are front surface reflection (6), transparency to high wavelengths (7) and losses from the escape cone for light emitted at the Brewster angle (8). In addition, luminescence may be reabsorbed by the dye molecules if they have overlapping absorption and emission spectra (9) - which will eventually result, again, in emitted luminescence.



**Figure 1.4: Possible phenomena taking place in LSC, from [wSIS 11]**

Incident solar radiation enters the device through the exposed surface; selected wavelengths are absorbed by the luminescent dye and re emitted isotropically [FARR 11]. A percentage of this emitted light will be trapped inside the plate by total internal reflection (TIR). TIR occurs at the interface between a medium with higher refractive index ( $n$ ) (e.g. glass, plastics...) and one with lower index (e.g. air). If light hits the interface between plastic and air at a larger angle than the critical one, it remains within the plate; otherwise, it is lost. The amount of emitted light that will be totally internally reflected ( $L$ ) is determined by the index  $n$  of the matrix material by:

$$L = \frac{(n^2 - 1)^{1/2}}{n}$$

The critical angle  $\theta_c$  is determined by:

$$\theta_c = \sin^{-1} \left( \frac{1}{n} \right)$$

The advantages of LSC are:

- Both direct and diffused light are absorbed, so no tracking system is required, reducing installation costs. These systems are suitable for places where high-intensity illumination cannot be achieved on a regular basis and where diffused radiation makes up 60% or more of the radiation incident on a flat surface [GOET 78].
- The emission band of the luminescent species can be matched with the maximum spectral response of the PV cell; thus the possibility arises to break down the solar spectrum into segments and concentrate them simultaneously, stacking plates containing dyes with different absorption characteristics, and matching them with different solar cells.
- As photons whose energy is below the bandgap are converted not into electricity but heat, and as a general rule the performance of solar cells decreases with increasing temperature, it is desirable to prevent below-bandgap radiation from reaching the cell. In LSC devices radiation from energy losses and infrared light is dispersed throughout the front plate avoiding efficiency losses in the PV cell, which remains cooler than a standard PV [RICH 04]. LSC could be suited for building integrated photovoltaics (BIPV) as shading devices or active building facades.

The disadvantages of LSC are:

- Luminescent dyes suffer from photo-degradation and have a limited lifetime [HERM 82]
- Reabsorption losses are due to the often too small Stokes shift (i.e. the difference in wavelength between the absorption and the emission peak).
- The absorption range is often limited, restricting the percentage of solar spectrum that can be exploited by the PV cell.

## 1.7 WLS

A wavelength shifter is a photofluorescent material that absorbs light at some frequency and re-emits it at a different one. In most cases, the wavelength of the emitted light is higher than that of the absorbed light.

There are three types of wavelength shifting [wSIS 11]:

- Down shifting, where an energetic photon is transformed in a less energetic one.
- Down conversion, where the energy of the incident photon is divided up between two lower-energy photons
- Up conversion, where two or more low energy photons are converted into a single high energy photon.

WLS can be used to increase the efficiency of a photovoltaic cell by changing one “overly energetic” photon into more photons of lower energy. Optical fibres doped with a wavelength shifter are typically used to collect scintillation light in particle physics experiments [BART 00; LORE 94; GRAT 00, AMBR 91, BOER 93].



A good wavelength shifter is always composed by two parts, i.e. matrix and dye(s) that have to fulfil some specific requirements [KLAM 09].

The host material must exhibit high transmittance, particularly in the region where the cell's response is high, as well as low scattering. At the same time it needs to provide a good environment for the dissolution of the luminescent species. Finally, it will have to endure the thermal treatment that solar cells are subject to during their manufacturing, and exhibit prolonged photostability over the extended periods of 20–25 years in which PV manufacturers guarantee a minimum of 80% of the initial performance in their modules.

The luminescent species used for LDS [luminescent down shifting] will ideally exhibit: unity IQE [internal quantum efficiency]; a wide absorption band in the region where the EQE [external quantum efficiency] of the cell is low; a high absorption coefficient; a narrow emission band, coinciding with the peak of the cell EQE; good separation between the absorption and emission bands in order to minimize losses due to re-absorption; low cost. In addition, as in the case of host materials, the luminescent species must also exhibit prolonged photostability (20–25 years) [KLAM 09].

## Bibliography

- [AMBR 91]  
C. D'Ambrosio, H. Leutz, S. Tailhardat, M. Taufer, P. Destruel, D. Puertolas, H. Güsten, Organic scintillators with large Stokes shifts dissolved in polystyrene, Nuclear Instruments and Methods in Physics Research Section A: Accelerators, Spectrometers, Detectors and Associated Equipment, 307, (2-3) (1991) 430-435
- [BART 00]  
Rebecca J. Bartlett, Rekha Philip-Chandy, Piers Eldridge, David F. Merchant, Roger Morgan, Patricia J. Scully, Plastic optical fibre sensors and devices, Transactions of the Institute of Measurement and Control 22, 5 (2000) 431-457
- [BOER 93]  
S F de Boer, A S Beddar and J A Rawlinson, Optical filtering and spectral measurements of radiation-induced light in plastic scintillation dosimetry, *Med. Biol.* 38 (1993) 945-959
- [FARR 11]  
D.J.Farrel,M.Yoshida,Operating regimes for second generation luminescent solar concentrators, Prog. Photovolt:Res.Appl. , 20 (2012) 93-99
- [GHAU 06]  
N.Ghausi, Solar oven (cooker & heater), US patent 20060000501; (2006)
- [GOET 77]  
A. Goetzberg, W.Greubel, Solar energy conversion with

fluorescent concentrators, *Applied physics*,14 (1977) 123-139

- [GOET 78]  
A. Goetzber Florescent solar energy collector: operating conditions with diffused light, *Applied Physics*, v16, (1978) 399-404
- [GOPE 97]  
G. Gope, F. Aghdasi, M.D. Dlamini, A review of the photovoltaic industry and its development in Africa, *Solar Energy*,59,4-6(1997),217-225
- [GRAT 00]  
K.T.V. Grattan, T. Sun, Fiber optic sensor technology: an overview, *Sensors and Actuators A: Physical*, 82 (1-3) (2000) 40-61
- [GREE 01]  
Green, M. A., 2001, *Solar Cell Efficiency Tables (Version 18)*, *Prog. Photovolt. Res. Appl.*,(2001) 9, 287-93
- [GREE 03]  
M.A.Green, Crystalline and thin-film silicon solar cells: state of the art and future potential, *Solar Energy*, 73,3(2003) 181-192
- [GUHA 00]  
S. Guha, J. Yang, A. Banerjee, Amorphous silicon alloy photovoltaic research – present and future, *Prog. Photovolt. Res. & Appl.*, 8, 1,(2000) 141-150

- [HERM 82]  
Hermann, Luminescent solar concentrators a review, *Solar Energy*, 29, (1982) 323-329
- [KAZM 97]  
L.L. Kazmerski, L. L., , Photovoltaics: A review of cell and module technologies, *Renewable and Sustainable Energy Reviews*, 1, 1(1997), 71-170
- [KLAM 09]  
E. Klampaftisa, D. Ross, K. R. McIntosh , B. S. Richards, Enhancing the performance of solar cells via luminescent down-shifting of the incident spectrum: A review, *Solar Energy Materials and Solar Cells*, 93, 8, (2009), 1182–1194
- [LORE 94]  
E. Lorenz, S. Natkaniec, D. Renker, B. Schwartz, Fast readout of plastic and crystal scintillators by avalanche photodiodes, *Nuclear Instruments and Methods in Physics Research Section A: Accelerators, Spectrometers, Detectors and Associated Equipment*, 344, 1 (1994) 64-72
- [MANS 98]  
A.F. Mansour, Outdoor testing of luminescent solar concentrators in a liquid polymer bulk plate of PMMA, *Polymer Testing*, 17 ,(1998) 153-162
- [MOHA 09]  
R.M. Moharil, P.S. Kulkarni; A case study of solar photovoltaic power system at Sagardeep Island, India;

Renewable and Sustainable Energy Reviews,13,3(2009),  
673-681

- [RICH 04]  
Richards A. Shalav, R.P. Corkish, A low escape cone loss luminescent solar concentrators 19th E.C: Photovoltaic Solar Energy Conference, Paris, France June 7-11th (2004) 113-116
- [SAHA 99]  
A. Shah, P. Torres, R. Tscharnner, N. Wyrsh , H. Keppner, Photovoltaic Technology: The Case for Thin-Film Solar Cells, Science, 30,285,(1999) 692-698
- [WEBE 76]  
W.H.Weber ,J.Lambe, Luminescent greenhouse collector for solar radiation, Applied Optics, 15(1976) 2299-2300
- [wKYO 2011]  
United Nations Framework Convention on Climate Change (UNFCCC) (2011), Kyoto Protocol, UNFCCC, retrieved last 2011-12-09
- [wMAE 11]  
[www.esteri.it/MAE/IT/Politica\\_estera/Temi\\_Globali/Energia/Situaz\\_italiana.htm](http://www.esteri.it/MAE/IT/Politica_estera/Temi_Globali/Energia/Situaz_italiana.htm); retrieved last 10/11/11
- [wSIS 11]  
<http://siser.eps.hw.ac.uk/research/conversion.html>  
Retrieved last 10/10/2011.

## Chapter 1

- [wSPE 11]  
[http://en.wikipedia.org/wiki/File:Solar\\_Spectrum.png](http://en.wikipedia.org/wiki/File:Solar_Spectrum.png)  
Retrieved 10/10/11
- [WUKE 01]  
X. Wu, J. C. Keane, R. G. Dhere, C. Dehart, D. S. Albin, A. Duda, T. A. Gessert, S. Asher, D. H. Levi, and P. Sheldon. 16.5% efficient CdS/CdTe polycrystalline Thin-Film solar cells. WIP-Munich and ETA-Florence (2001) 995-1000

# CHAPTER 2

## Experimental

---

### *2.1 Introduction*

This chapter provides a description of the experimental techniques and apparatus utilized in this work. The focus is in particular on the use of instrumentation to characterise the samples and on the experimental conditions in which the measurements presented in chapter four were performed.

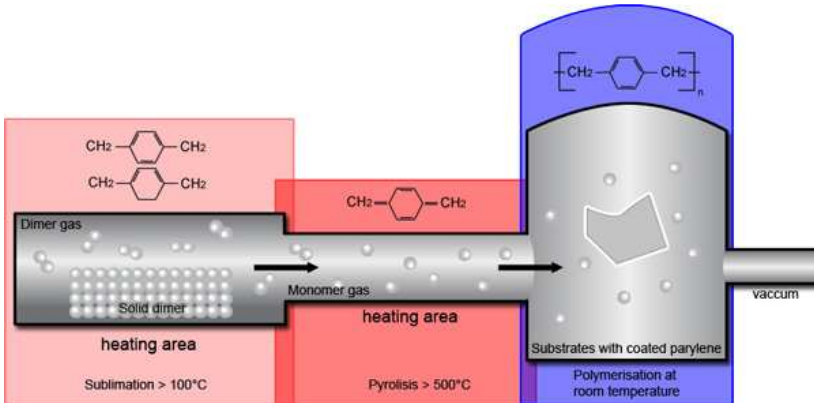
### *2.2 Parylene Production*

A LAB Coater parylometer LC300 (PPS, *Germany*) [wPLA 11] was used to deposit the homonymous polymer called parylene.

The parylene family consists of polymeric materials that can be vaporized and deposited. A peculiar characteristic of these films is that they can coat any geometric shape, in particular objects with deep holes or cracks. Parylene films are transparent and resistant to chemical attacks and cannot be solved in commonly used solvents. They are used for protective coating of medical instruments and electronic devices (motherboards for example).

The basis material is the parylene dimer. The deposition process (Gorham process) consists of several steps. The dimer is firstly heated around 150 °C and vaporized, then transported into a high-temperature chamber (650° C) where the monomer is formed via pyrolysis. The monomer finally enters a deposition chamber where

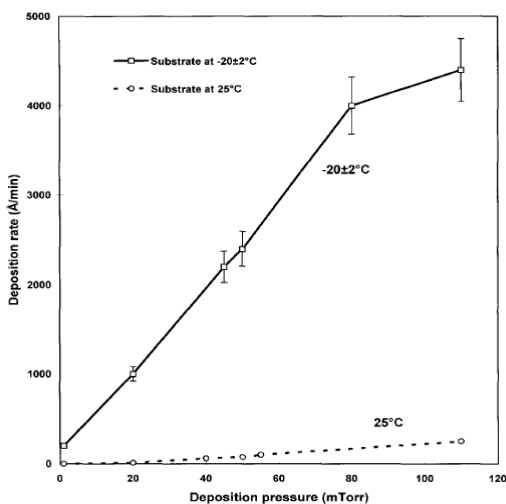
it spontaneously polymerizes into a substrate. In figure 2.1 the process for parylene N is shown.



**Figure 2.1: Deposition process of parylene N [wCOM]**

One of the foremost limitations of parylene is its low deposition rate. For example, in a chamber at 20 °C the deposition rate for a parylene N substrate is 8 nm/min at a pressure of 50 mTorr. An increase in pressure causes an increase in deposition rate (figure 2.2), but the transparency and electric properties of the film are negatively affected. The only viable way to increase the deposition rate is to decrease the chamber temperature (figure 2.2). The film quality is comparable with the quality obtained in a room-temperature chamber.





**Figure 2.2:** The deposition rate of parylene varies almost linearly with pressure and strongly depends on the deposition temperature [YANG 98].

### 2.3 Chemical characterisation process

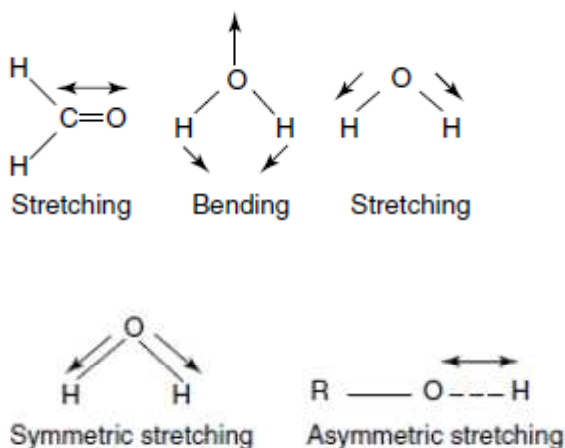
To ascertain the perfect realisation of the desired reactions two main techniques were used: IR for polymers and XRD for rare-earth nanoparticles.

#### 2.3.1 Fourier Transformate InfraRed

FT-IR spectra of the samples were recorded in the  $4000\text{-}400\text{ cm}^{-1}$  range using a Jasco FTIR 660 Plus spectrometer with a resolution of  $4\text{ cm}^{-1}$  ( $2.5\text{-}25.0\text{ }\mu\text{m}$ ). During the measurements, the sample cell and the interferometer were evacuated so as to remove the absorption peaks of water and atmospheric gases from the spectra.

This technique, which permits to identify organic compounds through their characteristic vibrations, was very useful to detect variations in the molecular structure, check their transformations and follow reaction trends.

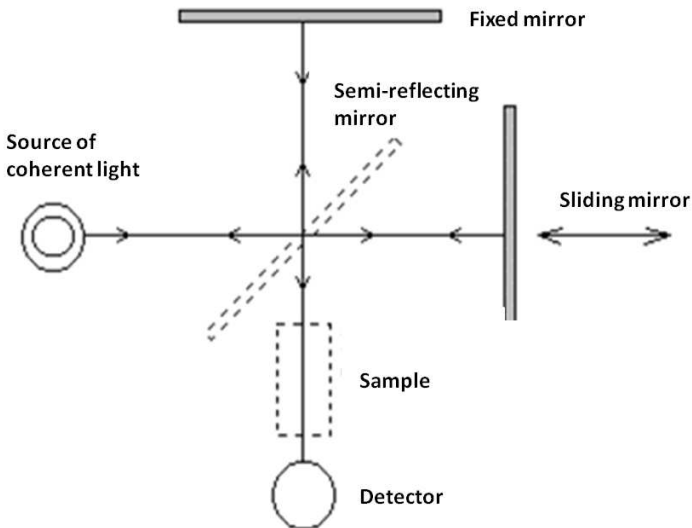
Although energy is absorbed in quanta, spectra do not only display sharp lines but also bands, as every vibration is followed by changes in the orientation of the molecules. Two types of vibration exist: stretching (movement along vibration axes) and bending (variation of bond angle), but only if the dipole momentum varies, as represented in figure 2.3.



**Figure 2.3:** Schematic representation of some molecules in their fundamental vibration.

IR spectroscopy is based on the exploitation of a Michelson interferometer applying a Fourier transform that makes possible the measurement of a spectrum based on the temporal coherence of a radiative source.

The interferometer is based on a source of coherent light at the temperature of 1500-2000K and by two orthogonal mirrors, one fixed and the other mobile. In the middle of the instrument is located a semi-reflecting mirror, acting as beam splitter, which forms an angle of  $45^\circ$  with the other two mirrors; when light reaches this mirror it is split into two beams, one reflected and the other transmitted. Both beams are reflected (by the two orthogonal mirrors) and, again through the beam splitter, they reach the detector. The mobility of one of the two orthogonal mirrors makes possible the creation of constructive or destructive interference. A scheme of the instrument is reported in figure 2.4.



**Figure 2.4** Scheme of Michelson's interferometer.

The detector transforms the incoming radiation into an electrical signal that is amplified and represented as an interferogram; from this signal, using a Fourier transform algorithm, the instrument can reconstruct the IR spectrum.

### 2.3.2 XRD

The arrangement of crystals in powder was determined by means of x-rays, that create a characteristic diffraction pattern when they hit a lattice. From this pattern it is possible to reconstruct the density of electrons within the crystal. From this electron density the mean positions of the atoms inside the crystal lattice can be in turn reconstructed, as well as their chemical bonds, disorder etc [KHAN 06].

In order to collect XRD spectra we used a Rigaku DMax diffractometer (Rigaku, Tokyo, Japan) in the Bragg–Brentano configuration, using CuK $\alpha$  radiation and a monochromator in the diffracted beam in the range  $2\theta = 25^{\circ}$ – $90^{\circ}$  with a  $0.05^{\circ}$  step.

X-ray diffraction results from the interaction between x-rays and electrons of atoms. The interference between two scattered rays is constructive when the path difference between them corresponds to an integral number of wavelengths. This selective condition is described by Bragg's law:

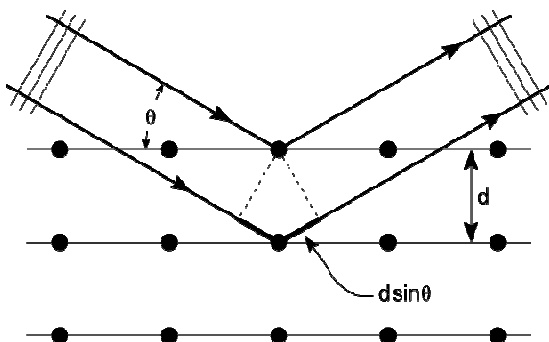
$$2d \sin \theta = n\lambda \quad (\text{eq.2.1})$$

Where  $\lambda$ = wavelength

d = spacing

$\theta$  = Bragg angle

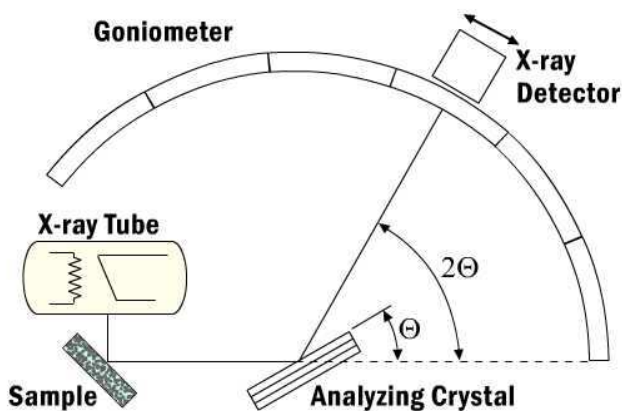
A scheme is reported in figure 2.5.



**Figure 2.5: X-rays incident on an atom lattice**

In figure 2.6 is schematically represented the working principle of an X-ray diffractometer. X rays interfere when the incident beam passes through at least two slits before reaching the sample. The so-called Soller slit limits the divergence of the incident beam in the direction perpendicular to the plane in which the diffracted intensity is measured (this divergence is also known as out-of-plane or axial divergence). The divergence slit establishes the in-plane aperture of the incident beam and the in-plane divergence. Since the sample is irradiated by the divergent incident beam, the diffracted beam converges (self-focuses) at the receiving slit, which is located at the same distance from the centre of the sample as the focal point of the source. These two distances remain constant at any Bragg angle, and both the focal point of the x-ray source and the receiving slit of the detector are located on the circumference of an imaginary circle (cylinder), which is known as the goniometer circle. The radius of the goniometer cylinder is identical to the goniometer radius. The diffracted beam passes through the second

Soller slit before reaching the detector directly (when no monochromator is employed) or being reflected in a crystal-monochromator on its path to the detector. An additional scatter slit, located before the receiving slit, can be employed to reduce the background. The Soller slit on the diffracted beam side can be placed between the scatter and receiving slits. The diffracted beam is monochromatized using a filter or a crystal monochromator. [PECH 05]



**Figure 2.6:** scheme of a x-ray diffractometer.

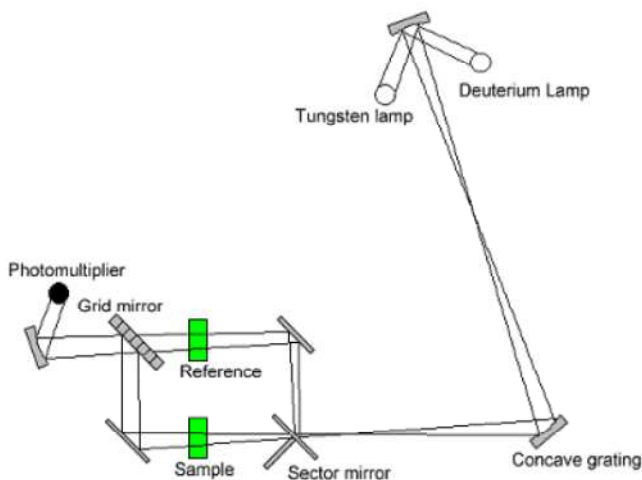
## 2.4 Optical characterization techniques

Properties of dyes, matrices and dye/matrix combinations were studied using the following apparatus: a spectrophotometer to investigate transmission and reflection spectra, a spectrofluorometer to examine the fluorescence behaviour and an

Ocean Optics spectrometer to collect spectra where fluorescent emission and absorption are shown simultaneously.

### *2.4.1 Spectrophotometer*

Absorption, transmission and reflections measurements were performed with a Jasco V-570 dual-beam spectrophotometer. This instrument consists of two lamps, tungsten and deuterium, to cover the whole wavelength range from 190 to 2000 nm. The beam is collimated and focussed on a selector mirror that splits the beam in two; a grid mirror selects frequencies and a photomultiplier collects the incoming light. The two beams are collated and from this comparison the final spectrum is given. In figure 2.7, a scheme of the instrument is presented.



**Figure 2.7: Working scheme of a spectrophotometer.**

In this work we used the instrument as a proper spectrophotometer to evaluate absorption and reflection and as a monochromator to

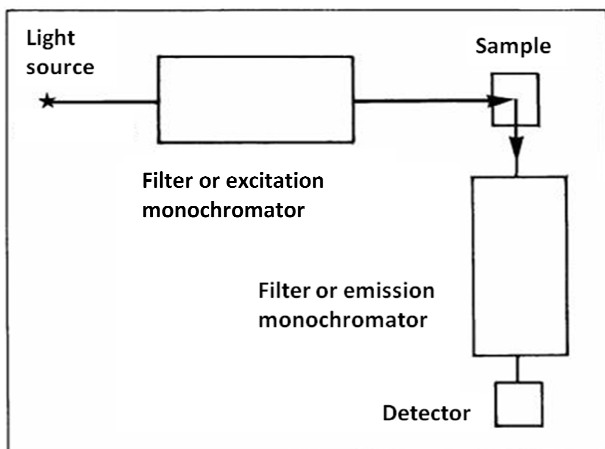
experimentally calculate the shape of the external quantum efficiency (EQE) curves. This last measurement was performed using a calibrated round UV-enhanced photo-detector (New Focus Model 2032) that has a diameter of 5.8 mm and a response range of 190-1100 nm; in order to calculate EQE the power output of the photo-detector was compared to that of the solar cells.

### *2.4.2 Fluorescence*

Fluorescence measurements were performed with three different instruments. The first two were Jasco FP-770 and FP 6300 spectrofluorometers, while the third was an Ocean Optics spectrometer.

We generally worked in “front face geometry” configuration, where the fluorescence is collected from the face hit by the exciting beam and reflected to the detector as shown in figure 2.8.





**Figure 2.8: Spectrofluorometer scheme.**

Our source was a 150 W xenon lamp that allowed us to perform measurements in the range 230-700 nm. The spectral bandwidth was 5 nm for all the spectra, which were corrected taking into account the spectral response of the overall detection system (emission monochromator and detection photomultiplier). [wJAS 11]

These instruments were used mainly to study the fluorescence of molecules in solutions embedded in the matrix. The Ocean Optics spectrometer is more versatile because it makes possible the collection of the whole emission/transmission spectrum, thus yielding a more complete picture of the spectrum incident on the solar cell.

### 2.4.3 Ocean Optics Spectrometer

The Ocean Optics, Model: USB 4000 spectrophotometer is portable and more versatile than a classical spectrometer [wOCE 12]. Its peculiarity is the capability to collect the whole visible spectrum from about 400nm to 800 nm. The possibility exists, moreover, to use optic fibers to reveal light both in transmission and reflection mode.

This spectrometer was used to collect fluorescence and transmitted light so a complete optical characterization could be done on samples as explained in chapter 4.

## 2.5 Physical analysis

To study the surface and thickness of parylene samples were studied with the AFM, which permits to perform more accurate measurements than would have been possible with a simple profilometer.

### 2.5.1 Atomic force microscopy (AFM)

The atomic force microscope is composed by a nanometric probe that interacts with a surface to obtain topographic three-dimensional-information at high resolution in a non-destructive way. This instrument is based on the interaction between the tip and the surface atoms. Every deflection of the cantilever where the tip is mounted corresponds at a topographical variation of the surface. Its position is detected by the deflection of a laser beam.

Considering the atoms as rigid spheres bonded by springs the interaction force could be described as an elastic force.

$$F_m = -Kx$$

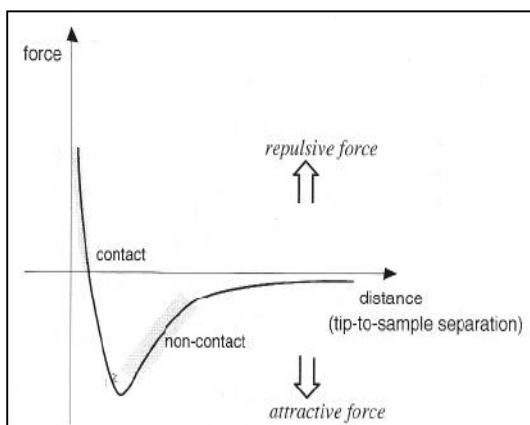
With the elastic constant  $K$  linked to the oscillation frequency ( $\omega$ ) of the system through the relation

$$\omega = \sqrt{(K / M)}$$

Where  $M$  is the atom mass (about  $10^{-25}$  Kg). For example, if the oscillation frequency is  $10^{13}$  Hz  $k$  is equal at 10 N/m.

This technique makes it possible to work with attractive and repulsive forces, both short- and long-radius, such as:

- Van Der Waals: they go from few Angstrom to dozen of nanometers (used for nanometer-scale measurements).
- Electrostatic forces that cause an electron transfer between nearby atoms (from a few Angstrom to hundreds of nanometers)
- Magnetic forces (hundreds of Angstroms).



**Figure 2.9: Schematic representation of the forces between atoms and AFM tip.**

Schematically an AFM consists of the following parts: a cantilever characterized by an elastic constant depending on the application of the instrument (different cantilevers are used for different types of measurements). To control the cantilever motion piezoelectric materials are used; different impulses are sent in order to obtain different types of analysis: a higher velocity is used for lower resolution samples (from 50x50 micron to 1x1 micron) while a lower velocity is used for higher resolution (scanning area from some square microns to 100x100 Å). Deflections caused by the roughness of the surface are revealed with a laser that impinges on the cantilever; the deflection is registered and transformed in a variation of vertical movement.

AFM can be used in two main ways:

- Tip in contact with the surface, when the deflection of the cantilever is measured during the surface analysis; with this method fast scanning is possible.
- Tip not in contact with the surface: here the tip vibrates thanks to AC current. Cantilever and tip reach their resonance frequency, so during the measurement every interaction with the surface is transformed in a frequency variation and a very accurate measurement of the surface can be obtained. The latter configuration is very powerful but slower than the former because of the presence of a feed-back.

The evaluation of AFM results must be careful because of the possibility of image artifacts due to damaged probe, incorrectly-calibrated scanners or thermal drifts that can badly distort images.

The roughness is measured with this instrument and is represented by these fundamental parameters:

$R_a$  is the average

$$R_a = \frac{1}{P} \sum_{j=1}^N \sum_{i=1}^M |\eta(i, j)|$$

Where P is the number of points on the entire surface and A, N and M the x,y and z coordinates and

$$\eta(x, y) = \left\{ I(x, y) - \left\{ \frac{1}{P} \sum_{j=1}^N \sum_{i=1}^M I(i, j) \mid (i, j) \in A \right\} \mid x = 1, \dots, M; y = 1, \dots, N; (x, y) \in A \right\}$$

Is the number of peaks for the whole area.

$R_q$  is the *Root Mean Square* (RMS)

$$x_{rms} = \sqrt{\frac{1}{n} \sum_{i=1}^n x_i^2} = \sqrt{\frac{x_1^2 + x_2^2 + \dots + x_n^2}{n}}$$

$$R_q = \sqrt{\frac{1}{P} \sum_{j=1}^N \sum_{i=1}^M \eta^2(i, j)}$$

$R_q$  is often used as a standard deviation.

## 2.6 Electrical measurements.

In this section all the elements used for the electrical characterization of the samples will be presented. We will introduce the solar cells that we used and the criteria for the choice of them.

Three types of solar cells were tested:

- Si photodiode
- InGaP solar cells
- GaAs solar cells

These types of solar cell have different EQE shown in figure 2.10:

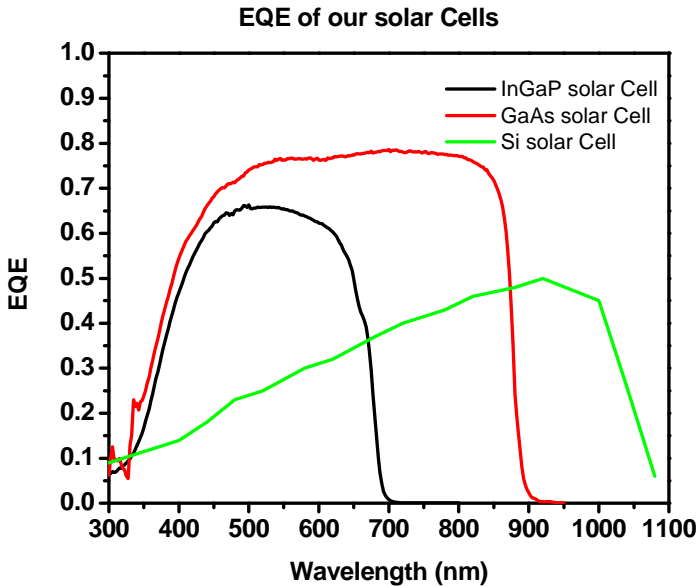


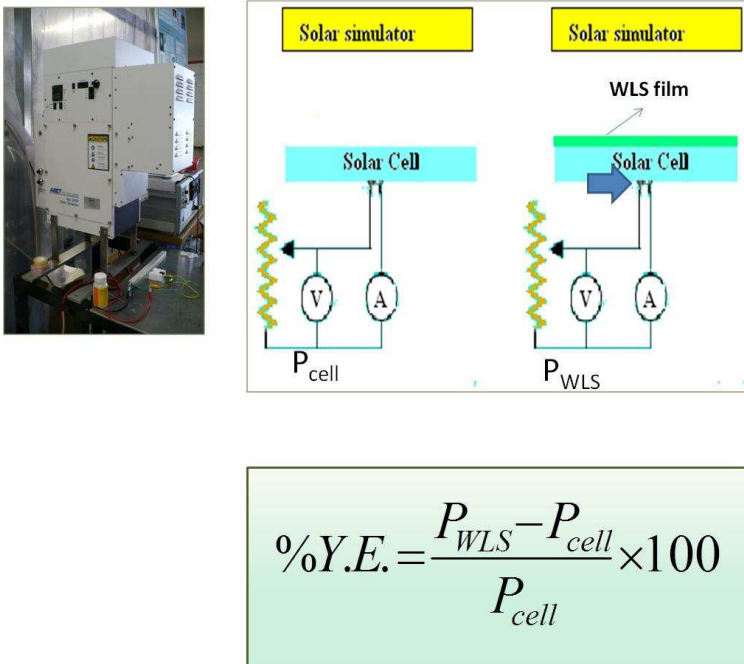
Figure 2.10: EQE of the three type of solar cells: InGaP, Si and GaAs.

The efficiencies of InGaP solar cells, GaAs solar cells and Si photodiodes respectively peak between 450 and 550 nm, between 600 and 850 nm and around 950 nm. These calibration spectra were obtained using a spectrophotometer, measuring the power output of the cells and normalizing the output power to a round calibrated-photodiode UV-enhanced photodetector (New Focus Model 2032) that has a diameter of 5.8 mm and a response range of 190-1100 nm. Results were normalized to power per unit area.

The experimental apparatus is represented in figure 2.11. The solar cells were connected with a rheostat with range from 0.1 to 100000 ohm. Then a voltmeter and an ammeter were connected respectively in parallel and in series.

In WLS tests the cell was first measured first bare. The maximum power was derived from the current and the tension at different resistances was measured. The same measurements were later reproduced with the cell covered by the film. The yield enhancement was calculated as a function of the variation of the maximum power.

In order to perform a repeatable measurement a solar simulator of 300 W was used. Although the device can simulate up to 2 suns all our measurements were carried out with a one-sun setting.



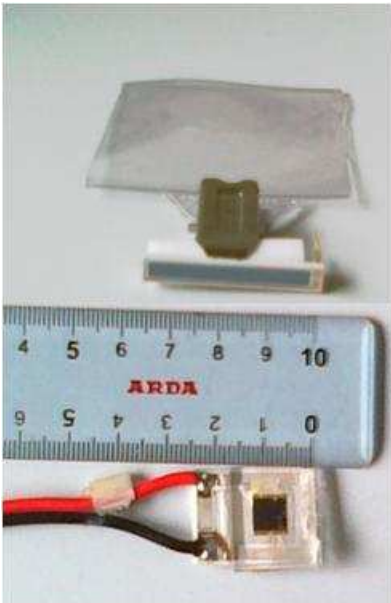
**Figure 2.11: Schematic representation of the experimental apparatus and the formula used to calculate the yield enhancement (%Y.E.)**



Some measurements were also performed in open air; in order to collate various measurement we measured only the open circuit current, that is proportional to the power incident on the cell. We did so because we wanted to minimize the error deriving from the variability of the solar power: every measurement of the complete I-V graph takes in fact ten minutes, and in that time sun lighting conditions can vary and strongly affect the results; measuring only the short circuit current, instead, the results were comparable.

### *2.6.1 Cell Preparation*

In the figure below the cell types that we used are reported. The Si photodiode was purchased from Hamamatsu (type: S3588-03 2a) and has an active area of 3x35 mm. Instead the InGaP and GaAs solar cells were bought from CESI and their active area is of 5x5 mm. These cells were kindly contacted by AUREL and did not have any protective coating. They were used bare in the WLS experiment while in the LSC experiment the two solar cells were coated in 2 mm of clear polysiloxane. The need to encapsulate cells for LSC application derives from the architecture of the cells themselves; the gold contacts that transport the current from the surface to the external contact are arches suspended on a slot that works as charge carrier of the opposite sign, so that crushing the Au arches into the slot would cause a short circuit which would badly damage the cell. For this reason it was important to fold the arches into a matrix; the other purpose of this procedure was to protect the surface of the cell, which is very sensitive to scratches and impurities. An ideal LSC could be directly cast in front of the cell, but we preferred encapsulation to casting in order to be able to re-utilize the cells in the future.



**Figure 2.12: Comparison between a Si solar cell and a GaAs one (the InGaP solar cell has the same appearance as the GaAs).**

Throughout the experiment the cell was measured before and after every step of preparation.

### *2.6.2 Integrating sphere*

The integrating sphere is a device that permits to evaluate the edge output of a luminescent solar collector. It consists in a hollow spherical cavity whose interior is lined with a diffuse white reflective coating, with small holes for entrance and exit ports [YOUN 00]. Its most relevant property is a uniform scattering or diffusing effect. Light rays incident on any point on the inner surface are, by multiple scattering reflections, distributed equally to all other points. . An

integrating sphere may be thought of as a diffuser which preserves power but destroys spatial information. It is typically used with some light source and a detector for optical power measurement.

Integrating spheres are used for a variety of optical, photometric or radiometric measurements. They are used to measure the total light radiated in all directions from a lamp. An integrating sphere can be used to measure the diffuse reflectance of surfaces, providing an average over all angles of illumination and observation. It can be used to create a light source with a uniform apparent intensity over all positions within its circular aperture, and independent of direction except for the cosine function inherent to Lambertian surfaces [YOUN 00]. Since all the light incident on the input port is collected, a detector connected to an integrating sphere can accurately measure the sum of all ambient light incident on a small aperture. The total power of a laser beam can be measured, free from the effects of beam shape, incident direction, and incident position

The optical properties of the lining of the sphere greatly affect its accuracy. Different coatings must be used at visible, infrared and ultraviolet wavelengths. High-powered illumination sources may heat or damage the coating, so an integrating sphere will be rated for a maximum level of incident power. Various coating materials are used. Early experimenters used a deposit of magnesium oxide. Barium sulfate has a usefully flat reflectance over the visible spectrum. Finely-deposited gold is used for infrared measurements. Various proprietary PTFE compounds are also used for visible light measurements.

## *Bibliography*

- [HEXR 09]  
B. B. He, Two-dimensional x-ray diffraction, John Wiley and Sons, 2009
- [KHAN 06]  
R.S. Khandpur, Handbook of analytical instruments McGraw-Hill Professional, 2006
- [MAGO 96]  
S. N. Magonov, M.-H. Whangbo Surface analysis with STM and AFM: experimental and theoretical aspects of image analysis, VCH, 1996
- [PECH 05]  
V. K. Pecharsky, P. Y. Zavalij, Fundamentals of powder diffraction and structural characterization of materials, Springer USA, 2005
- [wCOM]  
<http://www.comelec.ch/> retrieved last 15/12/2011
- [wJAS 11]  
[www.jascoinc.com](http://www.jascoinc.com), retrieved last 15/12/2011
- [wOCE 12]  
[www.oceanoptics.com](http://www.oceanoptics.com) retrieved last 14/02/2012
- [wPLA 11]  
<http://www.plasmatechnology.com>, retrieved last 15/12/2011
- [YANG 98]  
G.R.Yang, S.Ganguli,J.Karcz, W.N.Gill, T.M. Lu, High deposition rate parylene films,J.Cryst.Grow. 183 (1998) 385-390

- [YOUN 00]  
M. Young, Optics and lasers: including fibers and optical waveguides, Springer Germany 2000



# CHAPTER 3

## Materials

---

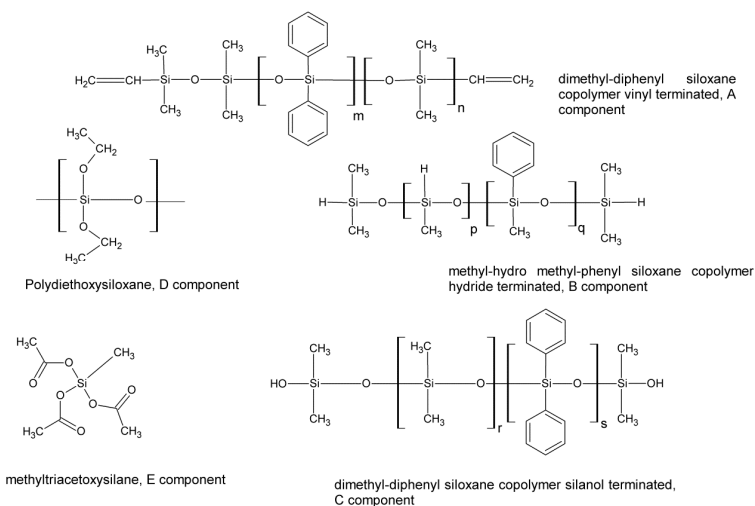
### *3.1 Polysiloxanes: properties and synthesis*

Polysiloxane is a collective denomination for semi-inorganic polymers based on the structural unit  $R_2SiO$ , where R is an organic group characterized by wide-range thermal stability, high lubricity, extreme water repellence and physiological inertness. These polymers are used in adhesives, lubricants, protective coatings, paints, electrical insulation, synthetic rubber and prosthetic replacements for body parts [BOIL 08].

The Si-O-Si chain can be surrounded by side substituents such as hydrogen, methyl, phenyl, and alcoholic groups. All these groups affect the general properties of the matrix. Different types of chemical reactions are possible to obtain cross-linked polysiloxane. Poly-addition and poly-condensation are the reactions used in the present work.

Different types of polysiloxane are here studied in order to establish the best matrices for application as WLS and LSC; in particular, silicones with phenyl substituent were used for WLS to enhance the capability of the matrix to catch UV rays and shift them into a more suitable wavelength range. Their presence increases the solubility and the refractive index, so that a better optical match with the solar cell can be achieved [FILA 93]

The matrices used in this work are shown in figure 3.1.



**Figure 3.1: Polysiloxane matrices used in the present work. The figures were drawn using free ACD Labs software [ACDL].**

The first polysiloxane matrix here studied was the poly addition of vinyl-terminated polydiphenyl-dimethyl-polysiloxane and hydride-terminated poly methyl hydro siloxane. The reaction was catalyzed by a Pt divyniltetrametildisilossane complex in xylene. The second matrix comes from the polycondensation of poly diphenyl-dimethyl silanol and poly(diethoxy siloxane); the reaction was catalyzed by dibutyltin dilaurate. The third reaction was again a polycondensation, catalysed by humidity, between poly(diethoxy siloxane) and tri-acetoxysilane.

### 3.1.1 First reaction

Poly diphenyl dimethyl polysiloxane vinyl terminated copolymer (resin A) has a variable percentage of phenyl substituent and this can influence the subsequent vulcanisation. For this reason the ratio



between the first resin and the hydride terminated resin B is itself variable. In table 3.1 a list of ratios between the resins is presented. Increasing the percentage of phenyl substituent the presence of Si-H groups must increase as well, in order to obtain a sufficient vulcanization between co-polymers. These ratios can be raised in favour of resin B to obtain a lower softness of the rubber matrix.

**Table 3.1: Ratios between resins A and B.**

Percentage of aromatic rings	Ratio between resin A and resin B
4%	100:2
15%	100:1.3
22%	100:2
100%	100:10

To catalyse the reaction Pt divinyl tetrametil disiloxane in xylene was used. Samples were always degassed using a low-vacuum system to free the samples from dissolved bubbles that nucleate and grow during the reticulation at high temperature (60°C), spoiling clearness and optical properties.

### 3.1.2 Second reaction

Silanol-terminated poly diphenyl-dimethyl polysiloxane, catalysed by diphenyldibutyl tin dilaurate, was added to poly(diethoxy siloxane). The Sn catalyst breaks the bond between the silanol group and the methyl group to form the reticulation bond and deliver a molecule of ethanol. This polycondensation was achieved using a ratio between parts of 100:1:10 where the figures respectively correspond to the first resin, the catalyst and the second resin. The co-polymer was then degassed and placed in an

oven for a night to complete the reticulation. The loss in weight due to water evaporation after the reaction was negligible.

### 3.1.3 Third reaction

Here diphenyl-dimethyl silanol terminated was added to triacetoxy silane. The ratio between the two polymers was 100:10 and the polycondensation reaction was catalysed by humidity. The result is a connection between the silanol group of the first resin and the Si-O-C group of the acetoxy ring delivering a molecule of acetic acid. The high ratio between the two polymers results in a high weight loss.

This polymer is suitable for the production of thin films but not for the production of large bulk samples. The very low molecular weight of the first resin does not permit to obtain high thicknesses, as the reaction is catalysed by water and when a film polymerises the remaining non-cross-linked polymer remains isolated from humidity, so that vulcanization cannot take place. To produce high-thickness polysiloxane high molecular weight is suggested. This type of polysiloxane with short chains, in fact, has a high weight loss.

For LSC-purpose polysiloxane the resin was a two-component PS resin, purchased from Rhodia Silicones (RTV141A B). The two resins were mixed in a ratio of 10:1 (A to B component) to obtain the poly-addition, i.e. a vinyl-terminated polysiloxane and a hydride-terminated PS. This is a commercial product so the composition is not completely known; in IR spectra typical peaks of Si-H groups ( $2150\text{ cm}^{-1}$ ) are visible in the B resin and Si-CH<sub>3</sub> groups ( $1275\text{-}1245\text{ cm}^{-1}$ ) are visible in figure 3.2 and table 3.2 for both A and B.

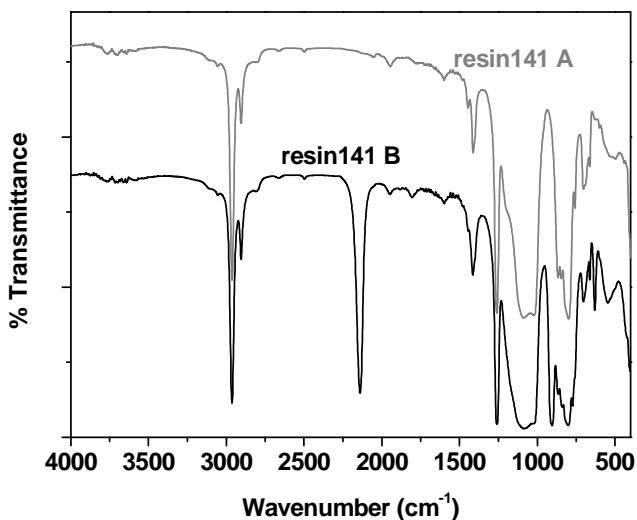


Figure 3.2: Rhodorsil 141 A and B IR spectra.

Table 3.2: Some fundamental peak assignments in polysiloxane.

Bond	Peak position cm <sup>-1</sup>	comments
Si-H	2150	
Si-O-Si	1130-1000	strong
Si-CH <sub>3</sub>	1275-1245	strong and sharp
	865-750	
CH	2900	

## 3.2 Parylene

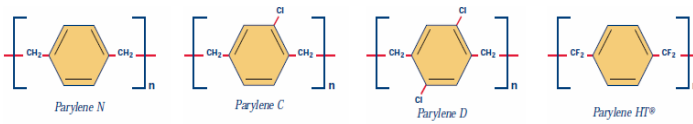
### 3.2.1 Parylene types

Parylene is a generic name for a family of polymers; the base polymer in this family is parylene N (poli para-xylene), discovered by Szwarc in 1947, completely linear and crystalline in structure (figure 3.3). Parylene N is a dielectric material with a low dissipation coefficient, large electric resistance and low, frequency-independent dielectric constant. Parylene N is outstripped only by parylene HT in the ability to penetrate narrow cracks.

Parylene C, the second member in the series, is produced from the same raw material (dimer) as parylene N and differs from it by the replacement of a hydrogen atom with a chlorine one. Parylene C has good physical and electrical properties, and a very low permeability in solutions and gasses.

Parylene D, the third member, is produced from the same dimer as parylene N and C, with 2 chlorine atoms replacing hydrogen ones. It has got very similar properties to parylene C and can be used at higher temperatures.

In Parylene HT, the most recent parylene type, chlorine atoms replace the alpha hydrogen atoms. This type of parylene is used at very high temperatures (>450° C) and in situations where a high stability to UV radiation is required. It has got a very low friction coefficient and dielectric constant, and the highest penetration property amongst parylenes.



**Figure 3.3: Different types of parylene [wSCS 11]**

Parylenes can be deposited as continuous films whose thickness ranges from a few angstroms to 75 microns.

### 3.2.2 Properties of parylene

- *Film dielectric properties:*

One of the main advantages of parylene is the possibility to be deposited in very thin layers. The data in table 3.3 show that parylene displays excellent dielectric properties also in very small thicknesses. It was shown that the difference in fracture potential for thickness unit increases with decreasing film width.

**Table 3.3: Comparison of some electrical properties of parylene and other polymers. [wSCS 11]**

Properties	Method	Parylene N	Parylene C	Parylene D	Parylene HT	Acrylic (AR) <sup>a,b</sup>	Epoxy (ER) <sup>a,b</sup>	Polyurethane (UR) <sup>a,b</sup>	Silicone (SR) <sup>a,b</sup>
Dielectric Strength V/ml	1	7,000	5,600	5,500	5,400	3,500	2,200	3,500	2,000
Volume Resistivity ohm-cm, 23°C, 50% RH	2	$1.4 \times 10^{17}$	$8.8 \times 10^{16}$	$1.2 \times 10^{17}$	$2.0 \times 10^{17}$	$1.0 \times 10^{16}$	$1.0 \times 10^{16}$	$1.0 \times 10^{13}$	$1.0 \times 10^{15}$
Surface Resistivity ohms, 23°C, 50% RH	2	$1.0 \times 10^{13}$	$1.0 \times 10^{14}$	$1.0 \times 10^{16}$	$5.0 \times 10^{15}$	$1.0 \times 10^{14}$	$1.0 \times 10^{13}$	$1.0 \times 10^{14}$	$1.0 \times 10^{13}$
Dielectric Constant									
60 Hz	3	2.65	3.15	2.84	2.21	-	3.3 - 4.6	4.1	3.1 - 4.2
1 KHz		2.65	3.10	2.82	2.20	-	-	-	-
1 MHz		2.65	2.95	2.80	2.17	2.7 - 3.2	3.1 - 4.2	3.8 - 4.4	3.1 - 4.0
Dissipation Factor									
60 Hz	3	0.0002	0.020	0.004	<0.0002	0.04 - 0.06	0.008 - 0.011	0.038 - 0.039	0.011 - 0.02
1 KHz		0.0002	0.019	0.003	0.0020	-	-	-	-
1 MHz		0.0006	0.013	0.002	0.0010	0.02 - 0.03	0.004 - 0.006	0.068 - 0.074	0.003 - 0.006
<sup>a</sup> Handbook of Plastics, Elastomers, and Composites, Chapter 6,						<b>Test Methods:</b>			
<sup>b</sup> Plastics in Coatings and Finishes, 4th Edition, McGraw Hill, Inc., New York, 2002.						1. ASTM D 149			
<sup>c</sup> Conformal Coating Handbook, Humiseal Division, Chase Corporation, Pennsylvania, 2004.						2. ASTM D 257			
						3. ASTM D 150			

- Permeability of parylene

One of the critical tests to prove the resistance of parylene to insufflation is the measurement of its resistance in a cyclic trial; this consists of 10 cycles (one a day) in which temperature and humidity are varied between very low and very high values (25 °C, 50% RH and 65 °C, 90% RH, respectively). The results are presented in Table 3.4 for parylene C films between 50.8 μm and 2.5 μm.

**Table 3.4: Variation of resistance (in ohms) for films from 50.8  $\mu\text{m}$  to 2.5  $\mu\text{m}$  [wSCS 11]**

Parylene Thickness ( $\mu\text{m}$ )	Initial Measurement	Precycle	Step 5 Cycle 3	Step 5 Cycle 7	Step 5 Cycle 10	Step 7 Cycle 10
	25°C, 50% RH	25°C, 90% RH	65°C, 90% RH	65°C, 90% RH	65°C, 90% RH	25°C, 90% RH
50.8	$2.0 \times 10^{14}$	$1.8 \times 10^{13}$	$2.3 \times 10^{12}$	$2.5 \times 10^{11}$	$1.4 \times 10^{11}$	$7.5 \times 10^{12}$
39.1	$5.0 \times 10^{14}$	$2.4 \times 10^{13}$	$8.6 \times 10^{11}$	$1.9 \times 10^{11}$	$1.1 \times 10^{11}$	$5.2 \times 10^{12}$
25.4	$2.0 \times 10^{14}$	$9.2 \times 10^{12}$	$8.1 \times 10^{11}$	$3.4 \times 10^{11}$	$1.3 \times 10^{11}$	$6.3 \times 10^{12}$
12.7	$5.0 \times 10^{14}$	$2.3 \times 10^{13}$	$4.1 \times 10^{12}$	$2.4 \times 10^{11}$	$1.1 \times 10^{11}$	$4.7 \times 10^{12}$
7.6	$5.0 \times 10^{14}$	$2.7 \times 10^{13}$	$4.4 \times 10^{12}$	$9.0 \times 10^{10}$	$4.7 \times 10^{10}$	$2.9 \times 10^{12}$
2.5	$5.0 \times 10^{14}$	$3.2 \times 10^{10}$	$1.3 \times 10^{11}$	$1.1 \times 10^{11}$	$6.4 \times 10^{10}$	$2.3 \times 10^{12}$

- Insulating properties and chemical resistance

The insulation properties of parylene are shown in Table 3.5. Parylene is compared in the transmission rate of water vapor (WVTR) to other polymers. The WVTR of parylene C is evidently superior.

**Table 3.5: Permeability of parylene in different gases [wSCS 11]**

Polymer	Gas Permeability at 25°C, (cc·mm)/(m <sup>2</sup> ·day·atm) <sup>a</sup>				Water Vapor Transmission Rate (g·mm)/(m <sup>2</sup> ·day)
	N <sub>2</sub>	O <sub>2</sub>	CO <sub>2</sub>	H <sub>2</sub>	
Parylene N	3.0	15.4	84.3	212.6	0.59 <sup>b</sup>
Parylene C	0.4	2.8	3.0	43.3	0.08 <sup>c</sup>
Parylene D	1.8	12.6	5.1	94.5	0.09 <sup>b</sup>
Parylene HT	4.8	23.5	95.4	-	0.22 <sup>d</sup>
Acrylic (AR)	-	-	-	-	13.9 <sup>d</sup>
Epoxy (ER)	1.6	2.0 - 3.9	3.1	43.3	0.94 <sup>e</sup>
Polyurethane (UR)	31.5	78.7	1,181	-	0.93 - 3.4 <sup>f</sup>
Silicone (SR)	-	19,685	118,110	17,717	1.7 - 47.5 <sup>f</sup>

<sup>a</sup>ASTM D 1434  
<sup>b</sup>ASTM E 96 (at 90% RH, 37°C)  
<sup>c</sup>ASTM F 1249 (at 90% RH, 37°C)  
<sup>d</sup>ASTM F 1249 (at 100% RH, 38°C)  
<sup>e</sup>Coating Materials for Electronic Applications, Licari, J.J., Noyes Publications, New Jersey, 2003.

- Chemical resistance

Parylenes have a high chemical resistance and are insoluble in any organic solvent at room temperature (table 3.6). The chemical resistance is lower at higher temperatures, but always remains sizable. Parylene C can be solved in chlorine naftalene at 75°C.



**Table 3.6: Parylene swelling in organic solvents at ambient temperature [wCIC 09].**

Solvents		% Swelling Parylene		
Class	Test Member	N	C	D
Alcohol	Isopropyl	0.3	0.1	0.1
Aliphatic hydrocarbon	Iso-Octane	0.2	0.4	0.3
Amines	Pyridene	0.2	0.5	0.5
Aromatic Hydrocarbon	Xylene ( mixed)	1.4	2.3	1.1
Chlorinated Aliphatic	Trichloroethylene TCE	0.5	0.8	0.8
Chlorinated Aromatic	Chlorobenzene	1.1	1.5	1.5
Chlorinated Aromatic	O-Dichlorobenzene	0.2	3.0	1.8
“Freon”	Trichlorotrifluoroethane	0.2	0.2	0.2
Ketone	Acetone	0.3	0.9	0.4
Ketone	2,4-Pentanedione	0.6	1.2	1.4

In organic solvents the chemical resistance of parylene is very strong, as shown in table 3.7, even at high temperature.

**Table 3.7: Parylene swelling in organic solvents at high temperature for 120 minutes [wVPS 11]**

Solvents		% Swelling Parylene			
Class	Test Member	Temp. (°C)	N	C	D
Alcohol	Isopropyl	75	0.3	0.2	0.1
Aliphatic Hydrocarbon	Iso-Octane	75	0.3	0.5	0.3
Amine	Pyridene	75	0.4	0.7	0.7
Aromatic Hydrocarbon	Xylene (mixed)	75	2.1	3.3	1.9
Chlorinated Aliphatic	Trichloroethylene (TCE)	74	0.7	0.9	0.9
Chlorinated Aromatic	Chlorobenzene	75	1.7	2.0	2.1
Chlorinated Aromatic	O-Dichlorobenzene	75	0.3	1.4	0.8
Fluorocarbon	Trichlorotrifluoroethane	37	0.2	0.3	0.2
Ketone	Acetone	56	0.4	0.9	0.4
Ketone	2,4-Pentanedione	75	0.7	1.8	1.6

- Thermal stability, cryogenic properties and in-vacuum behaviour.

From Arrhenius extrapolation parylene C is expected to survive 10 years (100,000 hours) to continuous exposition to air at 80 °C. In an

oxygen-free atmosphere or in outer space parylene is expected to survive 10 years at 220 °C. Any increase in temperature will shorten the polymer’s life. The principal thermal properties of parylene are listed in table 3.8.

**Table 3.8: Principal thermal properties of parylene [wSCS 11]**

Properties	Method	Parylene N	Parylene C	Parylene D	Parylene HT	Acrylic (AR)	Epoxy (ER)	Polyurethane (UR)	Silicone (SR)
Melting Point (°C) <sup>a</sup>	1	420	290	280	>500	85 – 105 <sup>b</sup>	NA	>170 <sup>b</sup>	NA
T <sub>g</sub> Point (°C) (Modulus = 600 MPa)	2, 3	160	125	125	377	–	110	-30	-125
T <sub>4</sub> Point (°C) (Modulus = 70 MPa)	2, 3	>300	240	240	>450	–	120	–	-80
Continuous Service Temperature (°C)	–	60	80	100	350	82 <sup>b</sup>	177 <sup>b</sup>	121 <sup>b</sup>	260 <sup>b</sup>
Short-Term Service Temperature (°C)	–	80	100	120	450	–	–	–	–
Linear Coefficient of Thermal Expansion at 25°C (ppm)	4	69	35	38	36	55 – 205 <sup>b,c</sup>	45 – 65 <sup>b,c</sup>	100 – 200 <sup>b,c</sup>	250 – 300 <sup>b,c</sup>
Thermal Conductivity at 25°C (W/(m·K))	5, 6	0.126	0.084	–	0.096	0.167 – 0.21 <sup>c,d</sup>	0.125 – 0.25 <sup>c,d</sup>	0.11 <sup>c,d</sup>	0.15 – 0.31 <sup>c,d</sup>
Specific Heat at 20°C (J/(g·K))	–	0.837	0.712	–	1.04	1.04 <sup>e</sup>	1.05 <sup>e</sup>	1.75 <sup>e</sup>	1.45 <sup>e</sup>

<sup>a</sup>The temperature at which heat flow properties show signs of change.  
<sup>b</sup>Handbook of Plastics, Elastomers, and Composites, Chapter 6.  
<sup>c</sup>“Plastics in Coatings and Finishes,” 4th Edition, McGraw-Hill, Inc., New York, 2002.  
<sup>d</sup>Coating Materials for Electronic Applications, Licari, J.J., Noyes Publications, New Jersey, 2003.  
<sup>e</sup>Lange’s Handbook of Chemistry, 5th Edition, McGraw-Hill, Inc., New York, 1999.

**Test Methods:**  
 1. DSC  
 2. Taken from Secant modulus-temperature curve (except Parylene HT)  
 3. ASTM 5026 (Parylene HT only)  
 4. TMA  
 5. ASTM C 177 (except Parylene HT)  
 6. ASTM 1461 (Parylene HT only)

As far as cryogenic stability is concerned, 50.8 um parylene C films at -200 °C can be folded by 180° six times before they break up. Other polymers like polyethylene, terephthalate polyethylene and polytetrafluoroethylene break up respectively after three, two and one folding instances. Vacuum tests carried out at the JET propulsion laboratory show the mass loss at 49.4° C and 10<sup>-6</sup> Torr is 0.12% for parylene C and 0.30% for parylene N. The percentage of non-volatile material is 0.01%.

- Mechanical and physical properties

The mechanical and physical properties of parylene are summarized in table 3.9. Because of its high molecular weight (500000) and high fusion temperature and crystallinity, parylene cannot be machined

in massive processes such as extrusion and stamping. The impact resistance is very high when parylene is deposited on the impact test panel. In impact tests with spheres on a parylene thickness of 25.4  $\mu\text{m}$  deposited on a steel panel, values are obtained of 28.2 N\*m. Parylene may be used to increase strength and resistance to abrasion.

**Table 3.9: Some physical and mechanical properties of parylene [wSCS 11].**

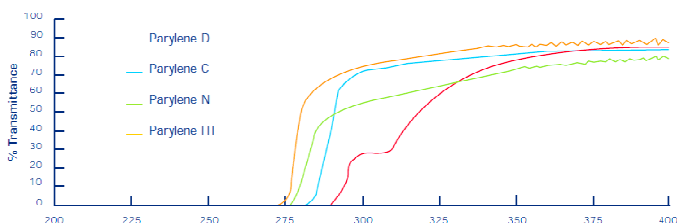
Properties	Method	Parylene M	Parylene C	Parylene D	Parylene HT	Acrylic (AR) <sup>a,b</sup>	Epoxy (ER) <sup>a,b</sup>	Polyurethane (UR) <sup>a,b</sup>	Silicone (SR) <sup>a,b</sup>
Sacant (Young's) Modulus (psi)	1, 2	350,000	400,000	380,000	370,000	2,000 - 10,000	350,000	1,000 - 100,000	900
Tensile Strength (psi)	3	7,000	10,000	11,000	7,500	7,000 - 11,000	4,000 - 13,000	175 - 10,000	350 - 1,000
Yield Strength (psi)	3	6,100	8,000	9,000	5,000	-	-	-	-
Elongation to Break (%)	3	Up to 250	Up to 200	Up to 200	Up to 200	2 - 5.5	3 - 6	>14	100 - 210
Yield Elongation (%)	3	2.5	2.9	3.0	2.0	-	-	-	-
Density (g/cm <sup>3</sup> )	4	1.10 - 1.12	1.289	1.418	1.32	1.19	1.11 - 1.40	1.10 - 2.50	1.05 - 1.23
Index of Refraction (n <sub>D</sub> <sup>20</sup> )	5, 6	1.661	1.639	1.669	1.559	1.48	1.55 - 1.61	1.50 - 1.60	1.43
Water Absorption (% after 24 hrs)	7	Less than 0.1	Less than 0.1	Less than 0.1	Less than 0.01	0.3	0.05 - 0.10	0.6 - 0.8	0.1
Rockwell Hardness	8	R85	R80	R80	R122	M6B - M10S	M80 - M110	68A - 90D (Shore)	40A - 45A (Shore)
Coefficient of Friction									
Static	9	0.25	0.29	0.33	0.15	-	-	-	-
Dynamic		0.25	0.29	0.31	0.13	-	-	-	-

<sup>a</sup>Coating Materials for Electronic Applications, Licart, J.J., Noyes Publications, New Jersey, 2003.  
<sup>b</sup>Handbook of Plastics, Elastomers, and Composites, Chapter 6, "Plastics in Coatings and Finishes," 4th Edition, McGraw Hill, Inc., New York, 2002.

**Test Methods:**  
 1. ASTM D 882 (except Parylene HT)  
 2. ASTM D 5026 (Parylene HT only)  
 3. ASTM D 882  
 4. ASTM D 1505  
 5. Abbe Refractometer (except Parylene HT)  
 6. ASTM D 542 (Parylene HT only)  
 7. ASTM D 570  
 8. ASTM D 795  
 9. ASTM D 1894

- Optical properties and resistance to UV radiation

Parylene displays little absorption in the visible range and is therefore deemed transparent. Below the wavelength of 280 nm all parylene types are very absorbent (figure 3.4).



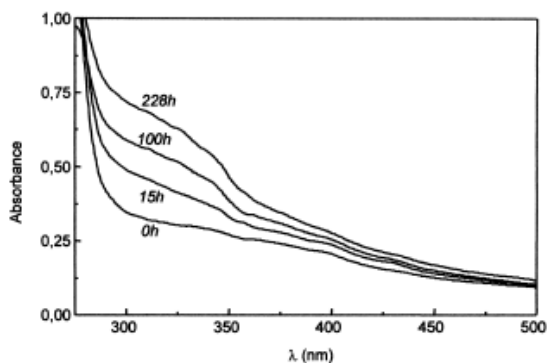
**Figure 3.4: Absorption spectra of various parylene types [wSCS 11].**

All parylene films in vacuum display a high resistance to gamma rays. Electrical properties after expositions of 1000 kGy are basically unaltered. With the exception of the HT type, though, parylene is not recommended for long exposures to UV rays.

- *Photodegeneration*

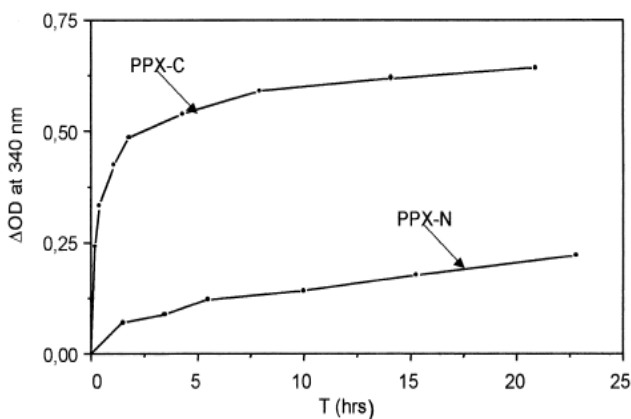
UV radiation is known to induce degradation in polymers. The energy of a photon with a wavelength of 250 nm is 480 kJ and the C-C and C-H bonds respectively correspond to 420 and 340 kJ/mol. Under certain circumstances (for example, if they are located in the proximity of aromatic structures like the parylene ring) these bonds may be even weaker. The absorption of photons whose energy exceeds the binding energy can lead to the breakup of the bonds and the subsequent formation of very reactive free radicals that can interact with the gasses (oxygen in particular) breaking the polymeric chain.

After photolysis (irradiation in vacuum), the absorption spectrum of parylene N displays an increase in absorbance although there are not any absorption peaks in the region between 300 and 600 nm (figure 3.5).



**Figure 3.5: UV absorption curves of parylene in vacuum for various exposure times [BERA 00B]**

The phenomenon of photo-oxidation also depends on the kind of parylene in the film: figure 3.6 shows that the optical density at 340 nm increases much more quickly in parylene C than parylene N.

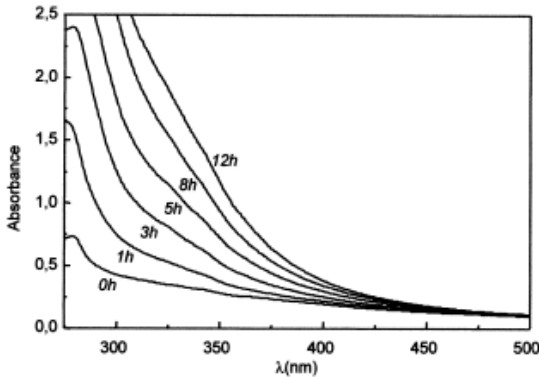


**Figure 3.6: Increase in absorbance at 340 nm of a 18 μm film of parylene C and N as a function of irradiation time [BERA 00B]**

The degradation of parylene N is nevertheless too small to be evidenced by IR analysis. On the contrary, in parylene C (especially in the initial exposure hours) IR analysis evidences the formation of a peak around  $1713\text{ cm}^{-1}$ , which corresponds to the formation of a compound of low molecular weight.

- *Photo oxidation*

In the presence of oxygen, the irradiation of parylene samples leads to relevant modifications in the IR absorption and emission spectra. The modifications observed in the absorption spectrum are more marked than those observed in vacuum (figure 3.7). Photo oxidation causes a high increase in the absorption of parylene and this causes the film to turn yellowish.

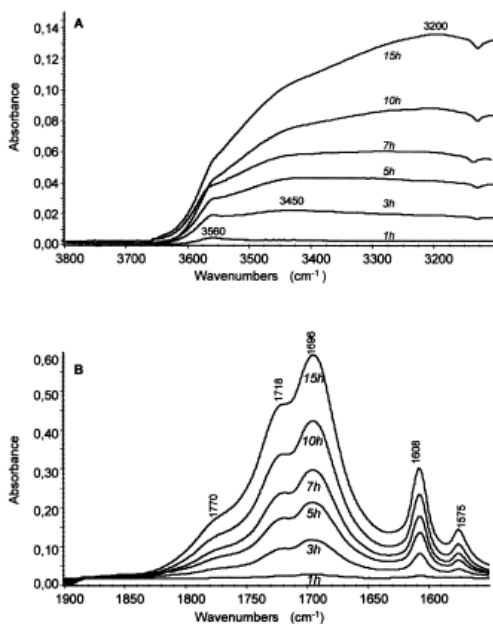


**Figure 3.7: Absorption spectrum of parylene irradiated with UV rays in atmosphere [BERA 00A]**

The change in the IR spectrum is visible in different regions. The comparison between the spectra of a parylene sample before photo

oxidation and after an exposure of a few hours allows the following conclusions to be drawn.

In the hydroxile region (figure 3.8 a) a sizable increment in absorption is visible. After short exposures a marked peak is visible at  $3650\text{ cm}^{-1}$ , which can be attributed to the vibration and steric hindrance of the OH group. For longer exposures absorption is in the range  $3500\text{-}2700\text{ cm}^{-1}$  and two peaks are visible at  $3450$  and  $3200\text{ cm}^{-1}$ , respectively due to the simultaneous vibration of the OH groups in the alcohols and in the carboxylic acids.



**Figure 3.8: FT-IR spectra of parylene exposed to UV for different times A) hydroxilic region B) carbonylic region [BERA 00A]**

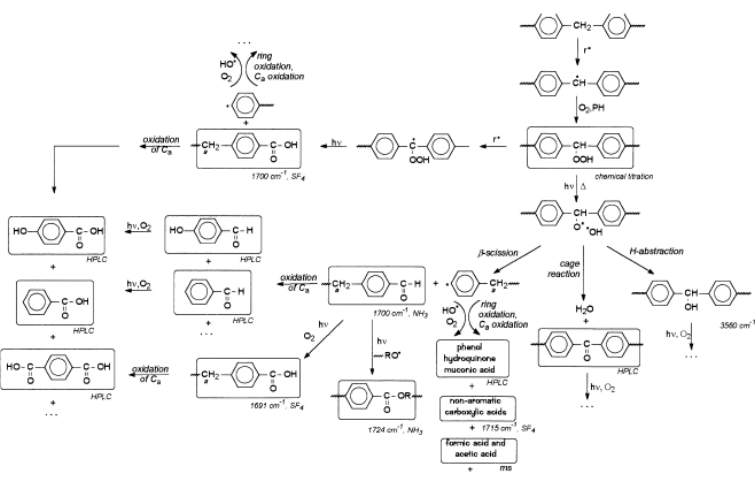


In the zone corresponding to the vibrations of the C=O bond (figure 3.8 b) two peaks appear, with maxima at 1696 and 1718  $\text{cm}^{-1}$  and a shoulder at 1770  $\text{cm}^{-1}$ . The two bands that develop at 1608 and 1575  $\text{cm}^{-1}$  indicate a change in the ring: the aromatic units lose their symmetry through the photo oxidation.

In the region corresponding to the vibrations of the C-O and C-O-H bonds an increase in the absorbance is observed, with a few maxima. These are located at 1421, 1408, 1312, 1277, 1217, 1176 and 1107  $\text{cm}^{-1}$  and hint at the presence of carboxylic acids, ester and alcohols.

In the zone between 900 and 600  $\text{cm}^{-1}$ , which corresponds to the three-dimensional vibration of the compounds (C-H), the appearance of a 767  $\text{cm}^{-1}$  peak suggests that a mono-substituted benzenic ring may have formed.

In figure 3.9 the photo oxidation mechanism of oxidation is reported [BERA 00].



**Figure 3.9: Photo-oxidation mechanism of parylene N [BERA 00A].**

### 3.3 Fluorinated Polyimide

Polyimides are known since 1908, but they were successfully synthesized only in 1950 by DuPont and commercialized only in 1960. Most polyimides have aromatic and hetero-aromatic structures, rigid and planar, and are often insoluble and infusible. The researchers that synthesized them for the first time used the workaround of producing the polymer precursor (polyamic acid), which is soluble, and convert it into the final polyimide. This process is called “two-step” and is currently the most common route for the production of polyimide.

#### 3.3.1 Properties

Fluorinated polyimides are a class of materials with interesting characteristics. In fact, they have excellent mechanical properties,

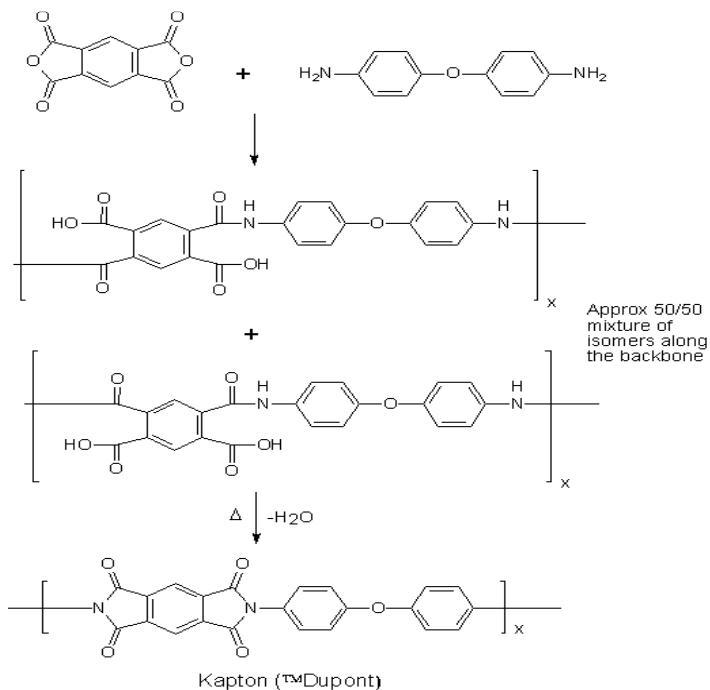
low dielectric constants, low permittivity, high discharge voltage, good machinability, good resistance to wear, high resistance to radiation, very good chemical inertia, good adhesion properties, low thermal expansion and good hydrolytic stability.

In many fields of application, transparent materials are required. Polyimide materials with high transparency at wavelengths longer than those of visible light and a controllable refractive index can be produced introducing fluorine atoms into polyimide materials [SASA 96]. Fluorinated polymers, such as polytetrafluoroethylene, have attractive features such as low water uptake, low permittivity, low refractive index, resistance to wear and abrasion, and both thermal and chemical stability. Those properties are induced by a fluorine atom, its 2s and 2p electrons being very close to the nucleus. Fluorine has a small electrical polarity and is the most electronegative of all elements. This high electronegativity results in strong bonds between carbon and fluorine atoms, so that fluorocarbon materials display high thermal and chemical stability. The low polarity of fluorine makes for a low refractive index and dielectric constant; the low cohesive energy and surface free energy, due to low polarizability, result in low water uptake and in resistance to wear and abrasion [TCAR 04].

The introduction of fluorine atoms into polyimides produces several attractive results. However, a potential downside is that the resulting polyimides may have some undesirable properties such as low adhesion strength, low mechanical strength or a high coefficient of thermal expansion.

## 3.3.2 Two-step polymerisation

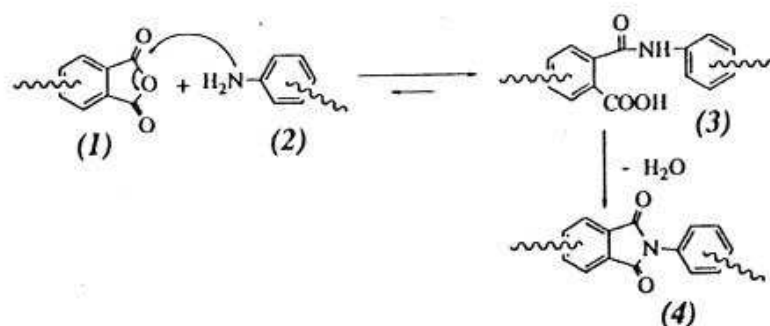
This type of polymerisation is the most common route currently used and is also the route used in this work; in figure 3.10 is shown the two-step process for the production of polyimide PMDA-ODA (Kapton, DuPont). Soluble polyamic acid is initially formed; proper polymerization follows, either through a thermal or chemical route.



**Figure 3.10: Two-step process for the production of polyimide from PMDA and ODA (Kapton) [wKAP 11].**

### 3.3.3 Formation of the polyamic acid

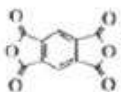
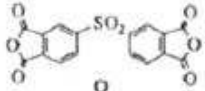
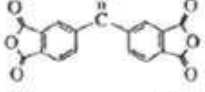
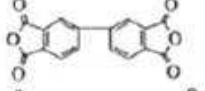
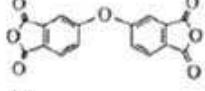
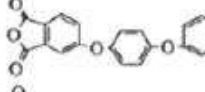
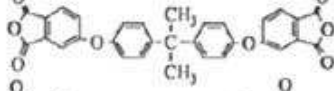
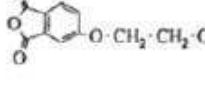
Polyamic acid forms quickly at room temperature adding one diamine and one dianhydride to an aprotic and dipolar solution. The reaction is based on the nucleophilic attack of the amino group on the carbonyl carbon in the anhydride group; this causes the anhydride ring to open and form the amic acid group (figure 3.11).



**Figure 3.11: Representation of the reaction between a dianhydride and a diamine resulting in the ring opening and subsequently closing with the loss of a water molecule [TAKE 96].**

The first part of the reaction is an equilibrium reaction, although it often seems to be irreversible because of the quickly-formed high molecular weight; moreover, the forward reaction is much quicker than the backward reaction, often by various orders of magnitude. For this reason, a large molecular weight cannot be obtained without a high reaction velocity. The reaction is exothermic and is therefore favoured at low temperatures; it is governed by the electrophilicity of the carbonyl group and the nucleophilicity of the nitrogen in the amino group. The phthalic anhydride group is a strong electron acceptor while the two orthogonally located carbonyl


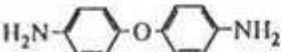
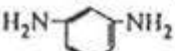


groups, given their strong electronic repulsion, activate each other in a nucleophilic reaction.

Dianhydrides	Abbreviation	$E_s$ (eV)
	PMDA	1.90
	DSDA	1.57
	BTDA	1.55
	BPDA	1.38
	ODPA	1.30
	HQDA	1.19
	BPADA	1.12
	EDA	1.10

**Figure 3.12: Electronic affinity of dianhydrides [TAKE 96].**

The electrophilicity of carbonyl groups can be measured via the correlation with electronic affinity (see figure 3.12). This suggests that a charge exchange may take place between dianhydrides and the amic groups, preceding acylation in which diamine is a donor,

while the dianhydrides is an acceptor. In the reaction, in fact, a variation in colour can be noted, initially due to the electrostatic interactions and charge transfers; the colour later stabilizes with the onset of electrophilic replacement. The reactivity of diamines is instead correlated with their basicity (figure 3.13). The variation in diamine structure seems to influence acylation velocity more than the variation in the dianhydride structure. Three orders of magnitude, in fact, separate electron-donor diamines and electron-acceptor ones.

Diamine	pK <sub>a</sub>	log k
	6.08	2.12
	5.20	0.78
	4.80	0
	4.60	0.37
	3.10	-2.15

**Figure 3.13: Basicity of diamines and their reactivity related to PMDA [TAKE 96].**

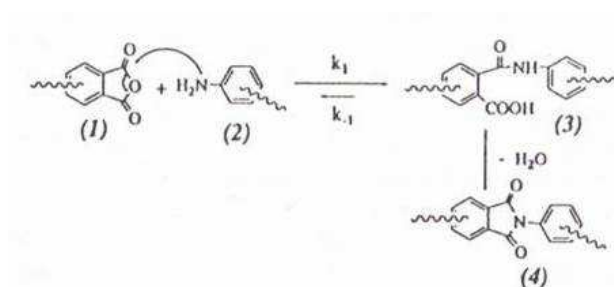
The kind of solvent used in the formation of polyamic acid plays an important role. Dipolar aprotic solvents like N,N-dimethylformamide (DMF), N,N-dimethylacetamide (DMAc), N-methylpyrrolidinone (NMP), and tetramethylurea (TMU) are most common; dimethylsulfoxide (DMSO) may also be used, although it is difficult to remove and it has got a low thermal stability. Such solvents are Lewis bases. It should also be noted that starting from a basic mix the product is an

acid. The strong acid-base interaction between the amic acid and the amide solvent is the main source of exothermicity in the reaction and one of the most important drivers. The polyamic acid is therefore expected to form more quickly in very basic and very polar solvents. This happens in acidic solvents as well, which indicates that the acylation reaction is catalyzed by the acid.

### 3.3.4 Secondary reactions and other factors

Alongside the aforementioned reactions, other routes may play a significant role under certain circumstances, in particular when the nucleophilic acyclic substitution is relatively slow because of the low reactivity or low concentration of the monomers.

As shown in figure 3.14 the main reaction is the acylation and its inverse reaction.



**Figure 3.14: The principal formation reactions of a PI are acylation ( $k_1$ ) and deacylation ( $k_{-1}$ ) [TAKE 96].**

When the polyamic acid is in solution, a small fraction of anhydride groups exist in equilibrium concentration; this implies a relevant role in the hydrolytic degradation of polyamic acid. In the presence of water, the anhydride groups are hydrolysed by the ortho-



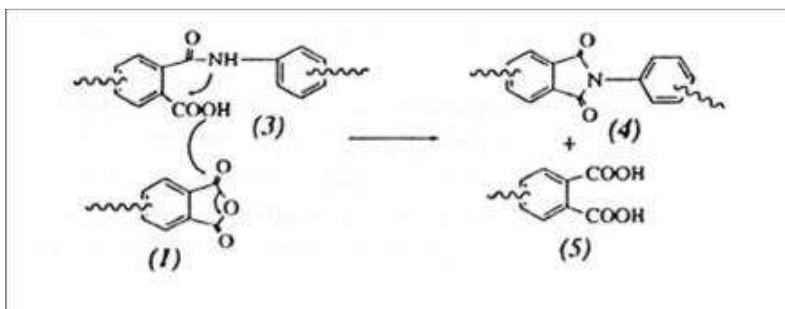
dicarbossilic groups. The reaction is driven by an increase in the nucleophilicity of water in an aprotic bipolar solvent and by strong acid-base interactions between products and solvent; therefore the ortho-dicarbossilic groups remain stabilized as final groups of the polyamic acid and are not converted into anhydride. Humidity plays an important role during polymerization, influencing the molecular weight of the polyamic acid.

The most common sources of H<sub>2</sub>O molecules are solvents that contain traces of humidity; moreover, water is a product of the imidisation of the amic acid groups. This means that the presence of water causes a gradual decrease in the molecular weight in the long term, even if at room temperature the imidisation velocity is relatively low. Polyamic acid solutions, for this reason, should be stored at low temperature to avoid the formation of imides.

It was proved that the change in the distribution of molecular weight from the initial formation of polyamic acid is the main cause of the decrease in viscosity of the suspension in the first hours [TAKE 96]. If the reactions proceed in a heterogeneous manner the conditions are set for an interfacial polymerization between the dianhydride in solid phase and the diamine solution.

The way in which monomers are added for the preparation of polyamic acid is another important factor that influences these results. A diamine solution is prepared, to which dianhydride is added. In this way we make sure that the reacting solution never contains a dianhydride excess, which causes a permanent molecular weight decrease in the polyamic acid (while the excess of diamine can be rectified to obtain the desired molecular weight).

When the solvent contains water as an impurity, some fraction of the anhydride groups is hydrolysed and a no longer reactive group is left. The result is that the equivalent number of amino groups that remain unbound will be equal to the stochiometric number of monomers not initially used (figure 3.15).



**Figure 3.15: Effect of anhydride excess in polyamic acid [TAKE 96].**

If some quantity of equivalent dianhydride is added to the amino groups that did not react, it will react with the final groups and the molecular weight will increase. Although the groups of the ortho-carboxylic acid are inactive at room temperature, they get dehydrated and react with the amines at high temperature, thus creating a situation in which the dianhydride is in excess. The molecular weight of the produced polyamide is primarily determined by the stochiometric reaction of the products.

### 3.3.5 Chemical imidisation and poly iso-imides

The cyclodehydration of polyamic acid can take place at room temperature if the reactants are anhydric acids in an aprotic solvent or in the presence of tertiary amines. Common de-

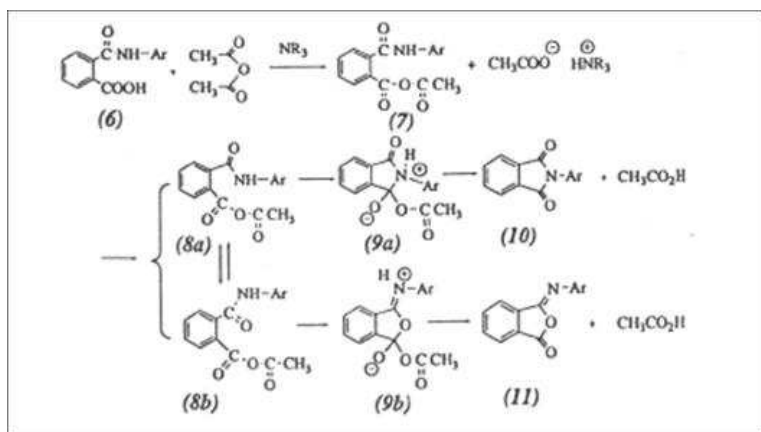
hydrating reactants are: acetic anhydride, propionic anhydride, n-butirric anhydride, benzoic anhydride.

Catalyzing amines are for example piridin, metilpiridin, lutidin, N-metil morpholin, trialchilammin. If the trialchilammines have a high pKa (>10.65) a polyimide of high molecular weight will be obtained. If less-basic tertiary amines are used lower molecular weights will in general be obtained, although several factors affect the validity of this statement, like the dehydrating agent, the monomers in the polyamic acid and the reaction temperature.

### *3.3.6 Mechanisms*

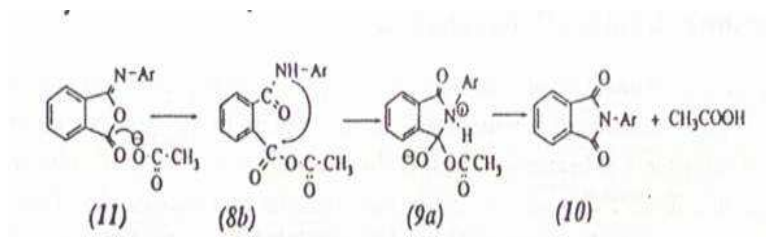
In a kinetic study it was observed that isoimides as well as imides may be formed, mixing the diammine with the anhydride intermediate (figure 3.16, point 7) that is formed in the acylation of carbossilic groups (figure 3.16, point 6) in the amic acid.

The imides are formed in the intramolecular nucleophilic substitution, on the anhydride of carbonyl, of the nitrogen atom in the amide (figure 3.17, point 8a-9a) while the isomides are the result of the substitution of the oxygen in the amide; the ammine acts as a catalyser as if it were an acceptor acid.



**Figure 3.16: Mechanism of the chemical dehydration of the amic acid [TAKE 96].**

If a basic ammine ( $pK_a > 10.6$ ) is used like triethylamine, only normal imide is produced, while imide and isoimide are produced together when mildly basic catalysers are used like pyridine ( $pK_a$  5.2). In the latter case the production of isoimide is initially very high, although it is later surpassed by the production of imide as, albeit slowly, isoimide re-arranges itself into imide (figure 3.18).



**Figure 3.17: Asset mechanism of isoimide into imide [TAKE 96].**

This transformation is catalyzed by the acetate ion. The isoimide is characterized by a strong absorption between 1750 and 1820  $\text{cm}^{-1}$  and assumes the structure of the imino lacton. Moreover, it displays a strong band 901 and 934  $\text{cm}^{-1}$ . The isoimides usually display a light yellow colour due to absorption between 350 and 400 nm.

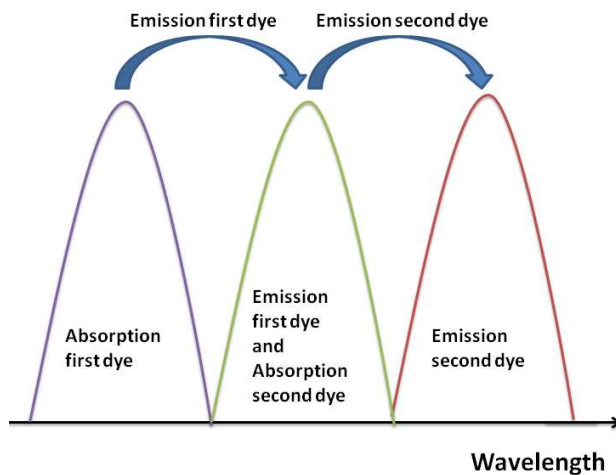
## 3.4 Dyes

### 3.4.1 Characteristics

Candidate dyes for WLS and LSC applications must possess some intrinsic characteristics, but their properties depend on the matrix host as well. This section provides an overview of the dyes investigated in the present study; we will in particular focus on 3HF because of its peculiar behaviour in polysiloxane. The properties of dye and matrix will be matched in chapter 4 where, on the basis of optical considerations, an optimal choice will be made regards both dye and matrix for the purpose of the present work.

An optimal trade-off between optical features and quantum yield must be sought in selecting a dye for a specific application. In fact, our original aim was to obtain a large Stokes shift using a combination of two or three dyes, one of which characterised by high absorption in the wavelength interval in which emission from the other one or two dyes would peak, as illustrated in figure 3.18. In order to avoid re-absorption phenomena, the overlap between the emission and absorption spectra of each dye should be minimal; moreover, the quantum yield should be unity, as every step decreases the efficiency of the process. This multi-step process is one way to overcome the usually small shift of organic dyes.

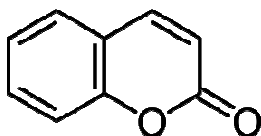
Samples made with Lumogen were used for this purpose, but the visible spectrum was not completely covered. For this reason Coumarin was considered for the purpose of filling an absorption gap between the emission of Lumogen violet and the absorption of Lumogen yellow 083.



**Figure 3.18: Illustration of the multiple-dye WLS mechanism.**

### 3.4.2 Coumarins

Coumarins are chemical compounds of the class of benzopyrone. These molecules have the chemical formula of 2H-chromen-2-one as represented in figure 3.19.



**Figure 3.19: 2H-chromen-2-one structure using (drawn using [ACDL])**

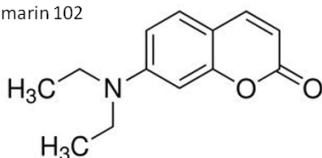
Many natural compounds are based on coumarines, as tonka bean (*Dipteryx odorata*), vanilla grass (*Anthoxanthum odoratum*), sweet woodruff (*Galium odoratum*), mullein (*Verbascum* spp.), sweet

grass (*Hierochloe odorata*), cassia cinnamon (*Cinnamomum aromaticum*) and sweet clover (*Fabaceae* spp.). Those types of lumophores are widely uses as laser dyes.

In the following picture the name and formula are reported of selected coumarins.

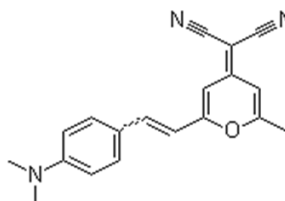
Coumarin 480:

2,3,6,7-tetrahydro-9-(methyl-1H,5H,11H-[1]benzopyrano-[6,7,8-ij]quinolizin-11-one);  
Coumarin 102



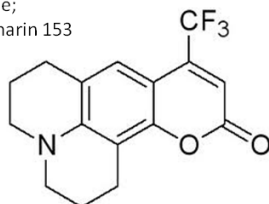
DCM:

[2-[2-[4-(dimethylamino)phenyl]ethenyl]-6-methyl-4H-pyran-4-ylidene]-propanedinitrile



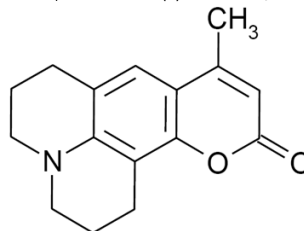
Coumarin 540A:

2,3,6,7-tetrahydro-9-(trifluoromethyl)-1H,5H,11H-[1]benzopyrano[6,7,8-ij]quinolizin-11-one;  
Coumarin 153



Coumarin 466 :

7-(diethylamino)-2H-1-benzopyran-2-one;



**Figure 3.20: Structure of the coumarin molecules used in this project (drawn using [ACDL]).**

Numerous types of coumarines are commercially available and currently used mostly as laser dyes, but for our purpose of obtaining a large spectral shift only four coumarines were found to be suitable for combination with other dyes. These molecules were chosen for the possibility to obtain a large final Stokes shift or for their large



intrinsic Stokes shift (as for DCM). Coumarines are very sensitive to the surrounding environment; for example Lewis and Maroncelli [LEWI 98] studied the behaviour of coumarin 153 and evidenced that the quantum yield was sizably dependent on the solvent, ranging from 0.42 in methanol to 0.95 in 2-methylbutane.

We picked (figure 3.20) coumarin 466, DCM, coumarin 153 and coumarin 102 because, as shown in table 3.10, we were looking for

- Molecules whose absorption spectrum peaks around 430 nm (C153, to be coupled with emission from Lumogen violet), or
- Molecules that shift UV wavelengths to 470 nm (where there is the maximum absorption peak of Lumogen yellow 083 as for C466 and c480), or
- Molecules characterized by a large Stokes shift (as for DCM) (table 3.10)

**Table 3.10: Absorption and emission maxima of coumarin in ethanol [wEXC 11]**

Dyes	Absorption I max (nm)	Emission I max (nm)	Solvent
<b>Coumarin 480</b>	399	466	ethanol
<b>Coumarin 530A</b>	423	530	ethanol
<b>Coumarin 466</b>	368	463	ethanol
<b>DCM</b>	481	644	methanol

### 3.4.3 Lumogen dyes

Lumogen dyes are clearly designed for LSC concentrators as described by the Lumogen F datasheet [wBAS 12].

Their characteristics are:

- Outstanding stability to light in the plastic of interest
- Strong luminosity
- Extremely high chroma
- Possibility to be readily incorporated in plastics
- High heat stability

For these reasons Lumogen dyes were developed in the project Fluka (TM).

In table 3.11 the absorption and emission peaks and quantum yields of Lumogen dyes are presented.

**Table 3.11: Lumogen F optical properties [wBAS 09].**

<b>Lumogen</b>	<b>Type of dye</b>	<b>Abs. <math>\lambda</math> max (nm) CHCl<sub>3</sub></b>	<b>Emission <math>\lambda</math> max (nm) CHCl<sub>3</sub></b>	<b>Quantum Yield</b>
<b>Violet 570</b>	Naphtalimide	378	413	>85
<b>Blue 650</b>	Naphthalimide	377	411	>80
<b>Yellow 083</b>	Perylene	476	539	>85
<b>Green 850</b>	Perylene	475	489	>90
<b>Orange 240</b>	Perylene	524	539	>90
<b>Yellow 170</b>	Perylene	505	528	>90
<b>Pink 285</b>	Perylene	547	580	>78
<b>Red 300</b>	Perylene	578	613	>90

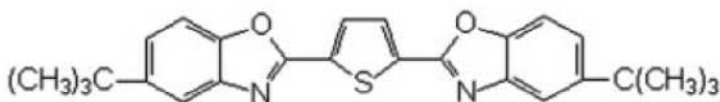
According to the Lumogen datasheet migration must be expected in plastics that contain butadiene and plasticizers or are partially

crystalline. This issue must be investigated if Lumogen F dyes are to be used in systems of this nature.

The optimal dye concentration depends on the thickness of the plastic to be coloured. Normally, a proportion of 0.005 – 0.02 % is sufficient.

#### 3.4.4 BBOT

BBOT is a molecule that absorbs in the UV region around 370 nm and re-emits in the proximity of 440 nm, as shown in figure 3.21. The excitation spectrum has two main peaks at 376 and 395 nm and a smaller one at 270 nm, while the emission spectrum displays two main peaks at 412 and 436 nm, respectively, and a smaller one at 350 nm. [WANG 07]



**2,5-bis(5'-t-butyl-2-benzoxazol-2-yl)thiophene (BBOT)**

**Figure 3.21: Structure of 2,5-bis(5'-t-butyl-2-benzoxazol-2-yl)thiophene (BBOT).**

At higher concentrations the absorption peak at 270 nm is visible; this small peak is also present in solution of BBOT in cyclohexane in Tury's fluorescence study [TURY 98].

### 3.4.5 3 Hydroxy flavone

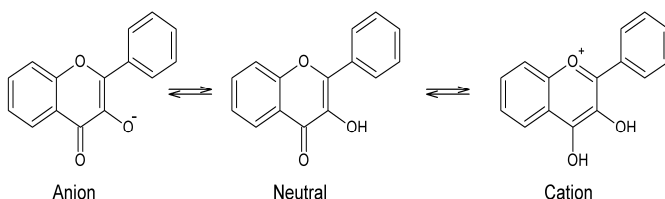
A detailed presentation will now be provided of 3hydroxy flavone (3HF) and the interaction between this dye and polysiloxane.

#### 3.4.5.1 The molecule

3 hydroxyflavone (3HF) is a widely-known molecule of the family of flavonoids characterized by dual fluorescence and intramolecular excited-state proton transfer (ESIPT) [KUMA 01, SENG 79,WOOL 81, STRA 83, CART 03].

This molecule was previously used as a sensor to reveal tin compounds [CROM88] [ALDR 81] or in organic light emitting diodes [HAMA 97]. It can also work as a chelating agent forming different types of complexes; for this reason a wide variety of metallic compounds were tested such as aluminium chloride [JURD 56, CONR 03], zinc and beryllium etc.

The most important characteristics displayed by 3HF are the process of intramolecular excited-state proton transfer (ESIPT), the dual fluorescence feature and the high Stokes shift of the tautomeric form (about 180 nm), which hinders re-absorption phenomena [SENG 79,WOOL 81, STRA 83]. These characteristics make this molecule an excellent wavelength shifter (WLS) [CART 04]. Therefore a possible use of the dye as fluorescent molecule for photovoltaic applications can be envisaged.



**Figure 3.22: Structure of 3HF (drawn using [ACDL]).**

3-Hydroxyflavone undergoes acid-base equilibrium, as depicted in figure 3.22, thus leading in alkaline or acidic media to several ionized forms, each characterized by a specific optical response. The neutral form shows an absorption peak at about 360 nm and an emission peak at 408 nm in ethanol [STRA 85, SENG 79], the anionic form has an absorption peak at about 400 nm and an emission peak at 500 nm, whereas the cationic form displays absorption at 380 nm and emission at 430 nm [WOLF 83].

All these forms coexist and can change into one another but their existence depends on the bond they create with the surrounding environment.

The entrapment of 3HF in suitable solid media is possible and hybrid materials have been studied with particular reference to the preservation of the optical properties of the dye. To cite some examples, 3HF has been entrapped in sol gel derived matrices [CART 03, LACA 10] and, for biological applications, in lipid bilayers [DASR 08].

3HF has a marked solvatochromic behaviour (table 3.12); the equilibrium between its forms strongly depends on the environment. The molecule was studied in different solvents such as

ethanol, methanol, acetonitrile [BRUC 91], DMSO and cyclohexane [FENG 08]

3HF is very sensible to pH variations; it has been in fact used also as a sensor for organic vapours [TCAR 04]. Wolfbeis and co-workers [WOLF 83] observed the absorption and emission of 3HF in different aqueous solutions at different pH levels and in different organic solvents. Their results are presented in Table 3.12, where the wavelengths of maximum absorption, excitation and emission are reported as a function of the solution acidity and the organic solvent used.

**Table 3.12: Absorption and emission maxima of 3HF in different solvents [KUMA 01]**

	Benzene	Ethyl acetate	Ethanol	Acetonitrile	Methanol	Water
$\lambda_{\text{abs}} \text{ (nm)}$	343	343	344	344	344	347
$\lambda_{\text{em}} \text{ (nm)}$	527	530	545	542	549	550

In the absorption spectra three main species can be individuated which present maxima at 402 nm (pH>10), 342 nm (pH 9-1) and 378 nm ( $H_0$  from -4 to -8), but four distinct fluorescence bands are observed when the acidity of the solution is increased stepwise from pH 13.0 to  $H_0$  -7.4; these bands have maxima at 508, 406, 514 and 430 nm.

Only one band is observed in strongly alkaline and strongly acidic solutions, while two fluorescence bands are observed in the range from pH 10 to  $H_0 - 0.31$  as well as in methanol and ethanol. Their excitation spectra coincide, thus indicating that they originate from the same ground state species and that there are two pathways for deactivation.

**Table 3.13: Wavelength UV absorption, excitation and fluorescence data for flavonol in solutions with different acidities and in organic solvents [HAMM 70]**

Solvent	$\lambda_{\max}^{abs}$ (nm)	$\lambda_{\max}^{exc}$ (nm)	$\lambda_{\max}^{flu}$ (nm)
<i>Organic solvents</i>			
Ethanol (95%)	344, 352	350, 310	405, 531
Methanol	345, 354	345, 308	409, 531
Diethyl ether	342, 355	342, 358 <sup>c</sup> , 308	401, 532
Toluene	345, 357	357, 344, 310	530
Cyclohexane	340, 352	352, 342, 308	527
<i>Aqueous solvents</i>			
pH 13	402	402	508
pH 10	402	400 <sup>a</sup> , 348	408, 509
pH 7	342	342, 310 <sup>b</sup>	409, 514
pH 3	342	342, 310	406, 514
pH 0	344	342, 312	406, 440 <sup>c</sup> , 510
H0 -0.31	345	342, 314	510
H0 -1.72	360	355	430
H0 -3.38	373	380	430
H0 -6.8	378	380	430

<sup>a</sup> For the 509 nm emission only.

<sup>b</sup> For both the green and the violet band.

<sup>c</sup> Shoulder.



In aqueous solutions 3HF assumes three main forms: anion (A), neutral molecule (N) and cation (C). The existence of these three forms is evidenced by the absorption spectra; the equilibrium between the species is governed by the ground state  $pK_a$ . The presence of three of four excited species is evident from the fluorescence spectra and the following assignments can be made:

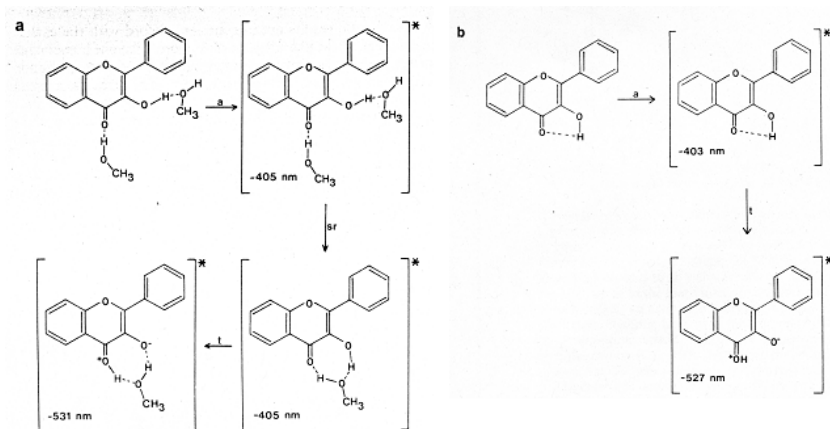
$$\lambda_{\max}^{flu} = 508 \text{ nm to A, } \lambda_{\max}^{flu} = 406 \text{ nm to N and } \lambda_{\max}^{flu} = 430 \text{ nm to C.}$$

The 514 nm band is assigned to the phototautomer, in which excited-state proton transfer has occurred. In neutral solutions it is generally difficult to discern between the tautomer deactivation and the anion photo-dissociation because their bands are too close to be clearly distinguished.

Besides the 3HF pH-dependence, polarity and the protic nature of the surrounding environment affect the optical features of 3HF. The ESPT mechanism (figure 3.23) derives from the interaction of solvent molecules with keto-enol tautomerism.

In the case of a polar medium (figure 3.23 1a) with hydrogen bonding capabilities, such as alcoholic systems, the intramolecular proton transfer can be remarkably hindered, thus leading to enhanced emission in the blue region from  $N^*$ . The tautomeric form, which emits at longer wavelengths, is by far the most desirable for any application where large Stokes shift is needed. There exists a tautomeric equilibrium between the forms  $T^*$  and  $N^*$  and  $N^*$  is most favoured in protic polar environments; the formation of intramolecular hydrogen bonding slows down the formation of the tautomeric form. The emission from this form is enhanced in the case of non polar, non hydrogen bonding solvents (figure 3.23 b). The tautomeric form has an absorption peak at 350

nm and an emission one at 530 nm. This last condition is the most desirable, as the large Stokes shift (180 nm) minimizes re-absorption phenomena.



**Figure 3.23: Keto-enol tautomerism in 3HF (a) in polar, hydrogen bonding solvents with double-proton transfer tautomerization and (b) in non-polar, aprotic solvents [WOOL 81]**

3-hydroxyflavone forms strong intramolecular hydrogen bonds in hydrocarbon solvents, so that phototautomerization is the only possible process in an excited state (figure 3.23 process b), while in alcoholic and aqueous solutions flavonol is both intramolecularly and solvent hydrogen bridged and will undergo intramolecular single-proton transfer to produce green fluorescence as shown in (figure 3.23 process a).

External hydrogen bridging needs double-proton transfer between solvent and solute to form the tautomer. This process is quite slow so in hydroxylic solvents emission is observed from both singlet-

excited flavonol (blue-violet emission) and its phototautomer (green emission).

Emissions in different media are driven by different kinetic rate constants; in hydrocarbon solvents the tautomerisation rate constant has a higher value than in alcohols where the strong intermolecular hydrogen bonding disrupts the weak intramolecular hydrogen bonding in 3HF.

### *3.5 Lanthanide nanoparticles*

#### *3.5.1 Lanthanides properties*

A possible alternative to dyes, that are known to suffer from stability and durability problems, is represented by nanoparticles. Luminescent nano species exhibit high quantum efficiency (number of photons emitted/number of photons absorbed), but low absorption coefficient [ROWA 08, STRU 07, KLAM 09]

Rare-earth nano particles have recently attracted great interest because they can be used in luminescent devices [SIVA 05], optical amplifiers [KUMA 07], labels for biomolecules [EVAN 06, SIVA 06, DIAM 05, DIAM 06] and as emitting species in many phosphors [ROND 98].

In particular, the 4f inner shell of lanthanides is full, and the most stable electron configuration is represented by their trivalent form. The number of possible configurations for some number of electrons sitting on the fourteen 4f orbitals is large. The corresponding energies range from ultra violet (UV) to infra red (IR).

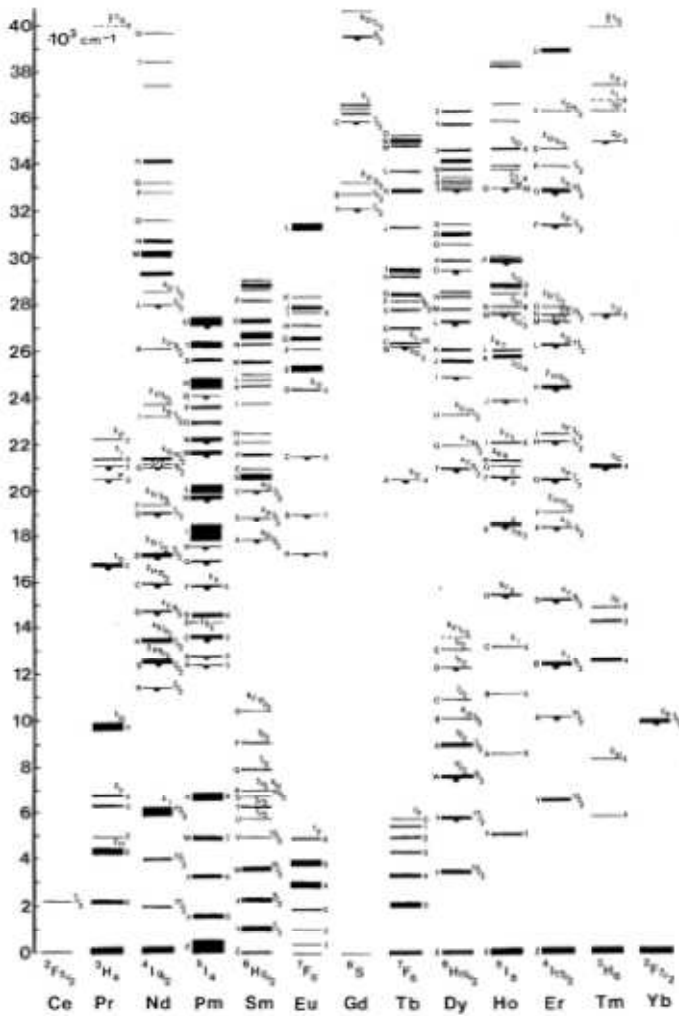
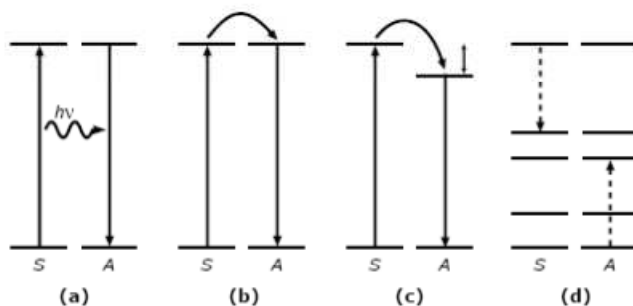


Figure 3.24: Dieke diagram of the observed energy levels of trivalent lanthanide ions [DIEK 68].

Figure 3.24, also called ‘Dieke diagram’, shows the energy level structure of the  $4f^n$  configuration of the trivalent lanthanide ions [DIEK 63, WEGH 00]. This diagram also evidences the abundance in energy levels of these ions.

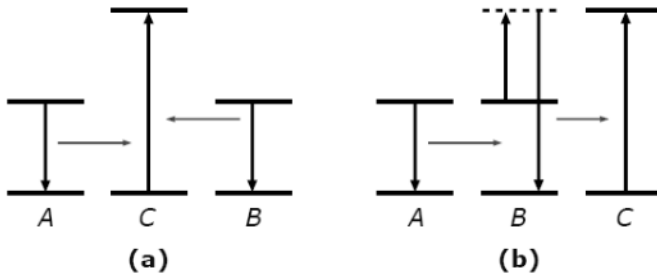
The absorption spectra of these single ions consist of a single line because they originate from  $4f$  intraconfigurational transitions, and  $4f$ - $4f$  transitions are not allowed since the initial and final state have the same parity; instead, a mixture of opposite-parity states into the  $4f$  level bypasses the selection rule, explaining the observed intensities of the  $4f$ - $4f$  transitions [AART 09].

Different types of energy transfer, both radiative and non radiative, can occur between two ions when two or more ion types are present, co-doped, within the same host material. Mechanism (a) in figure 3.25 is radiative, while mechanisms (b-d) are not. In particular, mechanism (b) is resonant, mechanism (c) involves a phonon emission or absorption to compensate the energy mismatch, mechanism (d) transfers only part of the energy via cross relaxation.

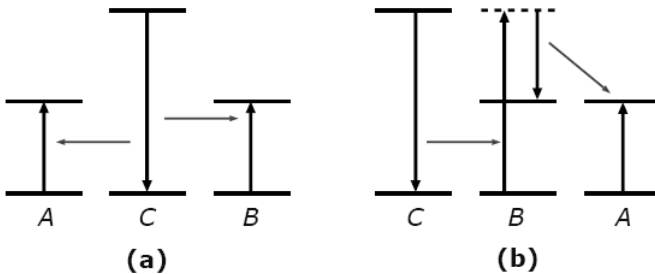


**Figure 3.25.: Schematic representation of some energy transfer mechanisms: (a) Radiative energy transfer; (b) Non-radiative resonant energy transfer; (c) Phonon-assisted non-radiative energy transfer; (d) Cross-relaxation [AART 09]**

The Dieke diagram in figure 3.24 shows that lanthanide nanoparticles can be designed to obtain a huge amount of possible combinations exploiting both radiative and non radiative mechanisms, that could be cooperative or accretive processes when a resonant intermediate level is not present [JENK 00]. The cooperative mechanism involves the mediation of a central energy ion, whereas the accretive mechanism exploits a virtual energy level from one of the ions with a lower-energy excited state. The prevalence of either process depends on the architecture of the molecule. Figure 3.26 shows a sketch of cooperative and accretive forms of upconversion, and figure 3.27 shows an analogous sketch for downconversion.



**Figure 3.26: Energy level diagrams for a three-centre energy pooling: (a) cooperative mechanism, (b) accretive mechanism [ANDR 01].**



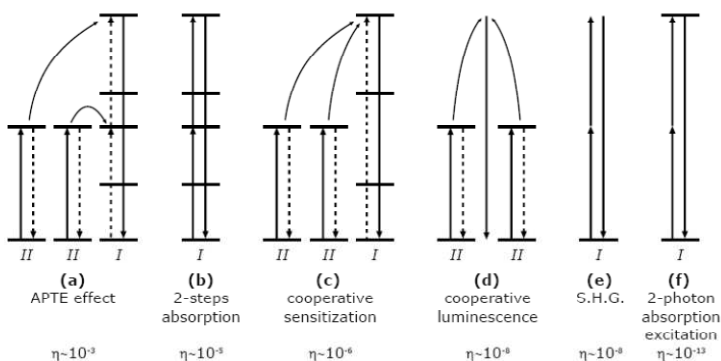
**Figure 3.27: Energy level diagrams for downconversion: (a) cooperative mechanism, (b) accretive mechanism [ANDR 01].**

The conditions that are required for the energy transfer are: a spectral overlap between the donor emission and the acceptor absorption (resonant condition); some interaction like exchange (wavefunction overlap) or multipole-multipole [BLAS 94].

All these transitions can lead to up- and down-conversion.

## 3.5.2 Up conversion

Up conversion is the process where two photons with a ‘small’ energy are ‘added up’ to obtain one photon with a ‘high’ energy [AUZE 04]. All previously described transitions could contribute to this phenomenon in the way illustrated by figure 3.28



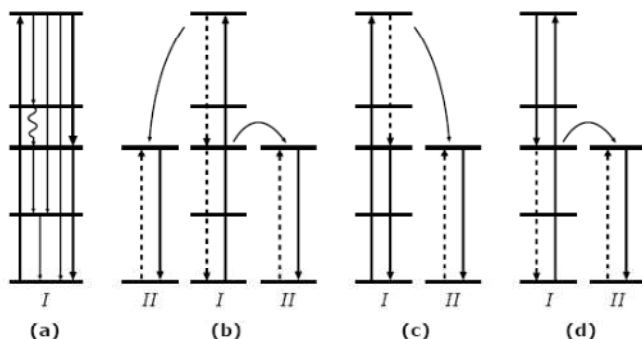
**Figure 3.28: Energy level schemes for some 2-photon upconversion mechanisms, with an indication of quantum efficiencies in  $\text{cm}^2/\text{W}$ . Solid vertical arrows indicate radiative transitions. Arrows connecting different ions and dashed arrows indicate energy transfer between ions [AUZE 90].**

## 3.5.3 Down conversion

Downconversion (DC) is the process where one photon with a high energy is ‘divided up’ to obtain two photons with a lower energy, which makes for even larger quantum yields than 100%. The mechanism involves a simultaneous energy transfer from a donor to two acceptors, each accepting part of the energy of the excited donor. The first couple of ions in which this behaviour was observed



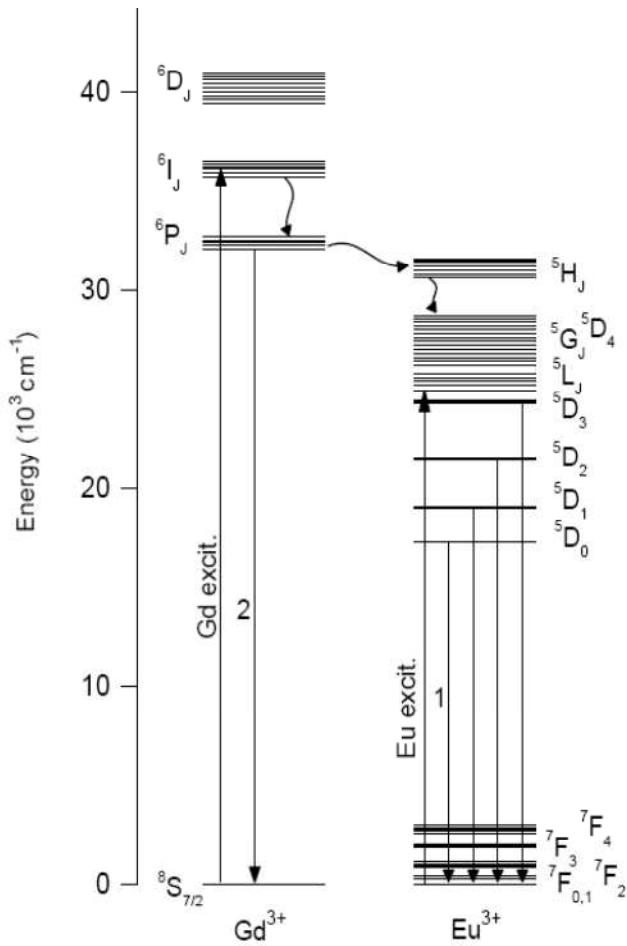
was  $\text{Gd}^{3+}\text{-Eu}^{3+}$  and, from the analogy with the two-step energy transfer process leading to upconversion, it was called 'downconversion' [WEGH 99]. Down conversion may be exploited to increase the efficiency of light-emitting devices (such as photomultipliers) or to increase the efficiency of solar cells [TRUP 02].



**Figure 3.29:** Schematic representation of some downconversion mechanisms. Solid vertical arrows indicate radiative transitions. Arrows connecting different ions and dashed arrows indicate energy transfer between ions. (a) Quantum cutting on one ion via cascade emission. Processes (b-d) occur on two types of ions. As a first step ion I is excited into a high energy level. From the high energy level energy transfer will excite the high energy level of the second ion of species II. Subsequently two photons will be emitted by two ions II, after a second energy transfer step (b), or by both ion I and II (c). Downconversion can also occur via emission of a photon by ion I, followed by energy transfer to an ion of species II (d) [WEGH 99].

### 3.5.4 $\text{NaGdF}_4:\text{Eu}^{3+}$

The downconversion process of the type in figure 3.29 (b) has been demonstrated for the phosphor  $\text{NaGdF}_4:\text{Eu}^{3+}$ . Upon VUV excitation in the 6GJ levels of the  $\text{Gd}^{3+}$ -ion, the energy is transferred to two  $\text{Eu}^{3+}$ -ions in two energy transfer steps resulting in emission from  $\text{Eu}^{3+}$ , mainly around 612 nm. Because of the weak absorption of the 6GJ levels of the  $\text{Gd}^{3+}$ -ion a significant part of the VUV radiation is not absorbed by  $\text{Gd}^{3+}$  but by the  $\text{NaGdF}_4$  host lattice and lost non-radiatively. The external quantum efficiency is therefore much lower and depends strongly on the presence of defect states in the host lattice [KARB 05]



**Fig.3.30. Schematic energy diagram for  $\text{Gd}_3\text{C}$  and  $\text{Eu}_3\text{C}$  ions in  $\text{NaGdF}_4$ . Only the levels which are relevant to the present study are included in this figure [KARB 05]**

## Bibliography

- [AART 09]  
L.Aarts, Downconversion for solar cells with lanthanide ion couples, PhD thesis, Leiden, 2009
- [ACDL]  
figure produced with ACD Labs software
- [ALDR 81]  
W.N.Aldridge, B.W.Street; Spectrophotometric and fluorimetric determination of tri- and di-organotin and -organolead compounds using dithizone and 3-hydroxyflavone, *Analyst* 106 (1981) 60-68
- [ANDR 01]  
D. Andrews and R. Jenkins, A quantum electrodynamical theory of three-center energy transfer for upconversion and downconversion in rare earth doped materials, *J. Chem. Phys.* 114 (2001) 1089-1101.
- [AUZE 04]  
F. Auzel, Upconversion and anti-Stokes processes with f and d ions in solids, *Chem. Rev.* 104, (2004) 139-174
- [AZUE 90]  
F. Auzel, Upconversion processes in coupled ion systems, *J. Lumin.* 45, (1990) 341-345
- [BEAC 78]  
William F. Beach: "A Model for the Vapor Deposition Polymerization of p-Xylylene". *Macromolecules* ,11(1),(1978) 72-76
- [BERA 00A]  
M. Bera, A. Rivaton, C. Gandon, J.L. Gardette: "Comparison

of the photodegradation of parylene C and parylene N”,  
European Polymer Journal 36 (2000) 1765-1777

- [BERA 00B]  
M. Bera, A. Rivaton, C. Gandon, J.L. Gardette:“  
Photooxidation of poly( para-xylylene)”. European Polymer  
Journal, 36, (2000) 1753-1764
- [BLAS 94]  
G. Blasse and B. Grabmaier, Luminescent Materials,  
Springer-Verlag, Berlin, Germany, 1994.
- [BOIL 08]  
S. Boileau, B.Boury, F.Ghanachaud, Silicon based  
polymer,advanced in synthesis and supramolecular  
organization, Springer 2008
- [BRUC 91 ]  
G. A. Brucker, D. F. Kelley, T. C. Swinney., Proton-transfer  
and solvent polarization dynamics in 3-hydroxyflavone ,J.  
Phys. Chem. 95 (1991) 3190–3195.
- [CART 03]  
S. Carturan, A. Quaranta, G. Maggioni, A. Vomiero, R.  
Ceccato, G. Della Mea, Optical Study of The Matrix Effect on  
the ESIPT Mechanism of 3-HF Doped Sol-Gel Glass, J. Sol-Gel  
Sci. Technol. 26 (2003) 931-935
- [CART 04]  
S. Carturan, A. Quaranta, G. Maggioni, M. Bonafini, G. Della  
Mea.; 3-Hydroxyflavone based wavelength shifting systems  
for near UV optical sensors,. Sens. And Act. A 113 (2004)  
288-292.
- [CONR 03]  
J.P.Conrad, J.C.Merlin; Comparison of the chelating power

- of hydroxyflavones, Journal Of Mol. Struct.651-653; (2003), 381-387
- [CROM 88]  
T.R.Crompton, A review of the analysis of organometallic compounds in the environment, Environment International, 14 (1988) 417-463
  - [DASR 08]  
R. DAS, A.S. klymchenko, G. Duportail & Y. Mely, Excited state proton transfer and solvent relaxation of a 3-hydroxyflavone probe in lipid bilayers; J Phys. Chem.B; 112 (2008) 11929-11935
  - [DIAM 05]  
P.R. Diamente, F.C.J.M. van Veggel: Water-soluble luminescent Ln<sup>3+</sup>-doped nanoparticles: retention of strong luminescence and potential as biolables, J. Fluorescence, 15 (2005) 543-551
  - [DIAM 06]  
P.R. Diamente, R.D. Burke, F.C.J.M. van Veggel; Bioconjugation of Ln<sup>3+</sup>-doped LaF<sub>3</sub> nanoparticles to avidin, Langmuir, 22 (2006) 1782-1788
  - [DIEK 63]  
G. Dieke and H. Crosswhite, The Spectra of the Doubly and Triply Ionized Rare Earths, Appl.Opt., 2 (1963) 675
  - [DIEK 68]  
G. Dieke, Spectra and energy levels of rare earth ions in crystals, Interscience Publishers, NewYork, 1968
  - [EVAN 06]  
F. Evanics, P.R. Diamente, F.C.J.M. van Veggel, G.J. Stanis, and R.S. Prosser; Water-Soluble GdF<sub>3</sub> and GdF<sub>3</sub>/LaF<sub>3</sub>

Nanoparticles – Physical Characterization and NMR Relaxation Properties, Chem. Mater., 18 (2006) 2499-2505

- [FENG 08]  
W. Feng, L. Lie, L. Xiang-Ping, Y. Ya-Xin, Z. Gui-Lan, C. Wen-Ju; All-optical switchings of 3-hydroxyflavone in different solvents, Chinese Physics B; 17 (2008); 1461-1467
- [FILA 93]  
United States Patent Number: 5,266,352; Filas et al. 4 Date of Patent: Nov. 30, 1993
- [GOTL 07]  
I. Yu. Gotlib, E. M. Piotrovskaya, S. W. de Leeuw: “Molecular Dynamics Simulation of Poly(p-xylylene): Bulk Phase and a Single Molecule”. J. Phys. Chem. C, 111 (2007) 6613–6620
- [HAMA 97]  
Y. Hamada, T. Sano, H. Fujii, Y. Nishio, H. Takahashi, . K. i Shibata.; Organic light-emitting diodes using 3- or 5-hydroxyflavone–metal complexes, Appl. Phys. Lett. ;Vol.71, n°23, (1997)3338-3341
- [HAMM 70]  
L.P. Hammett in Physical Organic Chemistry, McGraw-Hill, New York, (1970). 271
- [JENK 00]  
R. Jenkins and D. Andrews, Orientation factors in three-centre energy pooling, PCCP 2, (2000). 2837-2843
- [JURD 56]  
L. Jurd, T.A. Geissman; Absorption Spectra of Metal Complexes of Flavonoid Compounds, Journal of Organic Chemistry, (1956 );1395-1402
- [KARB 05]  
M. Karbowiaka, A. Mechb, A. Bednarkiewicz, W. Streffkb,

- L. Keffpin'ski, Comparison of different NaGdF<sub>4</sub>:Eu<sup>3+</sup> synthesis routes and their influence on its structural and luminescent properties, *Journal of Physics and Chemistry of Solids* 66 (2005) 1008–1019
- [KLAM 09]  
E. Klampaftis, D. Ross, K.R.McIntosh, B.S.Richards, Enhancing the performance of solar cells via luminescent down-shifting of the incident spectrum, *Sol. Eng. Mat and Sol. Cells*, 93 (2009) 1182-1194
  - [KUMA 01]  
S. Kumar, S.K. Jain, R.C. Rastogi, An experimental and theoretical study of excited-state dipole moments of some flavones using an efficient solvatochromic method based on the solvent polarity parameter, *ETN, Spectrochim. Acta A*, 57 (2001) 291-298
  - [KUMA 07]  
G. A. Kumar, C. W. Chen, J. Ballato, and R. E. Riman, Optical Characterization of Infrared Emitting Rare-Earth-Doped Fluoride Nanocrystals and Their Transparent Nanocomposites *Chem. Mater.*, 19 (2007) 1523-1528
  - [LACA 10]  
Ioana Lacatusu, Nicoleta Badea, Rodica Nita, Alina Murariu, Florin Miculescu, Ion Iosub, Aurelia Meghea, Encapsulation of fluorescence vegetable extracts within a templated sol-gel matrix, *Opt.Mat.*, 32 (2010) 711-718
  - [LEWI 98]  
J.E. Lewis, M. Maroncelli, On the\_uninteresting/dependence of the absorption and emission transition moments of coumarin 153 on solvent, *Chemical Physics Letters* 282 (1998)197–203



- [ROND 98]  
C. R. Ronda, T. Justel, H. Nikol, Rare earth phosphors: fundamentals and applications. *Alloys Compd.*, 275-277 (1998) 669-676
- [ROWA 08]  
B.C. Rowan, L.R. Wilson, B.S. Richards, Advanced material concepts for luminescent solar concentrators, *IEEE J. Sel. Top. Quantum Electron.* 14 (2008) 1312–1322.,
- [SASA 96]  
S. Sasaki and S. Nishi, Polyimides, fundamentals and applications, Edited by Ghosh and Mittal, Marcel Dekker Inc., 1996
- [SENG 79]  
P.K. Sengupta and M. Kasha, Excited state proton-transfer spectroscopy of 3-hydroxyflavone and quercetin, *Chem. Phys. Lett.* 68 (1979) 382-385
- [SENK 03]  
Jay J. Senkevich, G.-R. Yang, T.-M. Lu: “The facile surface modification of poly(p-xylylene) ultrathin films”. *Colloids and Surfaces A* Volume 216, Issues 1-3, ( 2003) 167-173
- [SIVA 05]  
S. Sivakumar, F.C.J.M. van Veggel, M. Raudsepp; Bright white light through up-conversion of a single NIR source from sol-gel derived thin film made with Ln<sup>3+</sup> doped LaF<sub>3</sub> nanoparticles *J. Am. Chem. Soc.*, 127 (2005) 12464-12465.
- [SIVA 06]  
S. Sivakumar, P.R. Diamente, and F.C.J.M. van Veggel; Silica-coated Ln<sup>3+</sup>-doped LaF<sub>3</sub> nanoparticles as new robust down- and up-converting biolabels, *Chem. Eur. J.* 2006, 12, 5878-5884

- [STRA 83]  
A.J.G. Strandjord, S.H. Courtney, D.M. Friedrich, P.F. Barbara, Excited-state dynamics of 3-hydroxyflavone , J. Phys. Chem. 87 (1983) p. 1125-1133
- [STRA 85]  
A. J. G. Strandjord, P. F. Barbara; The proton-transfer kinetics of 3-hydroxyflavone: solvent effects, J. Phys. Chem., 89(1985), 2355–2361
- [STRU 07]  
C.Strumpel,M.McCann,G.Beaucarne,V.Arkipov,A.Slaoui,V.Svrcek,C.del Canizo, I.Tobias, Modifying the solar spectrum to enhance silicon solar cell efficiency — an overview of available materials, Sol. Energy Mater. Sol. Cells 91 (2007) 238–249
- [TAKE 96]  
T. Takekoshi in Polyimides, fundamentals and applications, Edited by Ghosh and Mittal, Marcel Dekker Inc., (1996) 7.
- [TCAR 04]  
S.M.Carturan, Sol-gel based and polyimide based hybrid materials for radiation detectors applications, PhD Thesis in Chemistry, University of Trento 2004
- [TRUP 02]  
T. Trupke, M. Green, and P. Würfel, Improving solar cell efficiency by down-conversion of highenergy photons, J. Appl. Phys. 92, (2002) 1668
- [TURY 98]  
G. Túry, R. Vabrik, I. Kása, K. Papp, I. Rusznák, G.T. Szabó, A. Víg, E. Kálmán, Enhancement of fluorescent stability of 2,5-bis-2-(5-tert-butyl)-benzoxazolyl-thiophene (BBOT)

containing LDPE films., *Journal of photochemistry and photobiology A: Chemistry* 114, (1998) 51-58

- [WANG 07]  
J. Wang, Z. He, H. Mao, Y. Du, Y. Wang. Optical properties of BBOT-doped silica films prepared via sol-gel processing *Journal of Luminescence* 122-123 (2007) 268-271
- [wBAR 12]  
<http://environmentalchemistry.com/yogi/periodic/crosssection.html> retrieved last 15/03/12]
- [wBAS 09]  
[http://worldaccount.basf.com/wa\\_EU~en\\_GB\\_Catalog\\_Pigments\\_doc4\\_BASF\\_range\\_pl\\_col\\_dyes\\_lumogen\\_f\\_.pdf\\_title=&asset\\_type=ti\\_pdf&language=EN&urn=urn\\_documentum\\_eCommerce\\_sol\\_EU\\_09007bb280021ce6](http://worldaccount.basf.com/wa_EU~en_GB_Catalog_Pigments_doc4_BASF_range_pl_col_dyes_lumogen_f_.pdf_title=&asset_type=ti_pdf&language=EN&urn=urn_documentum_eCommerce_sol_EU_09007bb280021ce6) retrieved last 20/04/2009
- [wBAS 12]  
[<http://www2.basf.us/additives/pdfs/p3201e.pdf> 30-01-2012, retrieved last 30/01/12]
- [wCIC 09]  
<http://www.cicoil.com/pdf/GLIDRITECHEMDOC.pdf> retrieved last 12/09/09
- [WEGH 00]  
R. Wegh, A. Meijerink, R. Lamminmäki, and H. Jorma, Extending Dieke's diagram, *J. Lumin.* 87-89, (2000) 1002
- [WEGH 99]  
R. Wegh, H. Donker, K. Oskam, and A. Meijerink, Visible quantum cutting in LiGdF<sub>4</sub>:Eu<sup>3+</sup> through downconversion, *Science* 283, (1999) 663
- [wEXC 10]  
[www.exciton.com](http://www.exciton.com), last retrieved 14/07/2010

- [wKAP 11]  
<http://chem.chem.rochester.edu/~chem424/pimid1.htm>,  
last retrieved 23/12/11
- [WOLF 83]  
[O.S. Wolfbeis, pH-dependent fluorescence spectroscopy XVII: First excited singlet state dissociation constants, photoautomerism and dual fluorescence of flavonol, J. of Photochem. , 21 (1983) 67-79
- [WOOL 81]  
G.J. Woolfe and P.J. Thistlethwaite, Direct observation of excited state intramolecular proton transfer kinetics in 3-hydroxyflavone, J. Am. Chem. Soc. 103 (1981) p. 6916-6923.
- [wSCS 11]  
[www.scscoatings.com/parylene\\_services/index.aspx](http://www.scscoatings.com/parylene_services/index.aspx)
- [wVPS 11]  
<http://www.vp-scientific.com/solvent.htm> retrieved last  
11/10/11

# CHAPTER 4

## Results

---

### *4.1 Introduction*

This chapter is devoted to the analysis of the collected experimental data and is divided in two main parts, respectively focused on optical characterisation (absorption, transmission, fluorescence, IR, XRD) and electrical measurements (I-V curve).

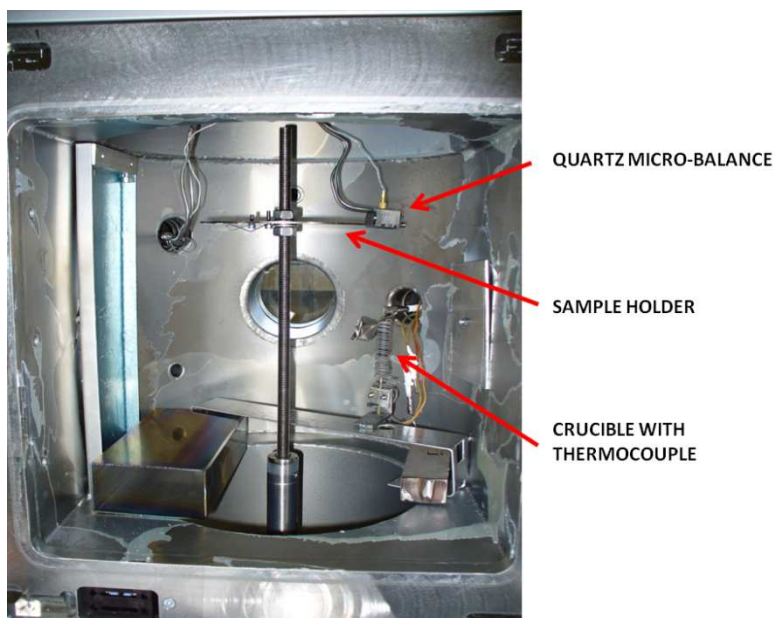
In the first part of the chapter numerous potential combinations of dyes and matrices are examined. Not all of these combinations were thoroughly investigated; the rationale for the selection that we operated is provided at the end of the first part, in a dedicated summary. The first part of the chapter closes the work segment focused on the choice of dye and matrix and introduces the second part, in which application-oriented measurements are presented. In the last part, in fact, the results that were obtained testing the materials on actual solar cells are reported.

# First Part

---

## *4.2 Parylene based samples*

An overview of the production and properties of parylene was provided in chapter 3; this chapter focuses on the specific experimental work which was performed on the material in this project. The experimental equipment used for the deposition of the dye-containing parylene-C (Pc) films was a PPCS Labcoater LC300 (PPS, Germany). The chamber was customized for the co-deposition of the parylene monomer and dye, by adding a crucible in the deposition area.



**Figure 4.1: Parylene-customised deposition chamber.**

Prior to co-deposition, the sublimation rate vs temperature curve of the dyes was measured with a quartz crystal microbalance and AFM thickness measurements. Hence, dyes were sublimated at a pre-determined temperature in order to get a steady and appreciable deposition rate. The films were deposited on two different substrates: p-doped (100) silicon wafers lapped on both faces (Bayville Chemical Co., USA) for fluorescence measurements and glass slides (Vetrotecnica, Italy) for optical absorption measurements.

## 4.2.1 Parylene: deposition parameters

The two types of parylene that we examined were parylene N and C. The deposition parameters, reported in table 4.1, were slightly different for the two types. Monomers were respectively evaporated at 150°C (parylene N) and 135°C (parylene C); the pyrolysis temperature, at which the dimer divides into two single monomers, was 650°C and 700°C, respectively. When the single unit was drawn from the oven it was deposited on a cool surface in the chamber at room temperature. Films of 360 nm were generally obtained when 2.5 g of dimer powder were used, while the average thickness was 300 nm when a dye was co-deposited, because of the local heating produced by the crucible. The deposition rate is in fact proportional to the substrate temperature: thickness increases with decreasing temperature, and the presence of the crucible at high temperature resulted in the creation of a warmer zone that induced a reduction in the polymer deposition rate. The quartz micro balance could not be used during parylene deposition because the polymer tends to stick the quartz, thus inhibiting measurements.

**Table 4.1: Deposition parameters of parylene**

<i>type</i>	<i>T. evap.</i>	<i>T. pyrolysis</i>	<i>Pressure</i>	<i>Powder quantity</i>	<i>Medium thickness</i>
<b>Parylene N</b>	150°C	650°C	6 Pa	2.5 g	360 nm
<b>Parylene C</b>	135°C	700°C	3.6 Pa	2.5 g	375 nm

Once the principal deposition parameters were set, the co-evaporation of some dyes was possible. To obtain these results the chamber was modified adding, as mentioned above, a crucible with



a thermocouple and a heater resistance that was connected to a temperature controller. The voltage used to heat the crucible was fixed at 12 V.

Propaedeutical to co-deposition, some evaporations of pure dye were performed in order to define the optimal deposition parameters for the fluorescent molecules. In order to obtain the pressure that would be later had in the deposition a valve was mounted between the rotative pump and the mechanical trap. In fact, during the parylene deposition the pressure in the chamber was around 6 bar, while it was only 2 bar when the dye alone was evaporated; with the introduction of the valve the delivery capacity decreased, increasing the pressure. A quartz microbalance was used to monitor the evaporation rate of the dye.

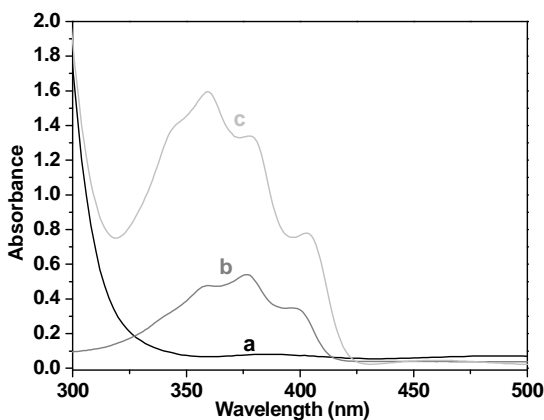
Numerous dyes capable of sublimation, mentioned in the previous chapter, were deposited in the course of this project; the experimental details of the process and the optical characteristics of the dyes are presented below.

### 4.2.2 Parylene N and BBOT

Parylene (both N and C) is strongly absorbent of wavelengths below 300 nm, but this absorption has a minimal influence on our application, as solar light power is negligible below 300 nm.

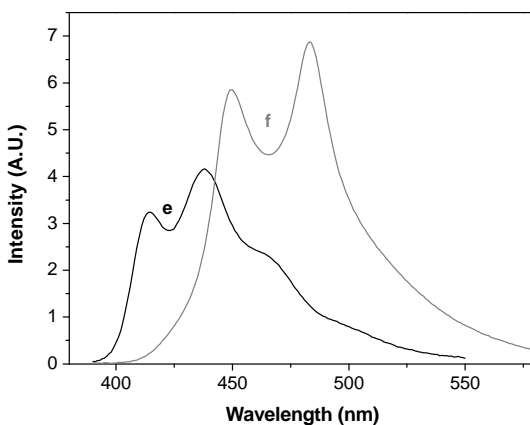
In figure 4.2 a comparison between absorption by a thin film of parylene N (a),  $10^{-5}$  mol of BBOT dissolved in  $CHCl_3$  (b) and a parylene N film doped with BBOT (c) are reported. Absorption peaks are present in a range between 320 nm and 420 nm; the ratio between the peak heights varies because the concentration in the film is very high and aggregations are possible, and because of UV

absorption from the parylene matrix. The absorption spectrum of the BBOT solution in cyclohexane, according to literature [BERL 71], ranges from 320 to 410 nm. In this case an asymmetrical absorption band appears from 310 to 410 nm, with its maximum at 378 nm and two lower peaks at 360 and 403 nm. In the case of BBOT-containing parylene films the absorption peaks are very similar but the prevalent peak is located at 360 nm rather than 378 nm, which evidences the different state of the dye molecules between film and diluted solution. In fact, when the concentration is sufficiently high, the interaction between the BBOT molecules becomes important and the electronic energy levels of the molecules can be strongly affected; all dye-doped parylene samples share this characteristic [MAGG 09].



**Figure 4.2:** Absorption spectra of a thin parylene N film (a), a solution of  $10^{-5}$  mol in  $\text{CHCl}_3$  of BBOT (b) and a film with parylene and BBOT(c).

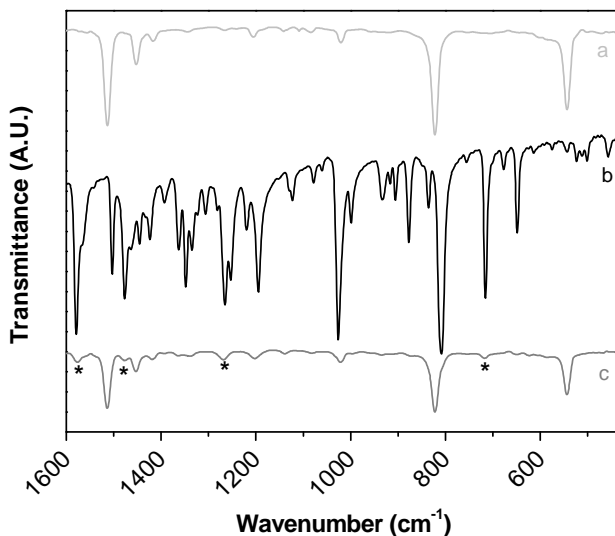
As shown in figure 4.3, when the incident wavelength is 380 nm emission peaks are red-shifted, the solution spectrum has two main peaks at 414 nm and at 437 nm with two small shoulders at 460 and 480 respectively, while the doped film emission spectrum displays maxima at 450 nm and 483 nm. The luminescence emission is in agreement with literature [BETL 71]; the low-concentration solution has a central peak at 437 nm and a minor peak at 414 nm and two small shoulders near 460 nm and 480 nm. Aggregation phenomena take place when the concentration increases, so that peaks are red-shifted, as occurs in BBOT-doped sol-gel derived glasses [WWAN 07].



**Figure 4.3:** Emission spectra, produced by an incident wavelength of 380 nm, by the  $10^{-5}$  mol BBOT in  $\text{CHCl}_3$  solution (e) and a parylene N + BBOT film (f)

*4.2.3 IR-analysis Parylene + BBOT*

In figure 4.4 the FT-IR transmission spectra of a BBOT-containing parylene film, a parylene N film deposited on Si Bayville and BBOT in a KBr pellet are reported. No evidence of appreciable interaction between the parylene matrix and the BBOT molecule can be detected within the sensitivity limits of this technique. The dye peaks are present in the matrix, but they are very weak if compared to those of parylene; although not all the peaks are clearly identifiable, the most prominent ones are located at 1578, 1477, 1267 and 716  $\text{cm}^{-1}$  (these peaks are marked with asterisks in figure 4.4); two other peaks may be seen as shoulders of the parylene peaks at 1030 and 811  $\text{cm}^{-1}$ . A more detailed analysis of the parylene peaks is given in the appendix. The presence of damaged molecules seems to be ruled out (within the detection limits of the analysis technique), as the peaks present in the BBOT-in-KBr spectrum and those present in the evaporated BBOT spectrum seem to coincide.



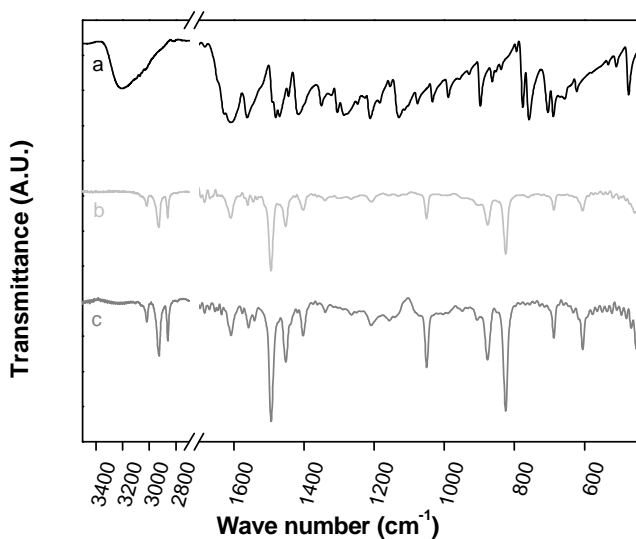
**Figure 4.4:** FT-IR spectra of a parylene N film (a), BBOT in KBr pellet (b) and a parylene film doped with BBOT (c).

When the absorbance of the parylene film becomes of some relevance the identification of the peaks in the absorption spectrum (see figure 4.2) may be affected by a high uncertainty, and for this reason an indicative quantitative analysis was carried out on the basis of the infrared peaks, that do not suffer from this problem. A calibration curve using KBr pellets was obtained measuring the amount of KBr and dye and normalizing the area under the curve to the area of non-overlapped BBOT peaks. In this way concentrations could be calculated for the produced parylene+BBOT samples.

Through the intensity of peaks and the calibration curve it was possible to determine the concentration of BBOT in film, which was estimated to be  $36 \text{ mg/cm}^3$ .

## 4.2.4 Optical of parylene C + 3HF

No IR analysis was possible on the parylene C and 3HF samples because the main peaks of 3HF and parylene C overlap, making it impossible to determine the amount of dye; interactions between the matrix and the dye could not be observed, on the other hand, because no new peaks were visible. In figure 4.5 all three spectra are shown for comparison (see a detailed description in the appendix). Again, the spectrum of the evaporated molecule could not be distinguished from the one obtained using KBr, which seems to rule out the presence of any damage in the molecule structure.



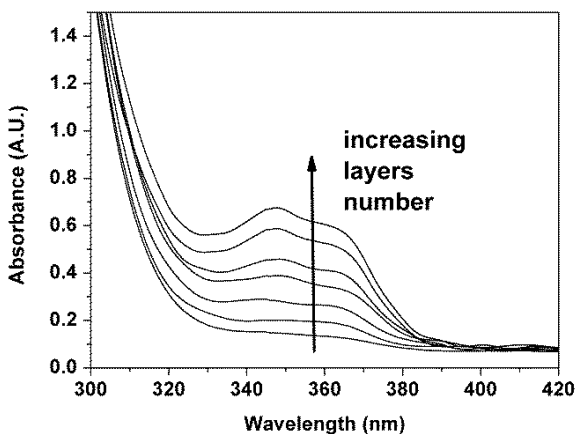
**Figure 4.5:** Transmission IR spectra of 3HF in a KBr pellet (a), of parylene C doped with 3HF (b) and of pure parylene C (c).

### 4.2.5 Deposition parameters

The extent of adhesion between thin parylene films and cell surfaces and the limited number of cells available to us imposed a severe constraint on the number of dye-matrix combinations that could be studied within the scope of the present project. For this reason after some exploratory study the decision was taken to focus all efforts on the sole combination 3HF+Parylene C. This combination was chosen by virtue of its very high Stokes shift and was deposited on different cells characterized by a higher efficiency at 530 nm (3HF emission) than 450 nm (BBOT emission).

Different depositions were carried out to optimize the probability that the spectrum of the incoming light would be altered so as to be optimally exploited by the solar cell. This aim could be accomplished increasing concentration and thickness up to, respectively, the solubility and transparency limit.

Absorption increases with the number of layers, as shown in figure 4.6. It is evident that absorption mostly takes place between 320 nm and 380 nm; absorption by the Zeus glass used to support the thin films is also visible, which suggests that the 3HF is present in its predominant tautomeric form [TOMM 04].



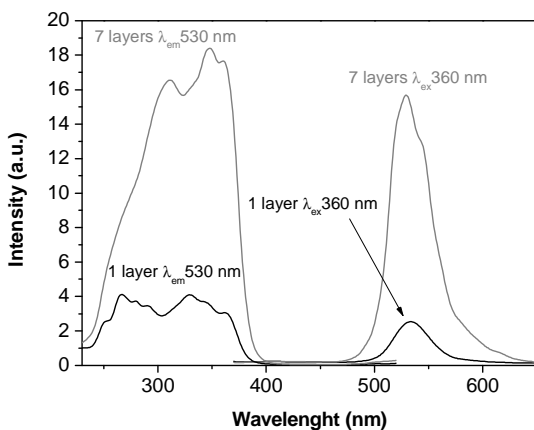
**Figure 4.6:** Absorption of a 3HF-embedded parylene C film. The lowest-lying curve corresponds to a one-layer sample while the highest-lying curve corresponds to a 7-layer deposition.

Fluorescence spectra confirm that the prevalent 3HF form is the tautomeric one, in fact as reported in figure 4.7 when the incident wavelength is 360 nm emission peaks around 530 nm and no other peaks are present. Increasing the thickness (and, therefore, the amount of dye) the emission intensity increases (the two measurements were performed exactly in the same configuration so as to obtain easily comparable results). The dominance of the tautomeric form is a signal that the radical polymerization between monomers does not involve the dye, which is therefore not influenced by the process; no interaction takes place with the surrounding matrix.

The results that we obtained from emission and excitation measurements, on the other hand, were not completely



satisfactory, as the intensity of the dye systematically decreased in time. This effect can be attributed to photo-oxidation mechanisms with a triplet state of the dye molecule. At lower concentration the excitation spectra were affected by the presence of the matrix, that has a small fluorescence emission around 350 nm when excited in the proximity of 270 nm; this can cause the deformation of the one-layer excitation spectrum, as an energy transfer can occur between the dye and the matrix.

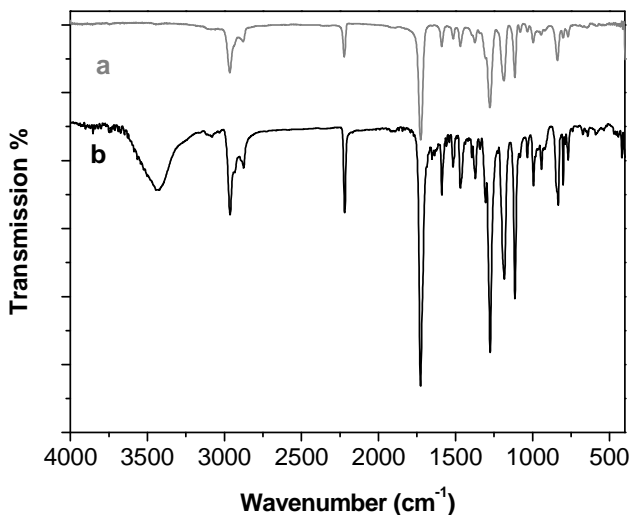


**Figure 4.7: Fluorescence spectra of 3HF embedded in parylene C, obtained from seven-layer and one-layer samples.**

#### 4.2.6 Evaporation of Lumogen yellow 083

Test depositions of Lumogen yellow 083 were also carried out in order to try to construct a multi-layer device characterized both by wide-range absorbance and large wavelength shift.

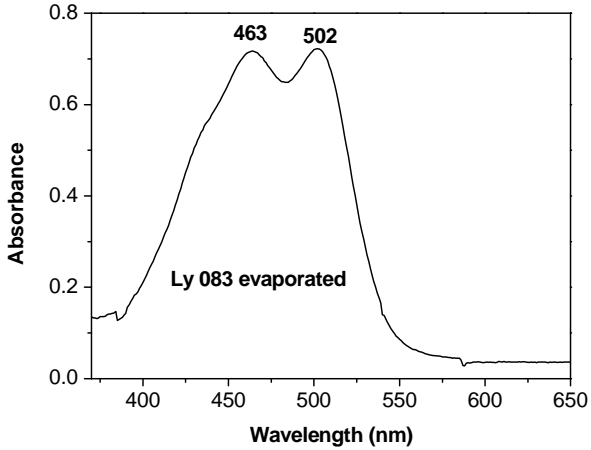
Lumogen yellow 083 was evaporated at the temperature of 225°C and the pressure of some Pa. In figure 4.8 are reported the IR spectra of the molecule in a KBr pellet (b) and evaporated (a). All the expected peaks are present except the broad band between 3200  $\text{cm}^{-1}$  and 3700  $\text{cm}^{-1}$ , ascribed to intramolecular OH bond. Considering that there are no evident variations of the IR spectra and that the structure of the molecule is patent protected, no other peak assignment was done.



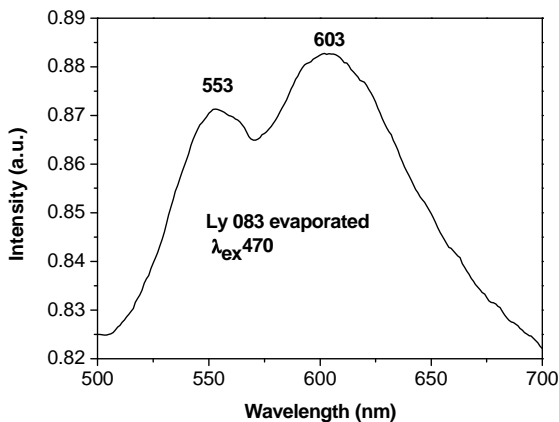
**Figure 4.8:** IR spectra of (a) evaporated Ly083 and (b) Ly083 in KBr

The disappearance of the OH group is indicative of damage in the molecule; in fact, from the analysis of fluorescence spectra (figure 4.10) it is evident that emission is weakened, and that when the sample is excited by 470 nm light emission peaks at 553nm and 603

nm, which is indicative of a transformation at molecular level, as the emission of Ly 083 is expected to peak at 490 nm.



**Figure 4.9: Absorption curve of Ly083**



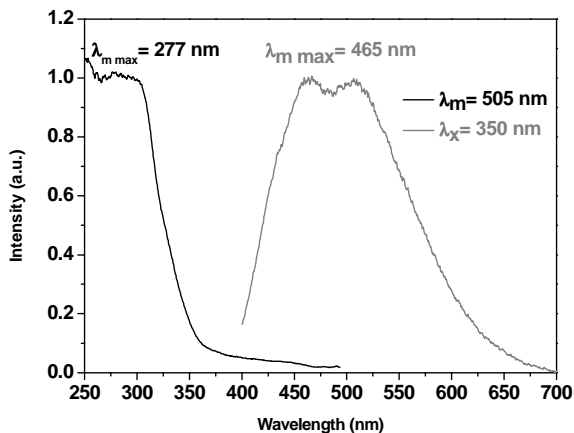
**Figure 4.10: Fluorescence spectra of evaporated Ly 083.**

Coumarines were not exploited because of their sensitivity to heat, which foreshadowed likely decomposition.

### 4.3 Fluorinated polyimide

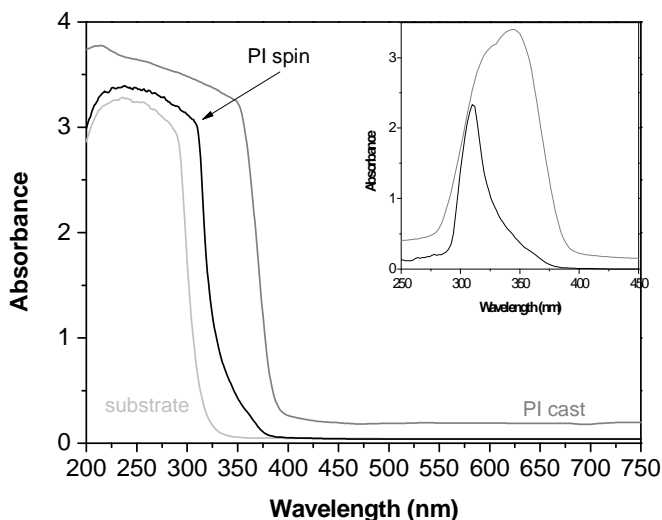
The procedure for the synthesis of polyimide 6FDA-DAD (PI) is described in chapter 3 and in ref [CART 09]. The flakes of produced PI were dissolved in N-methyl pyrrolidone (NMP) with the dye and then deposited on a glass slide via spin-coating and/or drop casting. Spin-coated samples were 1.4  $\mu\text{m}$  thick, whereas the sample obtained by casting was 30  $\mu\text{m}$  thick.

Polyimide has an intrinsic fluorescence: this matrix absorbs in the UV range around 230-350 nm and emits in the range 400-500 nm, with a maximum at 465 nm [CART 09]. This matrix, of rather remarkable properties for our purpose, was tested with several dyes.

Excitation/Emission spectra of 6FDA/DAD deposited on SiO<sub>2</sub>**Figure 4.11: Fluorescence of the 6FDA DAD matrix.**

#### 4.3.1 Polyimide+3HF

Samples were again produced via spin coating and casting. Comparison of the absorption spectra in figure 4.12 highlights a very different thickness. In fact the thicknesses of the spun and cast samples were, respectively, 1.4 and 30  $\mu\text{m}$ .

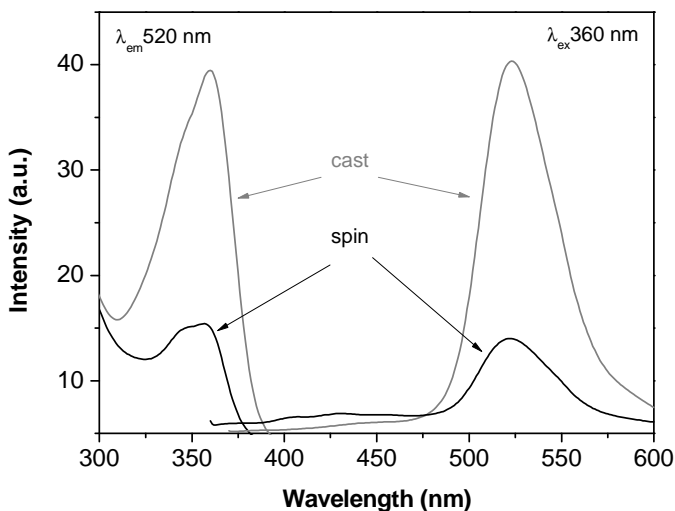


**Figure 4.12: Comparison between the absorption peaks of cast and spin coated samples with a dye amount of 1%; in the insert the difference between film and substrate evidences the contributions of dye and matrix.**

The only 3HF form visible in the fluorescence spectra, instead, is the green tautomeric one. In fact as shown in figure 4.13 the two peaks are very symmetric and there is no evidence of any other form; a small shoulder can be seen at 430 nm but, considering the high permeability of the polymer, humidity may be responsible for it.

Here the dye was dissolved with the polymer and the only physical phenomenon that could affect it was the evaporation of the solvent (usually DMF, NMP or DMSO). In polysiloxane and parylene, on the other hand, chemical reactions can take place after the dye is

added. In fact 3HF may be affected in polysiloxane by a reaction with a catalyst.



**Figure 4.13: Fluorescence spectra of 3HF in fluorinated PI**

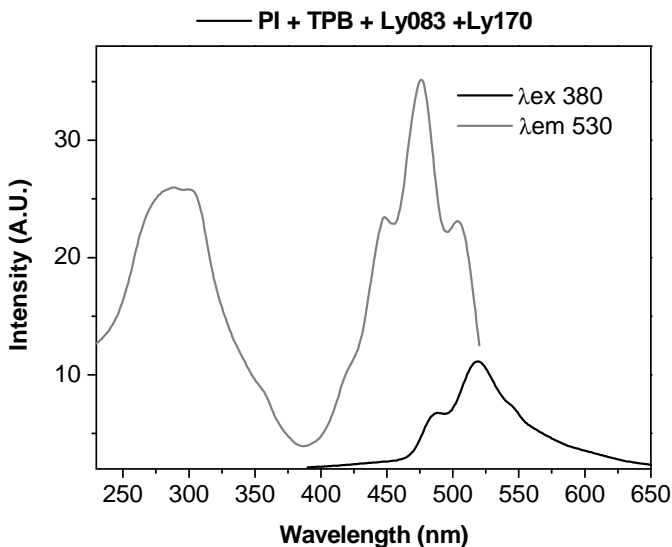
In fluorinated polyimide the dye concentration reached 2% wt: this is an upper bound for solubility, beyond which the transparency of the film is strongly affected, causing light scattering inside the film and, ultimately, poor transmission.

#### 4.3.2 Other dyes in Fluorinated Polyimides

Trying to produce samples with a wide absorption range and a final higher-wavelength emission, as explained in chapter 3, different combinations of dyes were considered. Lumogen dyes do not thoroughly cover the visible range, in particular because of a gap

between 430 nm (emission of Lumogen blue and violet) and 470 nm (absorption peaks of Lumogen yellow 083). In order to try to bridge this gap Coumarines were considered. Presumably because of the aforementioned thermal sensitivity of these molecules, however, no appreciable results were obtained.

Lumogen, instead, seems not to suffer from the problem in combination with polyimides, as can be deduced from the following spectra.

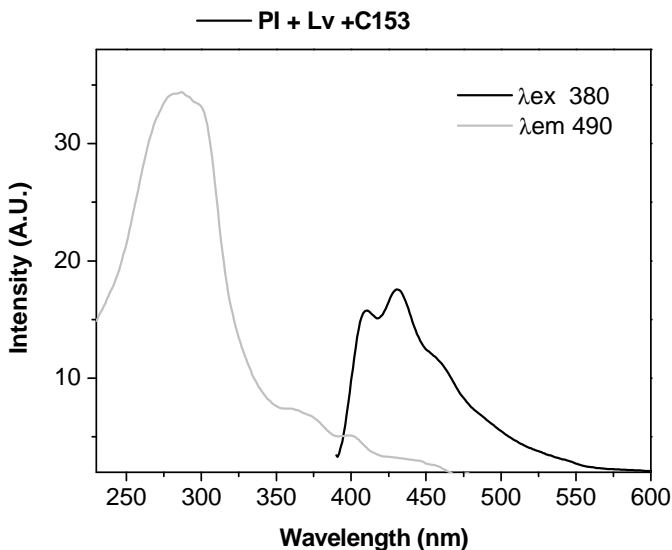


**Figure 4.14:** PI 6FDADAD samples with 0.06%TPB 0.025% Ly083 and 0.04% Ly170 exciting at 380 nm and emitting at 530 nm.

In figure 4.15 two spectra are visible, one measured exciting at 380 nm and the other emitting at 530 nm. The two contributions from lumogen are clearly visible and TPB (Tetraphenyl butadiene) is



hidden by polyimide emission; the contribution from TPB is visible in the shoulder.



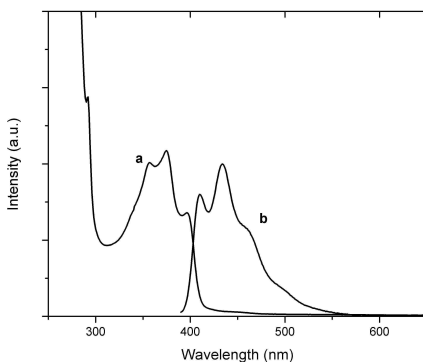
**Figure 4.15: PI with 0.05% Lv and 0.05% C153**

Figure 4.15 illustrates the behaviour of a sample of PI with 0.05% Lv and 0.05% C153. The presence of the Lv peak is very clear, while Coumarin 153 is not visible (it absorbs at 422 nm and emits at 530 nm). Here we measured emission spectra exciting at 380 nm and excitation spectra emitting at 490 nm.

## 4.4 Polysiloxane

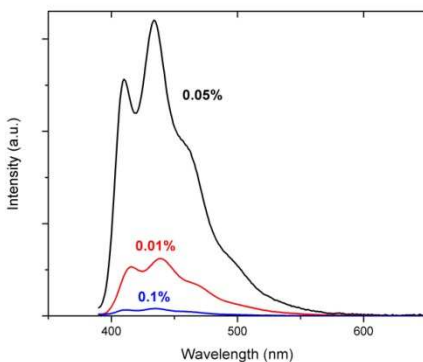
### 4.4.1 Optical characterizations of BBOT-containing polysiloxanes

The optical spectra of polysiloxane samples with BBOT are shown in figure 4.16. As in the case of the parylene samples, the spectra show that the polysiloxane matrix preserves the optical properties of the dye, without compromising its transparency at high wavelengths (above 500 nm). The absorption spectrum shows the typical band of BBOT, which closely resembles that of BBOT dissolved in  $\text{CHCl}_3$  (figure 4.16, spectrum b): the maximum peak is located at 374 nm with the two shoulders at 357 and 398 nm. This result indicates that the BBOT molecules are well dispersed inside the polysiloxane matrix and that the interaction between the molecules is negligible. This is confirmed by the emission features of polysiloxane samples (spectrum b in figure 4.16): the triple peak of BBOT can be clearly observed, with the maximum at 435 nm and the minor peaks at 410 and 458 nm.



**Figure 4.16: (a) Absorption spectrum of BBOT-containing polysiloxane film. (b) Emission spectra of BBOT-containing polysiloxane film ( $\lambda_{\text{ex}}=380\text{nm}$ )**

As shown in Figure 4.17, the presence of the emission band does not depend on the concentration of BBOT but the intensity of the emitted light does, increasing with increasing concentration from 0.01% to 0.05%, then decreases at 0.1%: taking into account that the thickness of the polysiloxane films was basically the same, this suggests that, differently from the BBOT-containing parylene films, there is a concentration-induced emission quenching and that the optimum concentration of BBOT is around 0.05%.



**Figure 4.17: Optical emission spectra of BBOT-containing polysiloxane films ( $\lambda_{\text{ex}}=380\text{nm}$ ) at different BBOT concentrations**

#### 4.4.2 Polysiloxane containing 3HF

Three different types of polysiloxane resin were chosen as matrices for embedding 3HF. The first one (labelled as PtCAT) is produced by the polyaddition of vinyl terminated diphenyl-dimethyl-siloxane copolymer (A) (22-25 % mol of diphenyl groups, viscosity 1000-1500 cSt) and methylhydrosiloxane - phenylmethylsiloxane copolymer, hydride terminated (B) (45 - 50% mol of phenyl groups, viscosity 75-110 cSt), catalyzed by Pt divinyltetramethyldisiloxane complex in xylene (Pt content 2.1 – 2.4 %).

The second one (labelled as SnCAT) results from a two-step polycondensation of silanol terminated diphenyl-dimethyl siloxane (C) (14-18 % mol of diphenyl groups, viscosity 50–60 cSt) and poly(diethoxysiloxane) (D), catalyzed by dibutyltin dilaurate (DBTDL).

The third system (labelled as ACET) is based on moisture-induced polycondensation without catalyst, involving a reaction between silanol terminated diphenyl-dimethyl siloxane (C) (14-18% mol of diphenyl groups) and methyltriacetoxysilane (E) (purity 95%).

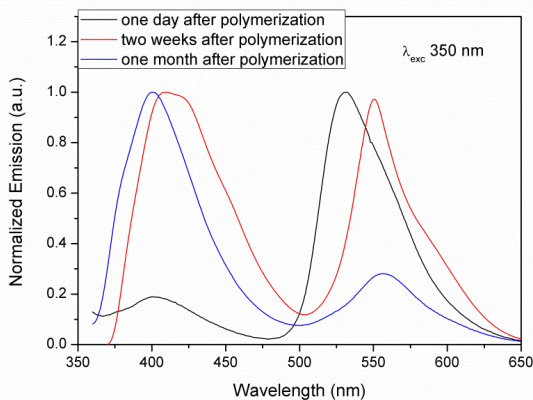
For each system, several experimental trials were performed in order to establish the best proportion between components in order to obtain transparent, bubble-free, non-sticky objects, which would be easily shaped by casting in polyethylene vessels and extracted without tear.

Excitation, fluorescence and absorption spectra were collected from both solid and liquid solutions of each component.

3HF powder was pelletized with anhydrous KBr and analyzed, whereas the interactions between 3HF and metal-based catalysts, Sn or Pt, were studied by dissolving a small amount of 3HF in the catalyst and pressing a drop of solution between two KBr windows. During the measurements, the sample compartment and the interferometer were evacuated to  $10^{-1}$  mbar to remove interference signals from water and atmospheric gases.

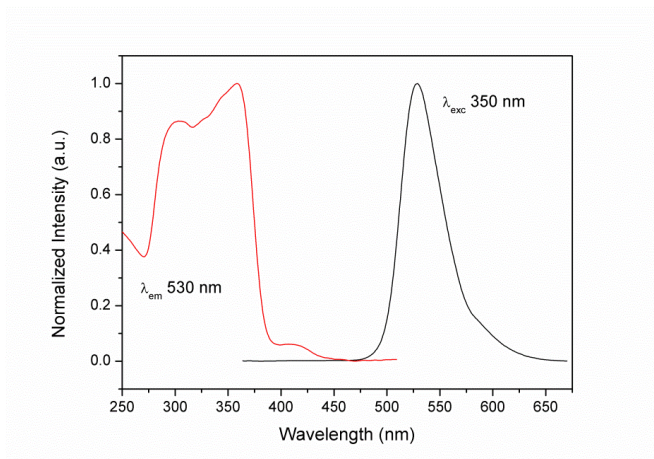
#### *4.4.3 3HF in polysiloxane, under Pt catalysis*

In 3HF-doped PtCAT polysiloxane matrices, obtained via polyaddition of vinyl terminated (component A) and hydride containing (component B) precursors catalyzed by Pt catalyst, the tautomeric form of 3HF is dominant, as proved by the fluorescence spectra of figure 4.18.



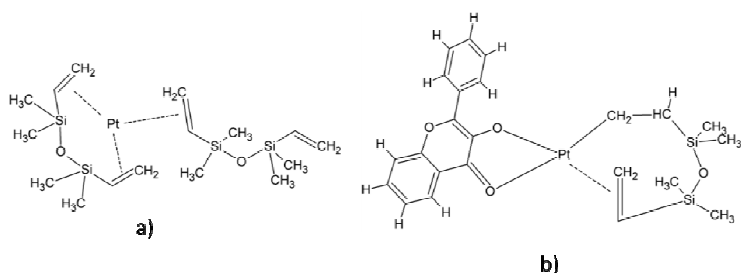
**Figure 4.18: Emission spectra of 3HF (excitation wavelength 350 nm) embedded in PtCAT polysiloxane at different times from cross-linking.**

The intensity ratio between the green and violet components decreases with time (see figure 4.18); after one month the main emitting form is the normal one, at about 400 nm. To explain this time evolution, emission and excitation spectra were collected after each step of the preparation route. The dye dissolved in component A is mainly present in the tautomeric form (figure 4.19, emission at 530 nm). The dye that was dissolved in the cross-linking resin (B component) does not present relevant changes in the fluorescence features (spectrum not reported). These facts suggest that the ESIPT equilibrium is shifted towards the violet-emitting component by interference with the Pt catalyst.



**Figure 4.19: Emission and excitation of 3HF dissolved in resin A of the PtCAT siloxane system.**

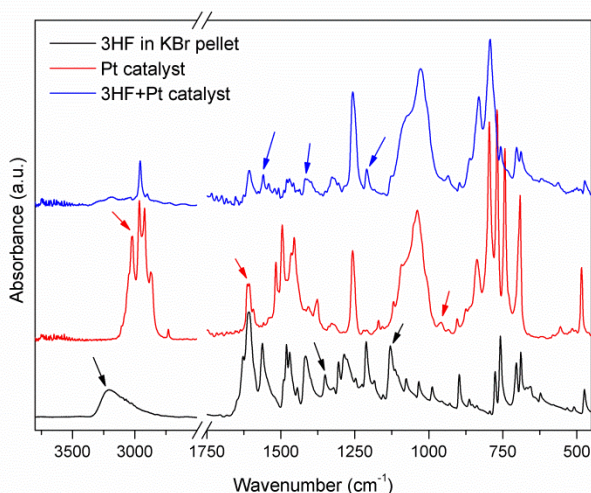
The hydrosilylation mechanism involves the coordination of a component terminal, double bond to Pt, promoting the addition of Si-H [CHAL 65]. Indeed, Pt complexes of siloxane are soluble in the resin and speed up the cross-linking reaction at low amounts of Pt (down to 1 ppm) in homogeneous catalysis conditions. The Karstedt catalyst used in this work (i.e. Pt divinyltetramethyldisiloxane, figure 4.20) is a  $d^{10}$  complex with coordination number 3, holding three olefin ligands coordinated to the central Pt(0). The reaction of this complex with 3HF may involve oxidative addition, with occurrence of a  $\beta$ -diketonate chelating ligand and H transfer to the olefinic end, ultimately resulting in a square planar  $d^8$  Pt species with one Pt-C  $\sigma$  bond and one Pt-olefin  $\pi$  bond (figure 4.20 b).



**Figure 4.20** a) The chemical structure of the Karstedt catalyst used in this work (2.5% Pt in xylene), b) proposed structure of a 3HF-Pt complex.

This proposed adduct between the Pt catalyst and 3HF is interpreted as resulting from direct addition of the catalyst to 3HF (see Experimental section). The solution was analyzed by FTIR (figure 4.21) and UV-Vis (figure 4.22).





**Figure 4.21: Infrared spectra of 3HF, a Pt complex used as a catalyst and their mixture. Data were stacked on the y axis for the sake of clarity. See text for details.**

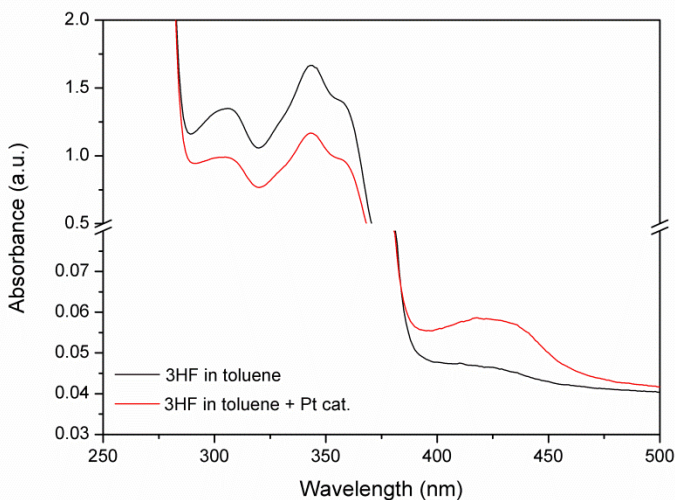
Though several works have been devoted to the IR spectroscopy of 3HF and derivatives, some peak assignments, particularly in the cases of C=O, C2=C3 (pyrone ring, see Fig. 4.20) and O-H stretching are still controversial. In 1962, Looker stated that the strong absorption at  $1610\text{ cm}^{-1}$  can be assigned to C=O stretching, while the same peak is shifted at  $1622\text{ cm}^{-1}$  in the spectrum of 3HF dissolved in  $\text{CCl}_4$  [LOKE 62]. Hayashi locates the C=O stretching of 3HF in the range  $1610\text{--}1620\text{ cm}^{-1}$  in KBr [HAYA 71], while 3HF isolated in an Ar matrix at 10 K displays C=O absorption at  $1652\text{ cm}^{-1}$  [PETR 02]. Vavra and co-workers [VAVR 08] collected gas-phase IR spectra of 3HF and assigned the strong peak at  $1616\text{ cm}^{-1}$  to C=O. Several authors ascribe the carbonyl signal shift to lower

frequencies in 3HF with respect to 5-hydroxyflavone to conjugation with C2=C3 bond of pyrone ring, or to chelation effects with the hydroxyl moiety [MWAN 07]. The assignment of the strong signals in the range 1600-1650  $\text{cm}^{-1}$  of the 3HF Raman spectrum is still debated [MWAN 07], though Protti and co-workers recently proved their interpretation to be in agreement with DFT theoretical calculations [PROT 08].

Limiting the discussion of IR spectra in figure 4.21 to the main features of the analyzed samples, the peaks of 3HF (KBr pellet) generally assigned to -O-H group (black arrows in figure 4.21) [VARV 08] at 3208  $\text{cm}^{-1}$  (broad, -OH stretching), 1350  $\text{cm}^{-1}$  and 1130  $\text{cm}^{-1}$  (-OH deformation) disappear in the spectrum of the Pt-3HF mixture, in agreement with the proposed structure of Figure 4.20b; as for the carbonyl stretching signal at 1607  $\text{cm}^{-1}$  (shoulder at 1627  $\text{cm}^{-1}$ ), no unambiguous conclusions can be drawn as related to the Pt adduct formation, because of the overlap with the olefinic C=C stretching at about 1600  $\text{cm}^{-1}$  of vinyl groups in the Pt complex, though the carbonyl signal from 3HF seems to disappear in agreement with the results of Kuntic and co-workers in the complex Pd(II)-quercetin [KUNT 98]. In the spectrum of the mixture, some peaks of 3HF are still visible (blue arrows) at 1560  $\text{cm}^{-1}$ , ascribed to C=C skeletal vibration of the A ring coupled with C2=C3 stretch mode [PROT 08], 1417 and 1210  $\text{cm}^{-1}$  (C=C stretching of A and B ring, C-H in plane bending) [MWAN 07], proving that the main 3HF structure is intact in the adduct.

Remarkable changes are also observed in the optical properties of 3HF (figure 4.22). The typical band I (310, 345 nm) and band II (235 nm) of 3HF in toluene undergo hypochromic shift as soon as the Pt complex is added, whereas a new component at about 430 nm

appears; this can be ascribed to the formation of Pt(II) complex [KATY 77, KUNT 98].



**Fig. 4.22: Absorption spectra of 3HF in toluene and in toluene plus Pt complex (y axis widened from 370 to 500 nm to highlight optical changes).**

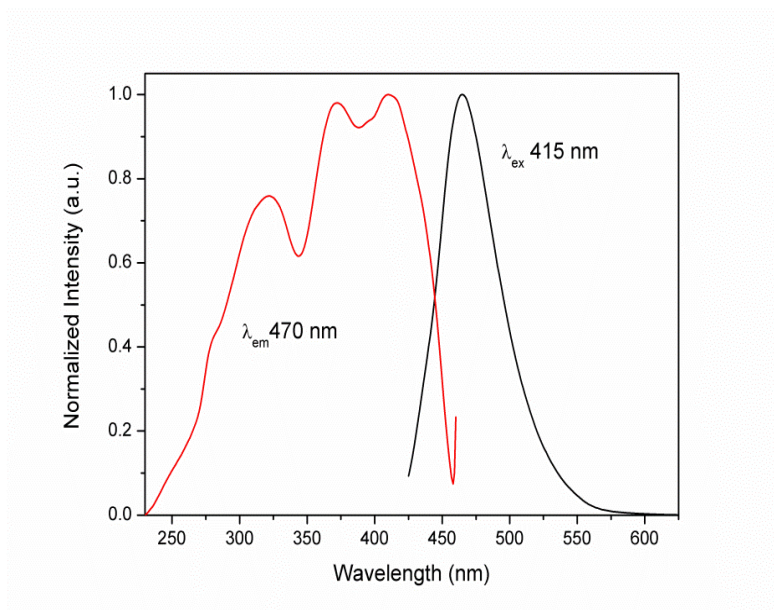
While optical and structural changes are immediately evident when 3HF and the Pt complex are mixed in direct contact, they take place only over several weeks in the siloxane matrix, which holds a very low Pt amount.

Embedding of 3HF in polysiloxane was performed by swelling the polysiloxane matrix in a 0.1 M solution of 3HF in acetone. After dipping, the sample displayed mainly the tautomeric, green emitting form and a minor violet emitting component due to the normal form. However, the intensity ratio between the tautomeric and the

normal form decreases in time, like in 3HF-doped PtCAT polysiloxane.

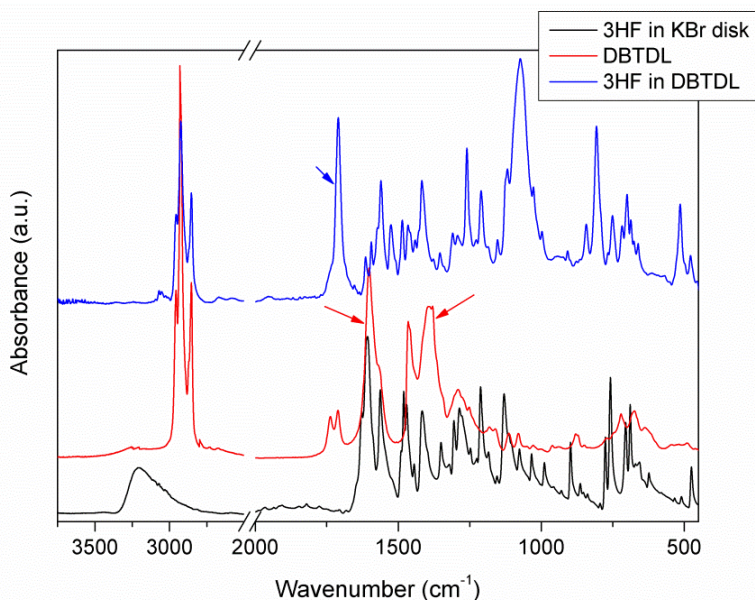
#### 4.4.4 3HF in polysiloxane, under Sn catalysis

SnCAT polysiloxane was used as a matrix to embed 3HF. As a first step, the dye was dissolved in component C; the emission spectrum (not reported) evidenced the tautomeric form as the most relevant one. After addition of component D and the tin catalyst, the resin promptly changed its colour to lemon yellow. After complete polymerization, the excitation and emission spectra of Fig. 4.23 were obtained. The main excitation bands shift from 350 nm to 380-420 nm and emission is centred at 470 nm. This instantaneous change may be ascribed to chemical interaction between 3HF and the tin catalyst. Indeed, while trying to swell 3HF-free SnCAT polysiloxane into a transparent solution of 3HF in acetone, it was observed that the whole liquid immediately turned yellow; moreover, a drop of pure tin catalyst added to a 3HF acetone solution produced an identical phenomenon.



**Fig. 4.23:** Excitation and emission spectra of SnCAT polysiloxane doped with 3HF.

As reported in the case of PtCAT system, a sample of 3HF with DBTDL was independently prepared. The FTIR spectra of this compound, pure DBTDL and 3HF are compared in Fig. 4.24.



**Fig. 4.24; IR spectra of 3HF, DBTDL and of the mixture of the two. Data were stacked on the y axis for the sake of clarity. See text for details.**

In the DBTDL spectrum, the strong signals from C-H stretching of butyl and laurate groups are visible in the range  $2950\text{--}2850\text{ cm}^{-1}$ . The strong peak at  $1600\text{ cm}^{-1}$  and the broad one at about  $1380\text{ cm}^{-1}$  (red arrows) correspond respectively to  $\nu_{\text{as}}(\text{COO}^-)$  and  $\nu_{\text{sym}}(\text{COO}^-)$  of the unidentate carboxylate coordination mode ( $\Delta\nu > 200\text{ cm}^{-1}$ ), according to previously reported data [TEOH 97, WENG 92, YOKO 80]. The 3HF-DBTDL product shows a drastic change in infrared features: the typical carboxylate peaks disappear while a conspicuous peak, assigned to free carboxylic acid [YOKO 80], appears at  $1710\text{ cm}^{-1}$  (blue arrow), which is assigned to free carboxylic acid [YOKO 80]. Moreover, the broad band assigned to –OH stretching of 3HF at  $3208\text{ cm}^{-1}$  is no more visible. Therefore, it

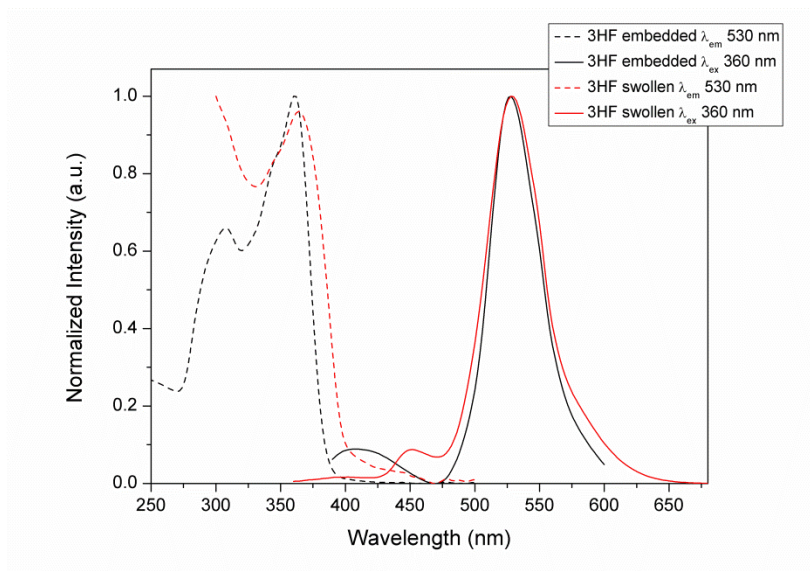
can be concluded that the anionic form of 3HF substitutes the laurate ligands in Sn(IV) coordination, as confirmed by the presence of free dodecanoic acid and by the optical spectra of Fig. 4.23 (anionic form of 3HF).

### 4.4.5 3HF in moisture-cured polysiloxane

The polysiloxane sample ACET was prepared by dissolution of 3HF in C component and subsequent addition of triacetoxysilane to trigger the cross-linking reaction.

Upon excitation at 360 nm, the most intense component is the green one (Fig. 4.25). The structural integrity of the 3HF molecule is preserved and the ESIPT mechanism is enabled without significant perturbations induced by coordination with metals or acid/base interactions with the siloxane precursors. A minor violet component from the normal form is visible at about 420 nm. Optical features are preserved in time: the intensity ratio between the green and violet components was found to be constant one month after the synthesis.

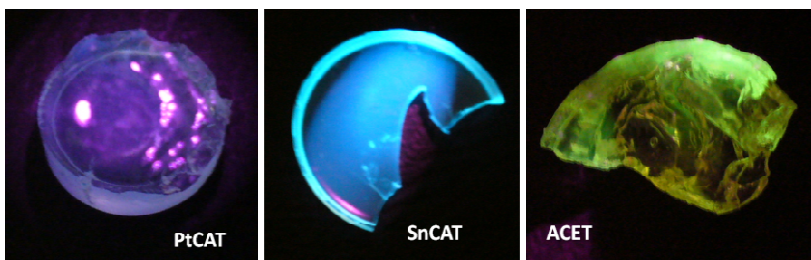
Introduction of 3HF by swelling, using the previously described technique, was performed. The excitation and emission spectra of this material are also reported in Fig. 4.25, where the main fluorescence component arises from the tautomer.



**Fig. 4.25: Emission and excitation spectra of 3HF in ACET polysiloxane.**

Fig. 4.26 compares the three types of 3HF-embedded polysiloxanes in their emission spectra upon excitation in the UV region. The ACET sample displays a strong green emission, thus proving that in this case the high Stokes shift typical of the 3HF tautomer is fully enabled; for PtCAT, the violet component from the normal form is dominant; the SnCAT sample shows the typical light blue emission of the anionic form. It must be highlighted that the pictures in Fig. 4.26 were collected from samples stored at ambient conditions after six months from the room-temperature vulcanization (RTV) reaction.





**Fig. 4.26:** 3HF-loaded polysiloxanes from different RTV upon exposure to UV light ( $\lambda_{\text{ex}}=380$  nm).

We have so far described different routes for 3HF embedding in polysiloxanes for the purpose of obtaining WLS systems with high Stokes shift. The 3HF ESIPT mechanism is heavily affected by the polymerization chemistry. The commonly used RTV of siloxanes, Pt-catalyzed polyaddition, produces a strong green emission as soon as the cross-linking reaction takes place; nevertheless, the emission band of the normal (violet emitting) form becomes gradually prevalent with time. The shift of the ESIPT equilibrium towards this form is attributed to the formation of a coordination compound between Pt and 3HF. The tin-catalyzed matrix with dissolved 3HF dye is also affected by chemical interaction between Sn and 3HF, resulting in deprotonation of 3HF, so that the most intense emission is found in the light blue region typical of the anionic form.

Experiments with acetoxy-based matrices evidence that this polycondensation can successfully be used to dissolve 3HF, while preserving its optical features. In addition, the time evolution of the optical features demonstrates that a steady green emission can be obtained without significant intensity losses six months after the

synthesis. Therefore, the possibility to entrap 3HF in siloxanes, derived from acetoxy polycondensation, is herein proved, suggesting that application as a WLS system with high Stokes shift is possible. Similar results were obtained via swelling.

#### 4.4.6 *Polysiloxane doped with Lumogen*

Lumogen dyes in polysiloxane display a behavior similar to that of 3HF. Several Lumogen fluorescence spectra are shown in the appendix. They were collected immediately after the production of the samples and one year later, and they evidence a transformation of the dye that points at an interaction between the catalyst and the dye. A gradual change in the colour of the dye, influencing the fluorescent emission, was actually noticeable during polymerization already.

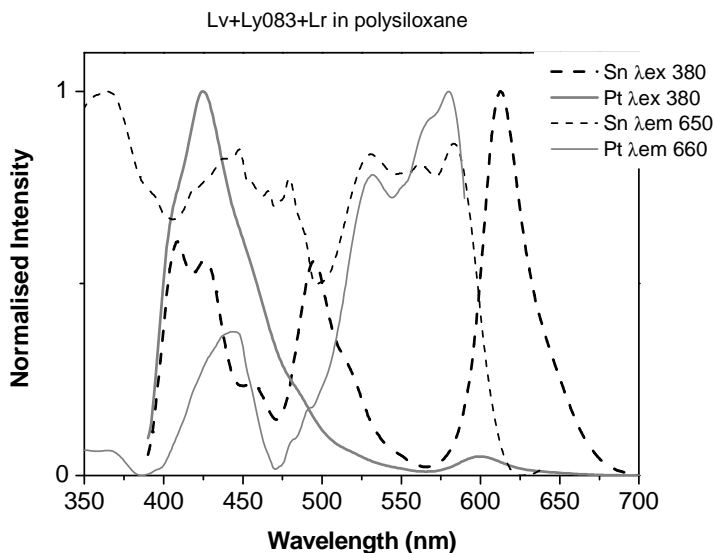
Alongside the spectra that we measured, spectra taken from literature are also presented in the appendix. Some appreciable variations in shape are highlighted.

As in the case of 3HF, it is most probable that the platinum catalyst produces some chemical modification on the molecule, creating complexes that affect the optical properties.

Lumogen® F Red 305 (Lr) is one of the most promising molecules of the Lumogen series for optical solar concentrators.

Two samples were produced with a combination of the same three dyes (Lumogen violet, Lumogen Yellow 083 and Lumogen Red) in Pt-catalysed polysiloxane and in Sn-catalysed polysiloxane. As shown in figure 4.27 the emission from Lumogen in the Sn-catalysed siloxane is in good agreement with literature data, while the peaks in the Pt-

catylased polysiloxane spectrum are either weaker than expected (Lumogen yellow 083) or shifted, as in the case of Lumogen red that emits under 600 nm rather than 610 nm, like it does in Sn-catalysed polysiloxane.



**Figure 4.27** Fluorescence spectra of a mixture of Lumogen violet, Lumogen yellow 083 and Lumogen red in Pt and Sn-catalyzed polysiloxane.

The efficiency of Lumogen red is quite high [KLAM 09]. The photostability is higher than that of other BASF Lumogen [wBAS 12].

Tanaka et al. [TANA 06] studied the properties of Lumogen red and orange and their photo-oxidation and photo-reduction. An equilibrium exists between the two forms; the photo reduced dye has a lower fluorescence than the photo oxidated one (type II

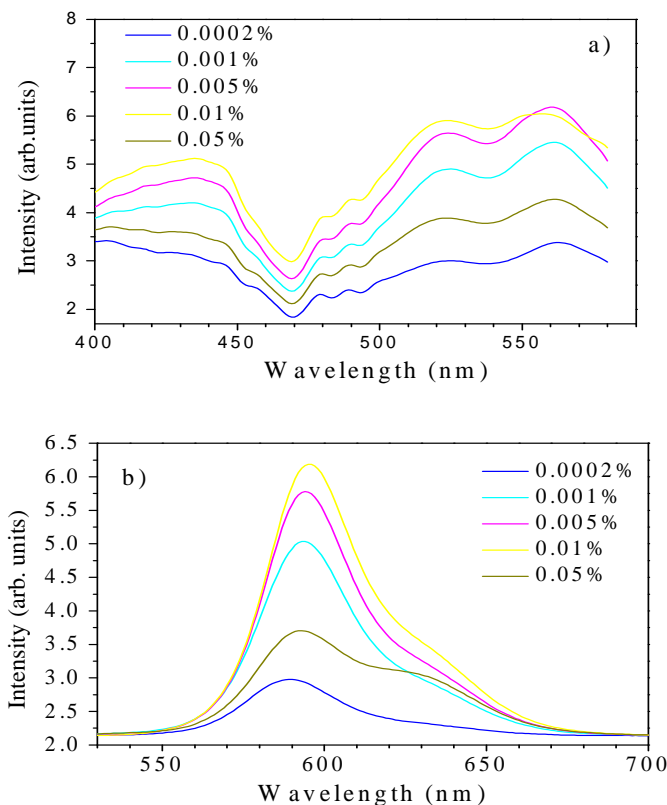
photooxidation). Photodegradation takes place when the two phenomena became irreversible.

LR was used in the past in poly(methylmetacrylate) (PMMA), poly(carbonate) PC and other studies [TANA 06, KIND 07, SLOO 07] as a doping molecule for luminescent concentrators.

#### *4.5 Lumogen red in LSC*

The absorbance spectra of the doped samples are characterized by a peak at 565 nm, whose amplitude increases with concentration. The qualitative comparison of fluorescence intensity in figure 4.28 shows that the light yield tends to increase with concentration up to 0.01%, then decreases.

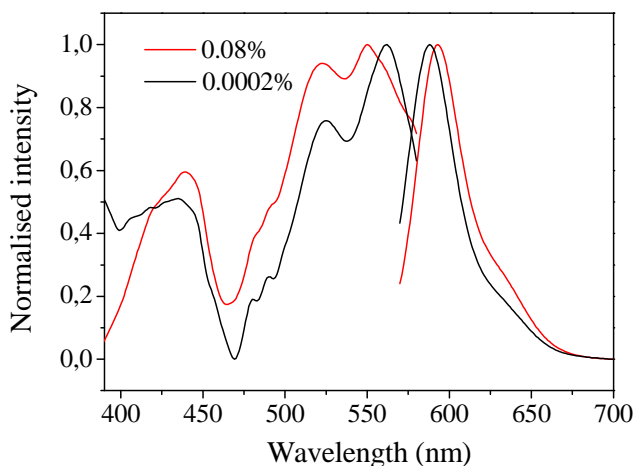
## Results



**Figure 4.28: Excitation (a) and emission (b) spectra of PS waveguides with 0.0002, 0.001, 0.005, 0.01 and 0.05 wt. % of LR305 in a polysiloxane matrix. Excitation and emission wavelengths were 520 nm and 620 nm, respectively.**

A deeper understanding of the effects of concentration on the fluorescence features can be obtained comparing the shapes of the spectra in figure 4.29, where the excitation and emission spectra are shown of PS sheets doped with low and high concentrations of

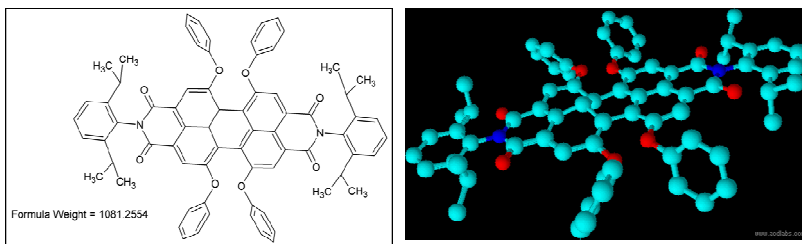
LR305, normalized by the maximum peak intensity value. As can be observed, in samples with lower dye concentrations the excitation and emission peaks are located at about 560 nm and 590 nm, respectively. By increasing the amount of LR305 by three orders of magnitude, these peaks shift to about 555 and 594 nm. It is worth noting that the datasheet provided by BASF locates the absorption and emission maxima in ethanol respectively at 578 and 613 nm. On the other hand, in PC the peaks were located at 573 and 597 nm [DEBI 07].



**Figure 4.29: Normalized excitation and emission spectra of PS sheets with 0.0002 wt. % (black line) and 0.08 wt. % (red line) of LR305. Excitation and emission wavelengths were 560 and 590 nm, respectively.**

The discrepancy between spectra measured in different environments is related to the chemical structure of LR305,

reported in [COLB 10] and depicted in figure 4.30. The perylenediimide molecule presents several hydrogen bonding acceptor functional groups (carbonyl oxygen, ether bridges, imide nitrogen). Thus, in ethanol the absorption/emission features are affected by specific interactions with the hydroxyl groups of the solvent, which can induce significant red shifts of the spectra with respect to the unperturbed molecule [LAKO 06]. These interactions cannot occur between the dye and the hydroxyl-free polysiloxane matrix used in this work. Comparing the case of PC, where strongly polar carbonyl groups are present along the macromolecule, and the almost non-polar, alkyl shielded Si-O-Si bonds in polysiloxanes, it can be envisaged that a blue-shift in both absorption and emission peaks in the case of a non-polar matrix is expected, as a result of less efficient solvent relaxation mechanism.



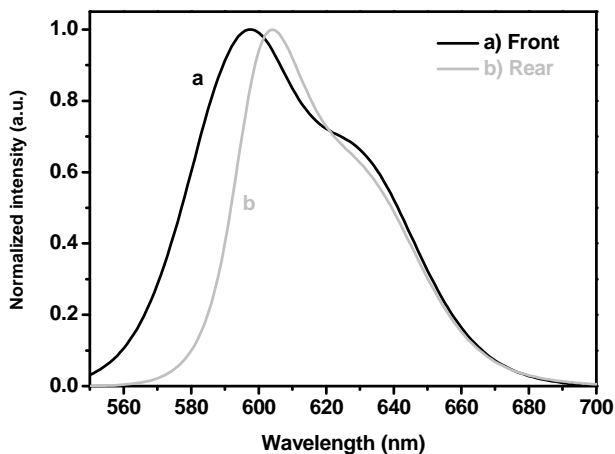
**Figure 4.30: Chemical structure of LR 305 in 2D and 3D view produced with Chemsketch (ACD Labs, free software).**

As for concentration effects, it must be taken into account that LR 305 was found to be resistant to aggregation-induced fluorescence quenching in the case of solid matrices up to concentrations of 100 mM [ALKA 06]. Keeping in mind that the maximum concentration of LR in PS reached in this work is about 30 mM (assuming the density of PS to be about  $1 \text{ g/cm}^3$ ), it is worth noting that the same

considerations about the absence of quenching and aggregation should apply also to the present case, where the appearance of the shoulder at 635 nm in highly concentrated samples, accompanied by a small blue-shift of the main excitation component and enhanced intensity of the secondary excitation peak at about 525 nm, were indeed observed in the case of high load of LR in PMMA matrices [COLB 10, FARA 92, WILS 10]. Nevertheless, the intrinsically different chemical nature of PMMA and PS as solid matrices should be considered. The strongly polar acrylate side groups in PMMA differ deeply from the almost apolar nature of the alkyl shielded siloxane macromolecule, thus concentration quenching effects in PS-derived samples cannot be ruled out.

Some samples were produced as films of polysiloxane with Lumogen red deposited on a non-doped polysiloxane slab. Films generally have a high concentration in order to convert the highest possible number of incoming photons, but this was prevented by the nature of the polysiloxane matrix, as a solubility limit was reached. Moreover, in about one month samples with a film of Lumogen red in polysiloxane over an empty silicone rubber tend to change; in fact the dye present in the polysiloxane diffuses through the empty silicone and the samples become red. In addition diffused LR has different optical properties. In figure 4.31 is reported the emission spectrum upon excitation at 530 nm of the same sample taken from (a) the front surface (the one with the deposited film) and (b) the rear surface, which is the one where the dye had been diffused. The emission is shifted by 10 nm (the maximum being located at 595 nm in the front surface case and 605 nm in the rear surface case).



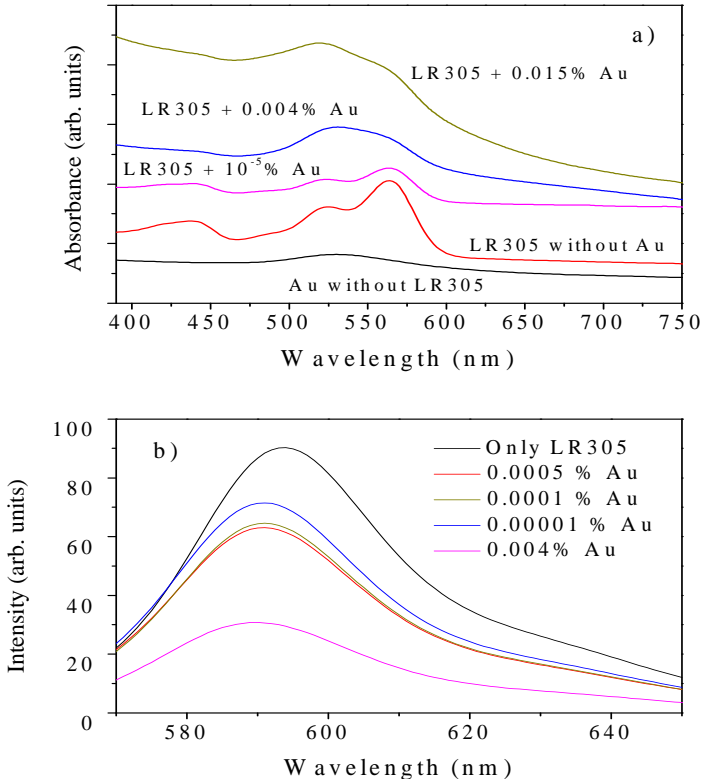


**Figure 4.31: Emission from the front and rear surface of a sample, exciting at 530 nm. See text for details.**

This indicates that LR does not interact with the lattice and is free to move into the polysiloxane, and this probably causes a different disposition of the molecule inside the lattice, probably creating some preferential orientation that modifies the spectra as shown in figure 4.31.

Gold nano-particles play the role of promoting the absorption peak at 530 nm and making the transmission of energy more efficient. Samples with embedded gold nano-particles present an enhancement of the absorption peak at 530 only for higher concentrations as shown in figure 4.32; for lower concentrations the difference is not appreciable, in fact the absorption bands of the two molecules, dyes and gold-nano-particles, overlap. Exciting on

the red band the emission is always less intense than in the sample without the Au-nc.



**Figure 4.32: (a) Absorption spectra of a PS film doped with gold alone and polysiloxane waveguides doped with 0.001% wt LR305 and with different concentrations of gold. (b) Emission spectra ( $\lambda_{\text{ex}}=540$  nm) of 0.001% wt LR305-doped samples with different gold concentrations.**

Gold nano-particles are believed to enhance the emission efficiency of the dye molecules, acting as nano-antennae. In this case, through the resonance energy transfer process, the dye absorption is

improved and, in turn, emission is improved. However, the realization of such a system is not trivial and requires a close proximity of the dye molecule to the gold cluster, to the extent that the boundary gold atoms can be seen as “grafted” to the organic molecule. This molecular architecture was previously successfully carried out through Au NC and Rhodamine molecule, exploiting the electrostatic attraction between the cationic form of the dye and the negative charge lying on the nanoparticles surface [IOSI 09]. In this work, which is to some extent a preliminary step on the path towards AuNC/dye complexes, the interaction between growing NC and dye is negligible, though carbonyl moieties on the diimide portion of LR305 were expected to establish coordination with gold atoms. Unfortunately, the lack of any appreciable benefit to emission intensity in bulk samples seems to indicate that this effect did not take place.

### *4.6 Choosing dye and matrix: summary*

We have presented the optical features of a few dye/matrix combinations. Only 3HF+parylene was tested on actual solar cells because of its high Stokes shift. The investigation of lower-shift BBOT was deferred to future work.

The option of building a multilayer device to enhance the shift was found to be not viable, as we did not find any stable dye combination that would produce the required optical features.

3HF was used with fluorinated polyimides. Lumogens in polyimide represent promising candidates for future studies, although we could not exploit them efficiently in the present case because of the

aforementioned optical features. Coumarines, instead, were just abandoned for their degradation into the PI matrix.

Finally, polysiloxane was investigated both as WLS in films and as LSC (only with a Pt catalyst) in bulk samples.

In the following part further measurements will be presented on the chosen sample types.

## Second part

---

### *4.7 Solar measurements*

The performance of a concentrator depends, as previously described, on the absorption and emission spectra of the dye and the efficiency range of the solar cell.

Results also differ, clearly, when the dye is used as WLS or LSC.

### *4.8 WLS*

Wavelength shifting experiments were performed only with 3HF dyes because of the very high Stokes shift of this molecule, as previously mentioned. Three solar cell types were covered with protective coatings doped with 3HF molecules: Si-photodiode, GaAs and InGaP.

Some remarks:

- The three polymers chosen for this application, because of the peculiar properties of each, were produced via different routes. It was therefore difficult to equip them with coatings having exactly the same properties. For example, a thickness of some hundred nanometers was achieved with parylene, which would have been very difficult to obtain via spin-coating techniques that instead produce micron-thick films.
- It was difficult to establish the amount of dye in parylene samples, as IR spectroscopy can hardly be exploited since the

3HF peaks are either too weak to be detected or superimposed on those of parylene.

- Polyimide cannot be produced in bulk samples because massive films are not sufficiently transparent.

#### 4.8.1 3HF embedded in parylene

Parylene films are very thin and have a high adhesion, so they are very difficult to remove after deposition. For this reason the cells were measured several times, before the deposition, under a solar simulator in order to estimate the experimental uncertainty and assess the repeatability of the measurements.

Many depositions were necessary since the average thickness deposited on the cell was only of some hundreds of nanometres.

The following remarks apply:

- The pure parylene coating on InGaP and GaAs solar cells lead to a foreseeable decrease in power output (see Chapter 2), in fact the yields of the GaAs and InGaP cells respectively decreased by 5.6% and 4.7%. This was simply due to the addition of a layer over the solar cell.
- Parylene displays some absorption in the UV range so some part of the solar spectrum did not actually reach the cell.
- The two cells (InGaP and GaAs) were covered with layers of co-evaporated parylene and 3HF. Three subsequent depositions were carried out and at every deposition a measurement of thickness and maximum power were performed. The maximum power was enhanced after the first deposition then levelled out, showing that the

beneficial effect of the dye was balanced by the negative effect of parylene.

- Seven successive depositions were performed on the silicon solar cell in order to obtain an appreciable result, with an enhancement of 2.2% from the performance of the bare cell (which, like most solar cells, is in fact not very efficient at 350 nm). The final thickness deposited on the cell corresponded to 1.93  $\mu\text{m}$ .

**Table 4.2: Results with parylene and 3HF on some solar cells.**

Sample	Power (mW)	% yield increase
Bare Si cell	$16.1 \pm 0.2$	--
Si pary C+ 3HF	$16.5 \pm 0.2$	2.2 %
GaAs	$5.53 \pm 0.01$	--
InGaP	$3.36 \pm 0.01$	--
GaAs+ Pary	$5.22 \pm 0.01$	<b>-5.6%</b>
InGaP+Pary	$3.20 \pm 0.01$	<b>-4.7%</b>
GaAs+ Pary +3HF	$5.31 \pm 0.01$	<b>1.7%</b>
InGaP+Pary +3HF	$3.24 \pm 0.01$	<b>1.3%</b>

#### 4.8.2 3HF embedded in fluorinated polyimide

Some very satisfactory results were obtained with polyimide. In order to preserve from damage the Silicon Photodiode, that had an epoxydic window that could be damaged by Dimethylformamide [wCIC 11] because of its capability to dissolve that kind of polymer, films were deposited on a thin glass which was stuck to the cell with a siliconic grease. The cell was measured bare, the influence of the glass and silicone grease was assessed and the enhancement was finally measured. Polyimide was deposited either spinning a very

thin film on the surface (1.4  $\mu\text{m}$ ) or pouring the dissolved polyimide over the glass and letting the solvent evaporate, achieving in this way a higher thickness (30  $\mu\text{m}$ ).

As the InGaP and GaAs solar cells did not have any external protective window and the gold contacts just extended outwards, the polyimide with 3HF was directly poured onto the surface of the cell. The coated cells were then dried in an oven and, when a complete film was formed of about 30  $\mu\text{m}$ , their performances were measured. The InGaP cell displayed an enhancement of 13%, while the GaAs displayed a decrease. This was probably due to a failure of the gold contacts, that could be affected by differential shrinkage, or a degradation of the cell due to the aggressiveness of the solvent. Results are reported in table 4.3 and 4.4.

**Table 4.3: Results with polyimide samples**

<b>Sample</b>	<b>Power (mW)</b>	<b>% yield increases</b>
<b>Si photodiode (SiPH)</b>	$7.9 \pm 0.1$	--
<b>SiPH + Pi +3HF spin</b>	$8.1 \pm 0.1$	2.5 %
<b>SiPH + Pi +3HF cast</b>	$8.2 \pm 0.1$	3.7 %
<b>InGaP</b>	$1.30 \pm 0.01$	--
<b>InGaP + 6 FDA DAD +3HF</b>	$1.47 \pm 0.01$	<b>13%</b>
<b>GaAs</b>	$2.71 \pm 0.01$	--
<b>GaAs + 6 FDA DAD + 3HF</b>	$2.66 \pm 0.01$	<b>-2%</b>

#### 4.8.3 3HF embedded in polysiloxane

Samples with polysiloxane were also produced and tested using the silicon photodiode. An optical matching was obtained by means of silicone oil. The enhancement was initially very high (5%), but after one month it decreased to 2.5%. This is due to interaction between



3HF and the platinum catalyst, as previously described; acetoxy polysiloxane suffers, on the other hand, from too low a viscosity, a high weight loss and shrinkage. Given the time and resources constraints of the present project, the decision was taken to defer this research line to possible future work.

**Table 4.4: Results with polysiloxane samples**

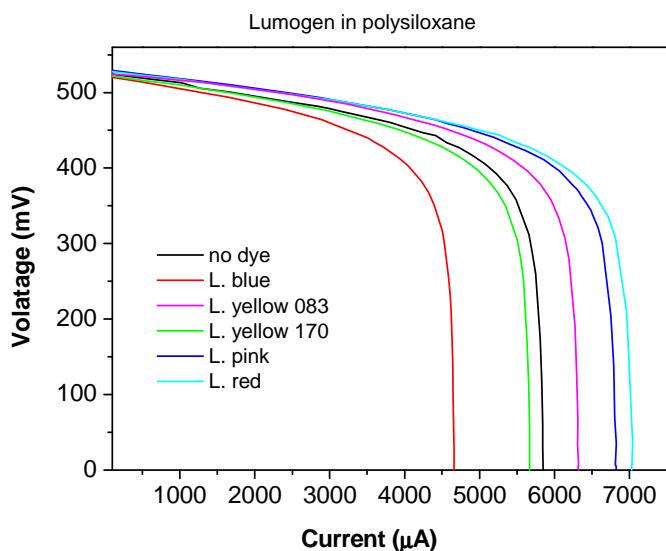
Sample	Power (mW)	% yield increases	Thickness
<b>Si photodiode (SiPH)</b>	$7.9 \pm 0.1$	--	
<b>SiPH + Polysiloxane + 3HF cast</b>	$8.3 \pm 0.1$	5 % (2.5% after 3 weeks)	60 $\mu\text{m}$
<b>SiPH + Polysiloxane + 3HF swelling</b>	$8.0 \pm 0.1$	1.3 %	1 mm

#### 4.9 LSC

All BASF Lumogens and 3HF were tested as LSC in order to evaluate their performance in a matrix.

3HF did not produce any appreciable result as a LSC because its absorption range is entirely contained in UV, where the total power of sun does not exceed 6%. Moreover, the emission at 530 nm is efficiently collected by the InGaP solar cell, but not by the other two cell types that were available to us. Finally, as previously mentioned, we had evidence that the only exploitable matrix (acetoxy polysiloxane) would be troubled by the non-negligible problems of weight loss and shrinkage. For all of the above reasons we decided not to pursue the use of 3HF as a LSC.

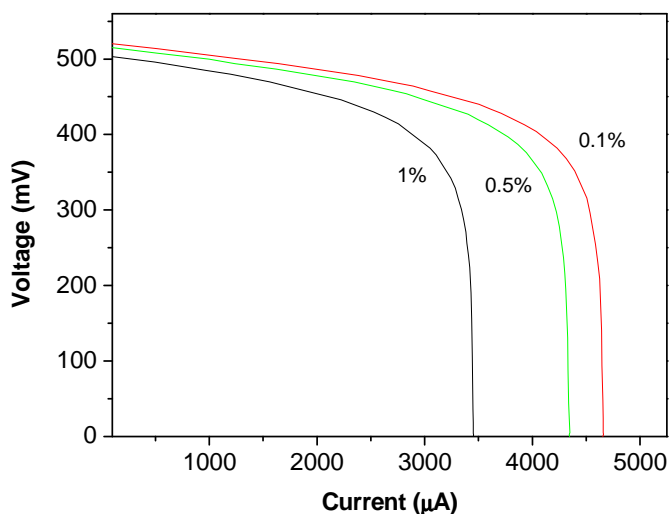
For the application as LSC the Lumogen series was studied and the most promising dye was individuated. Results are presented in figure 4.33; some dyes as Lumogen blue and yellow 170 have worse results than plain polysiloxane, while Lumogen red and pink perform fairly well (red and pink have, indeed, a wide absorption spectrum); the two mechanisms that route light to the cell are isotropic emission from the dye molecules and internal reflection.



**Figure 4.33: Performance comparison within the Lumogen series. Concentrations are 0.1%wt.**

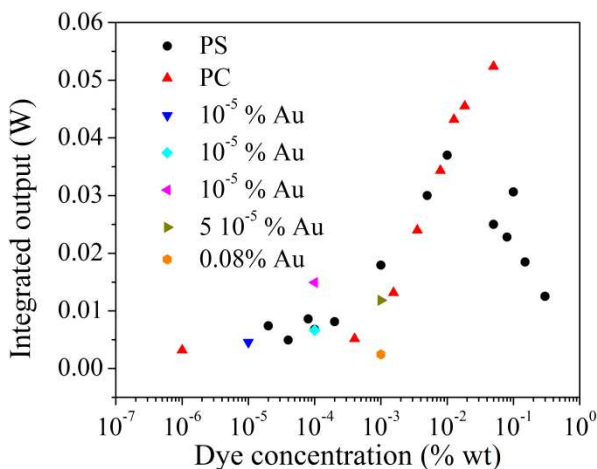
Dyes that have a small Stokes shift, such as Lumogen blue and yellow, caused a decrease in power output when tested with a silicon photodiode whose efficiency peaks at 1100 nm, because the balance between the efficiency of the dye and internal reflection was negative.

Comparing instead different concentrations of the same dye the negative influence of re-absorption is evident, as lower concentrations give better responses in power output (see figure 4.34).



**Figure 4.34: Current –tension curves from samples with three concentrations (1, 0.5 and 0.1% wt) of Lumogen blue.**

Having established that Lumogen red was the best option available to us for LSC purposes, we began the production and testing of larger samples in earnest.



**Fig. 4.35: Measurements of output power from the samples performed with an integrating sphere. A comparison between different types of polysiloxane is presented.**

Both bulk and thin-film samples were produced; all samples were measured with an integrating sphere and the edge output was evaluated integrating the emission between 400 and 800 nm. The efficiency of the samples was compared with that of a few PS samples doped with the same dye molecule [DEBI 08] - see figure 4.35. Polysiloxane displays a slightly better behaviour than PC samples at low dye concentrations (up to a value of 0.01% of LR); a decrease in output power is however observed past this point, whereas the power output of the PC rises until the concentration of 0.05% is reached. This suggests that the molecule behaves differently in different matrices, in agreement with the indication coming from the fluorescence spectra of LR in polysiloxane (as previously reported) and polycarbonate [MANS 05, SEYB 89, SLOO

06]. The emission decrease in PS-derived samples for high dye concentrations can be ascribed to a decrease in solubility of the dye within the matrix and to aggregation phenomena, giving rise to fluorescence quenching, through reabsorption or activation of non-radiative decay paths. As previously discussed, though no clear evidence of the formation of excimers or aggregates comes from the excitation and emission spectra of the samples, the different chemical environment experienced by LR molecules dispersed in a strongly polar environment (as in the case of PMMA or PC) or in an almost non polar medium (as in the case of polysiloxane) may influence the properties of the sample.

Studying the samples under a solar simulator with three different types of cells we obtained similar responses as those obtained with the integrating sphere. For all the three types of cell used (GaAs, InGaP and Si photodiode) the best observed performance corresponded to a 0.01% concentration of Lumogen Red, though for the GaAs solar cells the response of the sample with 0.005% LR was comparable.

From the results reported in Table I below it is possible to compare the power output produced by some significant samples.

**Table 4.5: Results obtained with selected samples and solar cells.**

<b>Sample</b>	<b>Power</b>		<b>Si</b>		<b>Power</b>		<b>GaAs</b>	
	<b>(mW)</b>				<b>(mW)</b>			
<b>Non filled PS</b>	0.75		0.33		2.42			
<b>0.001% LR PS</b>	1.19	59%	0.59	79%	2.80	16%		
<b>0.005% LR PS</b>	1.52	103%	0.62	88%	2.99	24%		
<b>0.01% LR PS</b>	1.67	123%	0.75	127%	2.85	18%		

A clear trend in sample performance can be derived from the results in Table I. The efficiency of the InGaP cells peaks around 500-600 nm. GaAs solar cells do not benefit much from LSC, as their efficiency curve is almost flat in the wavelength range where the dye collects and re-emits light (their efficiency peaks around 800 nm). The efficiency of the Si Photodiode is very poor in the range 400-590 nm, hence the collection of light at lower wavelength and re-emission at higher wavelength can make for a considerable improvement, as can be deduced from the EQE.

Furthermore the optical matching between the solar cells and LSCs was deeply different: the Si photodiode was used as it stood (this comprised the polymeric window in front of the cell surface), the GaAs solar cell was embedded in a thick layer of polysiloxane of the same type as that of the LSC, while a thin polyester film protected the InGaP cell from the sample and a dielectric thin strip prevented the Au contacts from falling into the slot. The presence of two thin films on the Si Ph and InGaP solar cells favours the transmission of light while the thick polysiloxane on GaAs seems to work as a dispersive media.

In fact sticking the LSC directly to a bare cell a decrease in power output was observed, while leaving a small space (less than a millimetre) between the cell and the LSC improved the performance of the device.

An intriguing observation was made when, because of the solidification of a bubble, a sample was left with a large (about 1 cm in diameter) depression in the middle of the light-facing surface. When the power output of this deformed sample was compared to that of 'normal' samples with the same dye concentration ( $10^{-4}$  % LR) it was noticed that the former actually performed better than the latter: the silicon photodiode respectively yielded 1.12 and 0.97 mW. The power output of the deformed sample was found to be higher than that exhibited by smooth, higher-concentration ( $10^{-3}$ % wt) samples even with the GaAS cell. This suggests that a perfectly flat light-facing surface may not be optimal for LSC purpose.

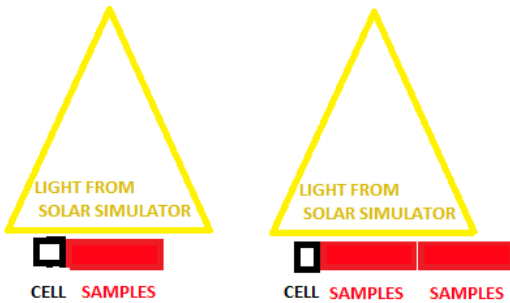
In Table 4.6 a comparison between samples of different length is reported. The maximum power is higher for shorter samples. For example, with the 5 cm sample with 0.001% LR the maximum power was 0.59 mW, while a 12 cm sample with the same dye concentration displayed a power output of only 0.49 mW; at the concentration of 0.01% LR, the maximum powers of the shorter and longer samples respectively were 0.74 and 0.68 mW.

**Table 4.6: Results with selected samples of different length, collected with the InGaP solar cell under a solar simulator.**

<b>Samples concentrations</b>	<b>InGaP Maximum power (mW)</b>
<b>empty</b>	0.34
<b>0.001% LR</b>	0.59
<b>0.001% LR long</b>	0.49
<b>0.01% LR</b>	0.74
<b>0.01% LR long</b>	0.68

Another intriguing observation was made comparing the performance of two adjacent shorter (5 cm) samples, only *one* of which fully lit, to the performance of a non-uniformly lit longer (12 cm) sample (see figure 4.36). In fact, not only the power output was higher with the former set-up than with the latter (see table 4.6), but the power output of the longer sample was smaller than the power output of *one* shorter sample. Note that the position of the cell relative to the light source remained constant so as to make results fully comparable.





**Figure 4.36: Schematic representation of the experimental set-up for comparing the performance of one shorter sample with that of two adjacent shorter samples or one longer sample. The solar simulator could not uniformly light the second shorter sample or the longer one.**

Interestingly, this result was reversed when the measurements were repeated in actual sunlight, the longer sample now performing better than one or two shorter samples. As a complete set of measurements obviously required some time, in order to obtain fully comparable results (characterized by common illumination conditions) only the short circuit current was measured. The open circuit voltage depends on many factors but mainly on the cell itself and its temperature. For this reason, all the measurements were carried out with the same cell and only the short circuit current (that under our experimental conditions was a fair representation of power) was collected. All the measurements were collected over as short a time as possible, and the empty cell was measured both at the beginning and the end of the session, to guarantee that lighting conditions had not changed.

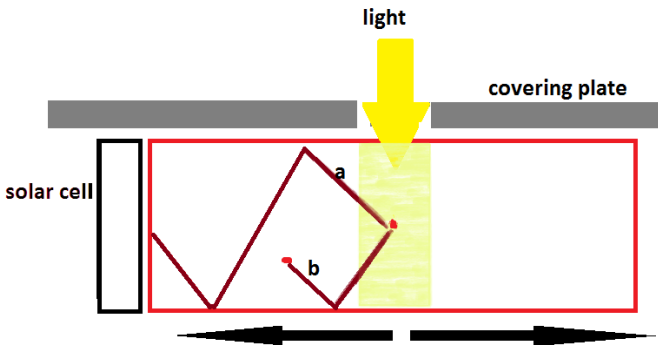
With all three cell types the longer samples outstripped the shorter ones. The best performance was achieved by a sample with a

concentration of 0.01% LR, in agreement with the results obtained with the integrating sphere.

**Table 4.7: Short circuit current measurements performed in open air.**

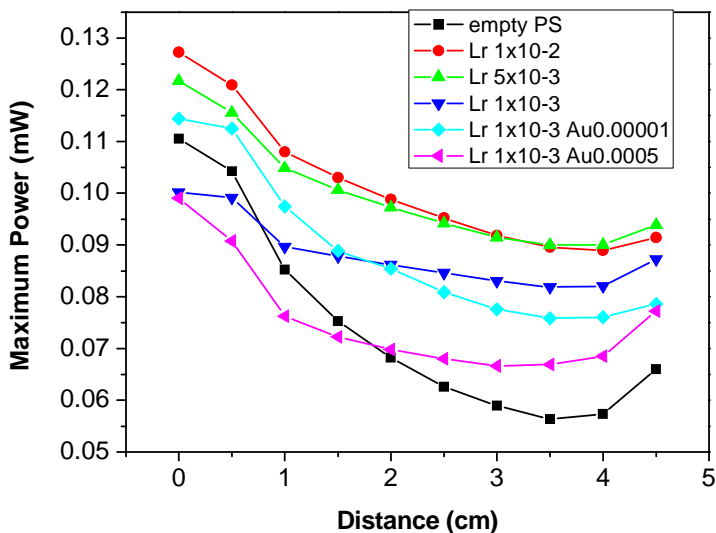
<b>Samples concentrations</b>	<b>InGaP <math>I_{sc}</math> (mA)</b>	<b>GaAs <math>I_{sc}</math> (mA)</b>	<b>Silicon <math>I_{sc}</math> (mA)</b>
<b>empty</b>	0.50	3.31	4.08
<b>0.001% LR</b>	0.89	3.95	6.42
<b>0.001% LR long</b>	1.27	4.50	8.28
<b>0.005% LR</b>	1.15	4.40	5.96
<b>0.005% LR long</b>	1.23	4.70	6.88
<b>0.01% LR</b>	1.22	4.51	6.05
<b>0.01% LR long</b>	1.80	5.37	9.18

In order to investigate the discrepancy between the results obtained with the solar simulator and those obtained with actual sunlight, the samples were re-tested (collecting, as always, the maximum power at the edge) illuminating only one 'slice' at a time, as shown in figure 4.37.



**Fig. 4.37: Only a slice is lit in the LSC device. A photon re-emitted by a dye molecule may be eventually absorbed by the cell (a) or by another dye molecule (b).**

The power corresponding to the first point in figure 4.38 is particularly high because of some amount of light coming directly from the solar simulator. The last two points, to which a higher power output corresponds than that displayed by the preceding points, are on the other hand affected by edge reflection effects [PETE 09, CHAT 03]. Neglecting the first and last points an exponential-like behaviour is apparent, in accordance with Batchelder's work [BATC 79].



**Fig. 4.38:** Maximum power of selected samples as a function of the distance between the illuminated portion of the sample and the Si cell surface. Distance  $x$  corresponds to the window  $[x, x+5 \text{ mm}]$ .

The results indicate that while the power collected when the non-doped polysiloxane sample is completely illuminated is equal to the sum of the powers collected illuminating the single slices (see figure 4.38), the sum of the single-slice powers is systematically less than the whole-sample power when a doped sample is considered. In fact, while the sum of the single-slice powers with the empty polysiloxane sample is 0.74 mW and the whole-sample power is 0.75mW, in the case of a 0.01% LR sample the sum of the single-slice powers is 1.01 mW and the whole-sample power is 1.68 mW; when the concentration of Lumogen red is 0.005% the figures are 0.99 and 1.53 mW, and when the concentration is 0.001% they are 0.88 and 1.19 mW.

Although a theoretical investigation of this phenomenon is outside the scope of the present project, re-absorption is the likely reason [SHOL 07, EARP 04, ROWA 08]. A high dye concentration, while beneficial in the portions of the sample that are thoroughly lit, may be altogether detrimental in portions that are not. Concentrators may thus be envisaged with gradients in dye content so as to accommodate fixed gradients in illumination due to the proximity of shadowing or reflecting elements.

### 4.10 Production procedure of nanophosphors

We here present some preliminary results from an investigation of nano-phosphors, namely the production and testing of  $\text{NaGdF}_4$  and a mixture of  $\text{NaGd}(95\%)\text{Eu}(5\%)\text{F}_4$ .

#### 4.10.1 Preparation

Our study follows in the footsteps of a work by Wang [FWAN 10].

Rare earth (RE) oxides with a purity  $\geq 99.99\%$  were used and transformed in  $\text{RECl}_3$  mixing the oxide powder with abundant HCl; water and excess HCl were left to evaporate, then the powder was soaked with de-ionized water and again left to dry.

A mixture of 12 ml of oleic acid, 28 ml of 1-octadecene and 0.2 M of  $\text{RECl}_3$  dissolved in methanol was then prepared. This transparent solution was heated for 30 min at  $160^\circ\text{C}$  while injecting  $\text{N}_2$  into it; the solution (which acquired a wheat-yellow color) was cooled down.

A solution of 20 ml of methanol, plus 1.6 mmol  $\text{NH}_4\text{F}$  (0.236 g) and 1 mmol NaOH (0.1586 g) was added and stirred for 30 minutes. The

solution was heated and degassed from 60°C to 110°C with an argon flux. The mixture was heated until 300°C for 1.5 hours

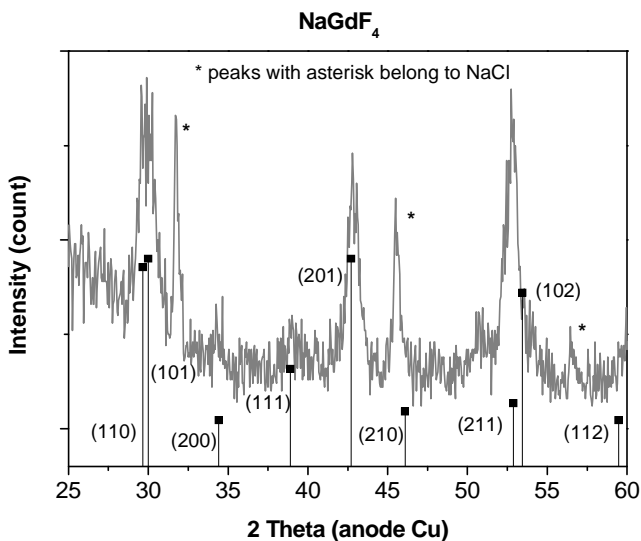
The solution was recovered with ethanol and acetone once cold and centrifugal purification was performed at 3000 rpm for 10 minutes.

After the purification particles were dissolved in cyclohexane and used in matrices. It is possible to produce different rare-earth combinations, as explained in chapter 3.

#### *4.10.2 The coupling of Gd and Eu*

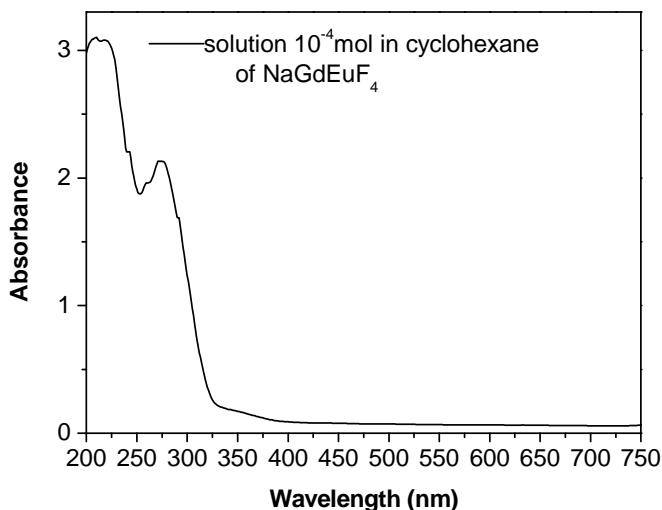
Zhang and Huang [ZHAN 10] presented a review on quantum cutting phosphors and established the interaction between various types of phosphors like Gd and Eu. Through the previously described procedure nano-particles of NaGdF<sub>4</sub> and NaGdEuF<sub>4</sub> were produced.

The structure obtained is the desired hexagonal one as demonstrated by the XRD spectrum reported in Fig.4.39, where the structure of the produced hexagonal NaGdF<sub>4</sub> is compared with literature (PDF#00-027-0699). Some other peaks are visible and marked with an asterisk, indicating the presence of some leftover sodium.



**Figure 4.39: XRD spectrum of NaGdF<sub>4</sub> hexagonal structure, the PDF#00-027-0699, asterisk peaks are those of NaCl**

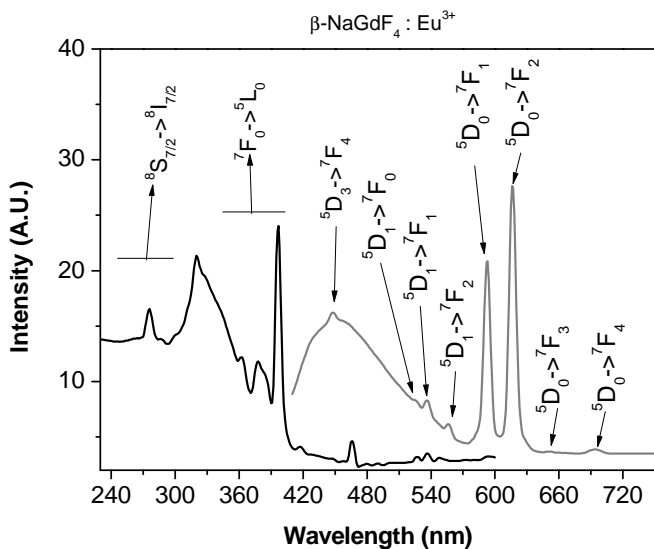
In figure 4.40 is reported the absorption spectrum of a solution of NaGdEuF<sub>4</sub> nano-particles in cyclohexane. The shoulder at about 270 nm corresponds to the absorption of the Gd<sup>3+</sup> ions, due to the abundant presence of Gd (95% - Eu is 5%).



**Figure 4.40:** Absorption spectrum of a solution of  $\text{NaGdEuF}_4$  in cyclohexane.

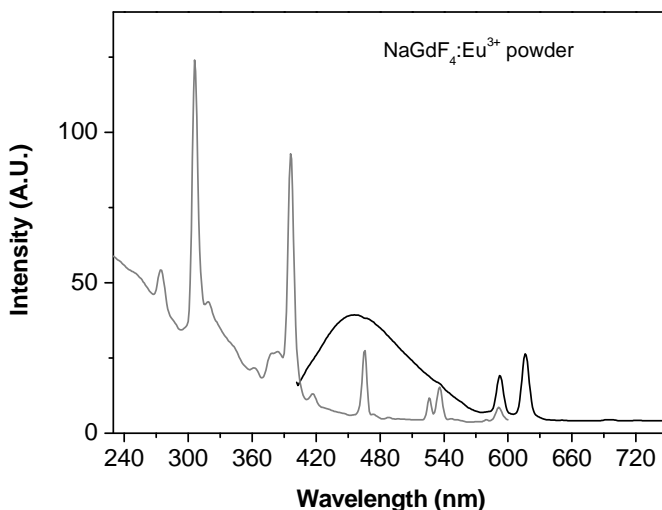
Typical Eu transition peaks are present in the emission and excitation spectra of the same solution. It is possible to note the transitions  ${}^5\text{D}_0 \rightarrow {}^7\text{F}_1$  at 590 nm,  ${}^5\text{D}_0 \rightarrow {}^7\text{F}_2$  at 614 nm,  ${}^5\text{D}_0 \rightarrow {}^7\text{F}_3$  at 652 nm  ${}^5\text{D}_0 \rightarrow {}^7\text{F}_4$  at 689 nm [PTAC 07]; a few other weak peaks are present and identified in the picture according to the works by Ptacek [PTAC 07] and Liu [YLIU 10].





**Figure 4.41: Excitation spectrum at  $\lambda_{em}=593$  nm and emission spectrum at  $\lambda_{ex}=397$  nm of a solution of  $\text{NaGdEuF}_4$  in cyclohexane .**

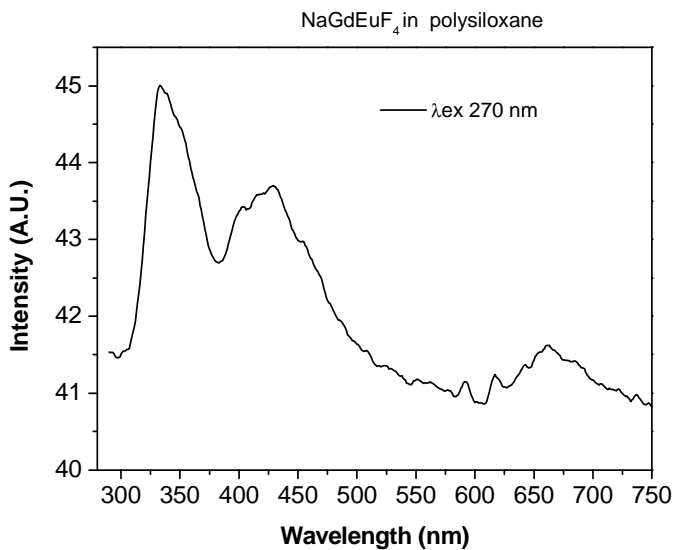
Typical, well defined Eu peaks can be noticed in the excitation spectra. In both the spectra of solid nanoparticles and nanoparticles in cyclohexane a broad band between 400 and 500 nm due to octadecene protecting the nanoparticle [wINV 12,FYAN 06] can be observed.



**Figure 4.42.:Spectrum of solid-particle NaGdEuF<sub>4</sub> in cyclohexane, exciting at 390 nm and emitting at 615 nm.**

These spectra are comparable to those obtained by Liu [YLIU 10].

If the Eu complex is inserted in polysiloxane the result presented in figure 4.43 is obtained: the location of peaks is compatible to that reported by Xu [XUHU 04], who created a complex of Eu<sup>3+</sup> directly with syloxane. The emission intensity that we obtained was actually rather low if compared to Xu's, but the concentration of the powder inside the sample in our preliminary study was only 0.1%, while Xu worked with a concentration of 2% wt.



**Figure 4.43: Emission spectrum of 0.1 % wt of NaGdEuF<sub>4</sub> in polysiloxane.**

## Bibliography

- [ALKA 06]  
Al-Kaysi, R. O.; Ahn, T. S.; Muller, A. M.; Bardeen, C. J. The photophysical properties of chromophores at high (100 mM and above) concentrations in polymers and as neat solids. *Phys. Chem. Chem. Phys.*, 8 (2006) 3453–3459
- [BATC 79]  
J.S.Batchelder ,A.H.Zewail, T.Cole; Luminescent solar concentrators. 1: Theory of operation and techniques for performance evaluation, *Appl. Opt.*18 ,no 18 (1979),3090-3110.
- [BERL 71]  
I. B. Berlman, *Handbook of Fluorescence Spectra of Aromatic Molecules*, Academic Press,( 1971), 402.
- [CART 09]  
S. Carturan, M. Tonezzer, A. Quaranta, G. Maggioni, M. Buffa, R. Milan, Optical properties of free-base tetraphenylporphyrin embedded in fluorinated polyimides and their ethanol and water vapours sensing capabilities,*Sens. Actuators B*, 137, (2009) 281.
- [CHAL 65]  
A.J. Chalk, J.F. Harrod, *Homogeneous Catalysis. II. The Mechanism of the Hydrosilation of Olefins Catalyzed by Group VIII Metal Complexes*, *J. Am. Chem. Soc.* 87 (1965) 16-21.
- [CHAT 03]  
A. J. Chatten, K. W. J. Barnham, B. F. Buxton and N. J. Ekins-Daukes, *A new approach to modelling quantum dot*

*concentrators*, Solar Energy Materials and Solar Cells, 75 (2003) 363-371.

- [CHOU 93]  
Pi-Tai Chou, Marty L. Martinez, Photooxygenation of 3-hydroxyflavone and molecular design of the radiation-hard scintillator based on the excited-state proton transfer, *Radiat. Phys. Chem.*, 41 (1993) 373-378
- [COLB 10]  
K. A. Colby, J. J. Burdett, F. F. Frisbee, L. Zhu, R. J. Dillon, C. J. Bardeen, Electronic energy migration on different time scales: concentration dependence of the time-resolved anisotropy and fluorescence quenching of Lumogen Red in Poly(methyl) methacrylate, *J. Phys. Chem. A*, 114 (2010). 3471-3482
- [COLB 10]  
K. A. Colby, J. J. Burdett, R. F. Frisbee, L. Zhu, R. J. Dillon and C. J. Bardeen, Anisotropy and fluorescence quenching of Lumogen Red in poly(methyl methacrylate), *J. Phys. Chem. A* 114 (2010) 3471–3482.
- [DEBI 07].  
M. G. Debije, D. J. Broer, C. W. M. Bastiaansen, Effect of dye alignment on the output of a luminescent solar concentrator *Proc. 22nd European Photovoltaic Solar Energy Conf., Munich, Germany, 2007*, Eds. G. Willelke, H. Ossenbrink, P.Helm,(2007) 87-89
- [DEBI 08]  
Michael G. Debije, Paul P. C. Verbunt, Brenda C. Rowan, Bryce S. Richards, and Theo L. Hoeks; Measured surface loss from luminescent solar concentrator waveguides, *Applied Optics*, 47, (2008) 6763-6768

- [EARP 04]  
A. A. Earp *et al.*, "Optimisation of a three-colour luminescent solar concentrator daylighting system," *Sol. Energy Mater. Sol. Cells*, 84 (2004) 411–426
- [FARA 92]  
V. L. Fara, R. Grigorescu, and C. Dimofte, "Optimum efficiency of fluorescent solar concentrators," in *Optical Materials Technology for Energy Efficiency and Solar Energy Conversion XI: Selective Materials, Concentrators and Reflectors, Transparent Insulation and Superwindows*. Toulouse-Labege, France: SPIE, (1992). 306–312.
- [FWAN 10]  
Feng Wang<sup>1</sup>, Yu Han<sup>2</sup>, Chin Seong Lim<sup>3</sup>, Yunhao Lu<sup>4</sup>, Juan Wang<sup>1</sup>, Jun Xu<sup>5</sup>, Hongyu Chen<sup>5</sup>, Chun Zhang<sup>1,4</sup>, Minghui Hong<sup>3,6</sup> & Xiaogang Liu<sup>1</sup>, Simultaneous phase and size control of upconversion nanocrystals through lanthanide doping, *Nature*, 463 (2010) 1061-1065
- [FYAN 06]  
F. Yang J., M. Zhang, J. Chen, Y. Liang, Structural changes of  $\alpha$ -lactalbumin induced by low pH and oleic acid, *Biochimica and biophysica Acta* 1764 (2006) 1389-1396
- [HAYA 71]  
T. Hayashi, S. Kawai, T. Ohno, Fluorometric Study on the Metal Chelates of Flavone Derivatives. II. Correlation between Fluorescence Emission and the Carbonyl Stretching Frequency, *Chem. Farm. Bull.* 19 (1971) 792-795
- [IOSI 09]  
M. Iosin, P. Baldeck and S. Astilean, "Plasmon-enhanced fluorescence of dye molecules," *Nuclear Instruments and Methods in Physics Research B* 267 (2009) 403–405

- [KATY 77]  
M. Katyal, S. Prakash, Analytical reactions of hydroxyflavones, *Talanta* 24 (1977) 367-315.
- [KIND 07]  
R-Kinderman. L.H.Sloof, A.R.Burgers, N.J.Bakker, A. Buchtemann, R.Danz, J.A.M van Roosmalen, "I-V Performance and stability of dyes for luminescent plate concentrators", *J.Sol.En.Eng.*, 129 (2007) 277-283
- [KLAM 09]  
E. Klampaftis, D. Ross, K. R. McIntosh, B. S. Richards, Enhancing the performance of solar cells via luminescent down-shifting of the incident spectrum: A review, *Solar Energy Materials & Solar Cells* 93 (2009) 1182-1194
- [KUNT 98]  
V. Kuntic, S. Blagojevic, D. Malesiev, Z. Radovic, M. Bogavac, Spectrophotometric Investigation of the Pd(II)-Quercetin Complex in 50% Ethanolic Solution, *Monatsh. Chem.* 129 (1998) 41-48
- [LAKO 06]  
Al-Kaysi, R. O.; Ahn, T. S.; Muller, A. M.; Bardeen, C. J. The photophysical properties of chromophores at high (100 mM and above) concentrations in polymers and as neat solids. *Phys. Chem. Chem. Phys.*, 8 (2006) 3453–3459.
- [LOKE 62]  
J.H. Looker, W.W. Hanneman, Physical and Chemical Properties of Hydroxyflavones. II. 3-Aroyl-5-hydroxyflavones. *Synthetic and Infrared Spectral Studies*, *J. Org. Chem.* 27 (1962) 3261-3263
- [MAGG 09]  
G. Maggioni, M. Tonezzer, S. Carturan, A. Quaranta, M.

Buffa, A. Antonaci, G. Della Mea; Novel Wavelength-Shifting Materials for Improving Solar Cells Efficiency; 24th European Photovoltaic Solar Energy Conference, 21-25 September 2009, Hamburg, Germany; 621 – 623; doi: 10.4229/24thEUPVSEC2009-1DV.4.28

- [MANS 05] ,  
A. F. Mansour et al., “Laser dyes doped with poly(ST-Co-MMA) as fluorescent solar collectors and their field performance,” *Polym. Test.*, 24, (2005) 519–525
- [MWAN 07]  
M. Wang, T. Teslova, F. Xu, T. Spataru, J.R. Lombardi, R.L. Birke, Raman and Surface Raman Scattering of 3-Hydroxyflavone, *J. Phys. Chem. C* 111 (2007) 3038-3043
- [PETE 09] ,  
M. Peters, J. C. Goldschmidt, P. Löper, B. Bläsi and A. Gombert, *The effect of photonic structures on the light guiding efficiency of fluorescent concentrators*, *Journal of Applied Physics*, 105 (2009) 0149010-0149013
- [PETR 02]  
J.M. Petroski, C. De Sa Valente, E.P. Kelson, S. Collins, FTIR Spectroscopy of Flavonols in Argon and Methanol/Argon Matrixes at 10 K. Reexamination of the Carbonyl Stretch Frequency of 3-Hydroxyflavone, *J. Phys. Chem. A*, 106 (2002) 11714-11718.
- [PROT 08]  
S. Protti, A. Mezzetti, C. Lapouge, J.P. Cornard, Photochemistry of metal complexes of 3-hydroxyflavone: towards a better understanding of the influence of solar light on the metal-soil organic matter interactions, *Photochem. Photobiol. Sci.* 7 (2008) 109-119.



- [PTAC 07]  
P.Ptacek, H. Schafer, K. Kompe, M. Haase, Crystal phase control of luminescing  $\text{NaGdF}_4:\text{Eu}^{3+}$  nanocrystals, *Adv. Funct. Mater.* 17 (2007) 3843-3848
- [ROWA 08]  
B.C. Rowan, R. Wilson, B.S. Richards, *Advanced Material Concepts for Luminescent Solar Concentrators*, *IEEEjournal of selected topics in quantum electronics* , 14 (2008) 1312-1321.
- [SEYB 89]  
G.Seybold, and G.Wagenblast, "New Perylene and Violanthrone Dyes for Fluorescent Collectors", *Dyes and Pigments*, 11 (1989) 303-317.
- [SHOL 07]  
V. Sholin, J. D. Olson, and S. A. Carter, "Semiconducting polymers and quantum dots in luminescent solar concentrators for solar energy harvesting," *J. Appl. Phys.*, 101, (2007). 123114-1–123114-9
- [SLOO 06]  
L. H. Slooff, R. Kinderman, A. R. Burgers, A. Büchtemann, R. Danz, T. B. Meyer, A. J. Chatten, D. Farrell, K. W. J. Barnham, and J. A. M. Van Roosmalen, "The luminescent concentrator illuminated," *Proc. SPIE* 6197 (2006) 1-8
- [SLOO 07]  
L.H.Sloof, R-Kinderman, A.R.Burgers, N.J.Bakker, J.A.M van Roosmalen, A. Büchtemann, R.Danz, M Schleusener," efficiency enhancement of solar cells by application of a polymer coating containing a luminescent dye", *J.Sol.En.Eng.* , 129 (2007) 272-276

- [TANA 06]  
N.Tanaka, N. Barashkov, J.Heath, W.N.Sisk, “photodegradation of polymeric dispersed perylene di-imide dyes”; *App.Optics*; 45 (2006) 3846-3851
- [TEOH 97]  
S.G. Teoh, S.H. Ang, J.P. Declercq, Synthesis and characterization of di-n-butylbis(2,4-dihydroxybenzoato)tin(IV), *Polyhedron* 16 (1997) 3729-3733
- [TOMM 04]  
S. Tommasini, M.L. Calabrò, P. Donato, D. Raneri, G. Guglielmo, P. Ficarra, R. Ficarra, Comparative photodegradation studies on 3-hydroxyflavone: influence of different media, pH and light sources, *Journal of Pharmaceutical and Biomedical Analysis*, 35 (2004) 389–397
- [VAVR 08]  
A. Vavra, R. Linder, K. Kleinermanns, Gas phase infrared spectra of flavone and its derivatives, *Chem. Phys. Lett.* 463 (2008) 349-352
- [wBAS 12]  
[<http://www2.basf.us/additives/pdfs/p3201e.pdf> 30-01-2012, retrieved last 30/01/12
- [wCIC 11]  
<http://www.who.int/ipcs/publications/cicad/en/cicad31.pdf>
- [WENG 92]  
J.H. Wengrovius, M.F. Garbauskas, Solution and solid-state structures of several dialkyl tin dicarboxylate complexes [R<sub>2</sub>Sn(O<sub>2</sub>CRR'CO<sub>2</sub>)<sub>2</sub>]: Polymorphic organotin polymers, *Organometallics* 11 (1992) 1334-1342.
- [WILS 10]  
L. R. Wilson, Luminescent solar concentrators: a study of

optical properties, re-absorption and device optimization,  
PhD Thesis.Edinburgh 2010

- [wINV 12]  
<http://www.invitrogen.com/site/us/en/home/References/Molecular-Probes-The-Handbook/Probes-for-Lipids-and-Membranes/Fatty-Acid-Analogs-and-Phospholipids.html#head1> retrieved last 10/01/12
- [WWAN 07]  
Wang, Z. He, H. Mao, Y. Du, Y. Wang, Optical properties of BBOT-doped silica films prepared via sol-gel processing, *Journal of Luminescence*, 122–123 (2007) 268-271
- [XUHU 04]  
J. Xu, X.H. Huang, N.L. Zhou, J.S. Zhang, J.Ch. Bao, T.H. Lu, C. Li, Synthesis, XPS and fluorescence properties of  $\text{Eu}^{3+}$  complex with polydimethylsiloxane, *Materials Letters*, 58 (2004) 1938–1942
- [YLIU 10]  
Yongsheng Liu, Datao Tu, Haomiao Zhu, Renfu Li, Wenqin Luo, Xueyuan Chen, A Strategy to Achieve Efficient Dual-Mode Luminescence of  $\text{Eu}^{3+}$  in Lanthanides Doped Multifunctional  $\text{NaGdF}_4$  Nanocrystals ,*Adv. Mater.*, 22 (2010) 3266-3271
- [YOKO 80]  
T. Yokoyama, H. Suzuki, J. Mukai, The Effects of Heat Treatment on Dissipation Factors of Silicone Rubber, *IEEE Trans. Electr. Ins.* EI-15 (1980) 373-381
- [ZHAN 10]  
Q.Y.Zhang and X.Y.Huang, Recent progress in quantum cutting phosphors, *Progress in Materials Science*, 55 (2010) 353-427



# CHAPTER 5

## Conclusions and Further Work

---

### *5.1 Conclusions*

The aim of this thesis is the production and characterisation of materials for the enhancement of solar cells. The crucial issue is to increase the efficiency of the cell while keeping cost low. The materials investigated in this project fulfil this requirement.

Polymers are very attractive for their low cost, low weight and versatility, while organic dyes are of low cost and easy usage. This drove our choice of an organic matrix-organic dye combination.

The matrices on which we focused are polysiloxanes, fluorinated polyimides and parylene:

- Polysiloxanes were exploited for their transparency, radiation hardness and low cost.
- Fluorinated polyimides were selected for their transparency, low thermal expansion and chemical resistance.
- Parylene was tested for its impressive adhesion properties, low permeability, high transparency and temperature resistance.

Luminescent species were individuated in organic dyes that have a wider absorption range than rare-earth ion complexes and are not as toxic as quantum dots.

Matrices and dyes were then combined to achieve the desired enhancement. This beneficial effect can be accomplished in different ways. The two methods explored in this thesis are wavelength shifting (WLS) and luminescent solar concentration (LSC).

### 5.1.1 WLS

As WLS materials, all the aforementioned matrices were studied in order to obtain a thin film that, properly doped with a dye, could achieve a high Stokes shift, shifting a significant part of the incoming solar spectrum into the wavelength interval where the efficiency of the solar cell is highest. This film could be applied over the materials encapsulating the cell or as encapsulation material itself.

The organic molecule that accomplished the best results is the one characterized by highest Stokes shift, namely 3HF; all the combinations of this dye with the three matrices produce an increment in the maximum power output of the silicon and InGaP solar cells. (The results obtained with the GaAs solar cell, which has a markedly different efficiency curve to the other two cell types, were on the other hand not as satisfactory).

It is well known that the presence of an additional layer such as the encapsulation coating can negatively affect the performance of the cell, but the usage of a wavelength shifter in the encapsulation material, or deposited on the cell, can lead to a performance increase.

The usage of multiple dyes to obtain a higher Stokes shift is not a straightforward option. In fact, extreme care must be paid to the overlap between the emission and absorption spectra of the dyes and cell, in order to minimize re-absorption effects.

### *5.1.2 LSC*

LSC connects two main aspects: the exploitation of direct and diffused solar light impinging on a large surface, via the concentration of light onto a small cell positioned on a panel side, and the architectural demand for multi-colour surfaces.

Among the materials investigated in this project, only polysiloxanes appear to be suitable for this application, because of their cost effectiveness and the capability to produce large samples. Furthermore this matrix is environmentally friendly and can be shaped in numerous flexible forms. Lumogen red in polysiloxane displays interesting properties which are comparable to those of polycarbonate, even if the solubility limit is markedly lower for polysiloxane than polycarbonate.

Samples produced with commercial polysiloxane are known to suffer from leaching, but this is due to some additives that are present in the commercial formulation; this problem is not observed in samples produced starting from pure copolymers. So this problem can be easily overtaken, devising an ad hoc formulation for the purpose.

A second problem is the interaction of the polysiloxane catalyst with the dye molecule. Platinum is one of the most common catalysts, but unfortunately it forms some complex with the dye, causing disruption in the fluorescence. This could be avoided using a

different catalyst (tin, for example, does not display any interaction with Lumogen red – although it too forms a complex with 3HF) or the acetoxy formulation of polysiloxane, that does not need any catalyst at all.

### 5.1.3 Further work

This thesis provides some cues for further chemical and physical investigations:

- Experiments on the durability of dyes in matrices should be performed.
- Encapsulation properties of different matrices should be tested and evaluated.
- Other types of cells, like for example organic-dye sensitised solar cells, could be tested and coupled to particular matrix/dye combinations.

Some theoretical questions are also worth consideration.

In chapter 4 some samples with a low dye concentration ( $10^{-4}$  % wt) and a large depression in the middle (~1 cm in diameter) offer results similar in maximum power output to samples with a concentration of  $10^{-3}$  % wt. This hints at the possibility that a perfectly flat light-facing surface may not be optimal with respect to the performance of the device. Various patterns of orderly unevenness in the light-facing surface may be investigated through Monte Carlo simulations akin to those in [SAHI 11] to establish whether this instance of symmetry breaking may lead to beneficial effects.



A second open question is the optimal size and dye concentration of the LSC device. In fact, in order for the device to be effective the dye concentration must be sufficiently high, but with a higher concentration the luminescence is more likely to be reabsorbed; also, as the area of the light-facing surface of the LSC increases, more light enters the medium, but with a greater chance of being lost due to escape. Monte Carlo simulations, again, may prove extremely beneficial in this respect.

*Bibliography*

- [SAHI 11]  
D. Sahin, B. Ilan, D.F. Kelley, Monte-Carlo simulations of light propagation in luminescent solar concentrators based on semiconductor nanoparticles, *Journal of Applied Physics* 110, (2011) 033108-033116

# Appendix A

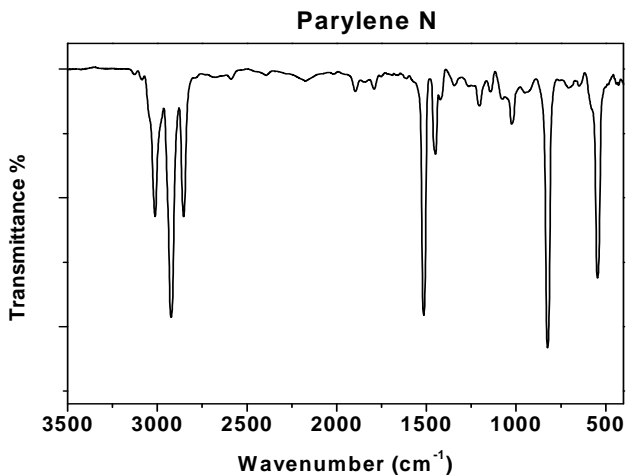
## INFRARED ANALYSIS

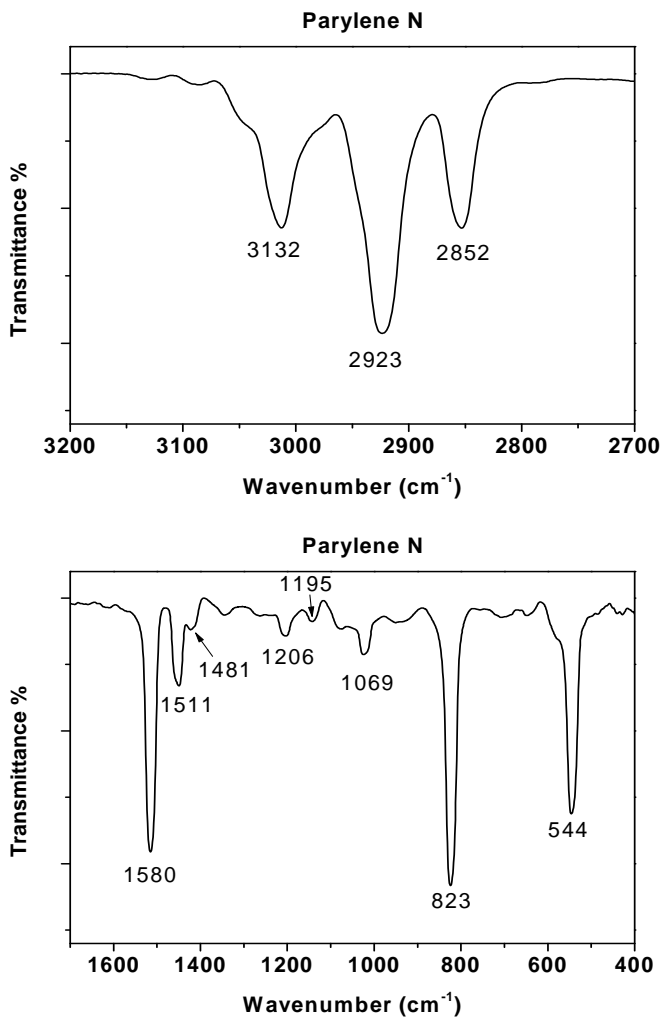
---

The infrared analysis of the most relevant matrices and dyes (polysiloxane, parylene and 3HF) is here presented.

### *Parylene N*

Parylene N is formed by two units  $\text{CH}_2$  and a benzenic ring, bonded along the chain in position 1 and 4. In figure A.1 the spectra of parylene C are reported; the picture consists in a complete spectrum and two enlargements with labelled peaks.





**Figure A.1:** IR spectra of parylene C on Si Bayville. The whole spectrum and two enlargements are shown.

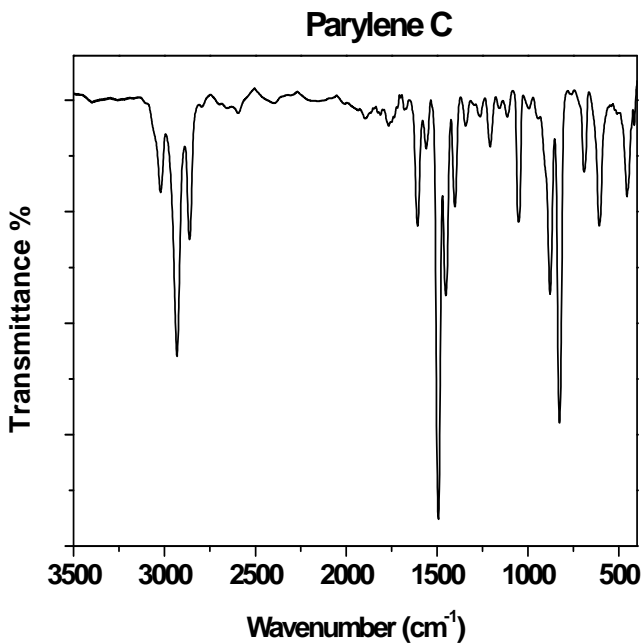
In Table A.1 peak assignments are proposed using the program “Know it all” [wKNO 12] and literature data.

**Table A.1: IR peak assignments in parylene N.**

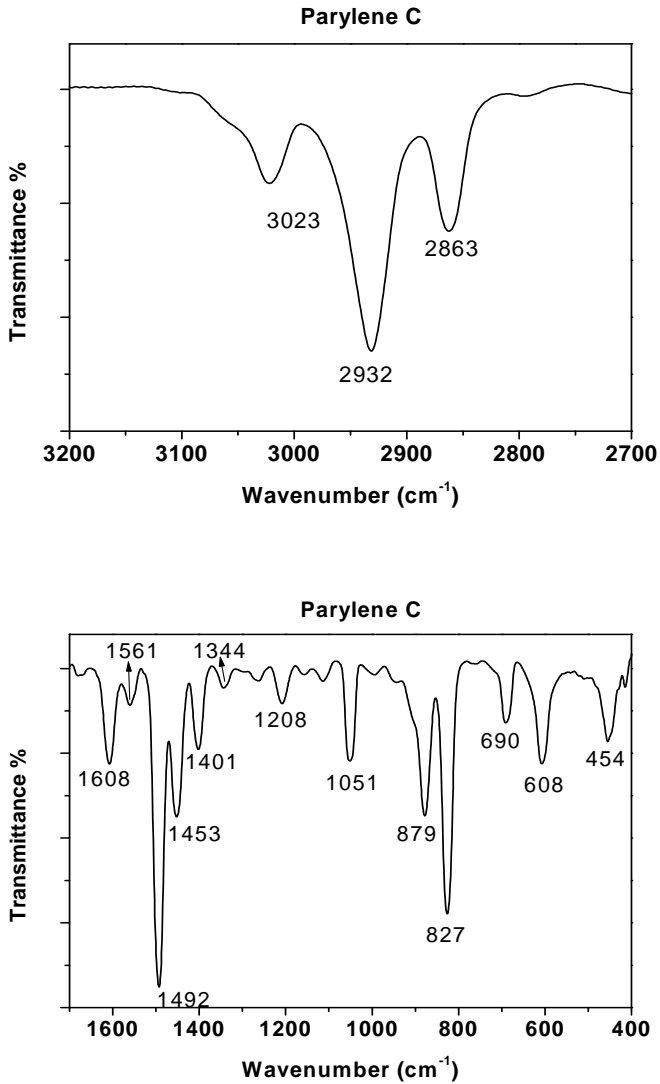
<b>Bond</b>	<b>Wavenumber cm<sup>-1</sup></b>	<b>Strength</b>	<b>Type</b>	<b>Comment</b>
<b>Aromatic CH</b>	3123	w	stretching	symmetric
<b>CH<sub>2</sub></b>	2923		stretching	Asymmetric
<b>CH<sub>2</sub></b>	2852		stretching	symmetric
<b>Benzenic ring</b>	1511	V	stretching	
	1580	M	stretching	
	1449	M	stretching	
<b>CH of benzenic ring</b>	1206	w	bend	In plane H bend
	1139	w	bend	In plane H bend
	1069	w	bend	In plane H bend
	1021	w	bend	In plane H bend
	823	s	deflection	2 hydrogen out of plane
	544	m		
<b>-CH<sub>2</sub> -</b>	1481	m	deflection	

### *Parylene C*

Parylene C is formed by two units  $\text{CH}_2$  and a benzenic ring bonded along the chain in position 1 and 4 and a Chlorine atom in position 3. In Figure A.2 the complete IR spectrum and two enlargements are reported.



*Infrared Spectra*



**Figure A.2:** IR spectra of parylene C on Si Bayville; the whole spectrum and two enlargements are shown.

Appendix A

Table A.2: IR peak assignments in parylene C.

Bond	Wavenumber cm <sup>-1</sup>	Strength	Type	Comment
<b>Aromatic CH</b>	3123	w	stretching	symmetric
<b>CH<sub>2</sub></b>	2932-2940		stretching	Asymmetric
<b>CH<sub>2</sub></b>	2863		stretching	symmetric
<b>Benzenic ring</b>	1617-1608	v	stretching	
	1579	M	stretching	
	1492	V	stretching	
	1453	M	stretching	
<b>CH of benzenic ring</b>	1208	w	bend	In plane H bend
	1160	w	bend	In plane H bend
	1040-1020	w	bend	In plane H bend
	945	w	deflection	1 hydrogen out of plane
	879	m	deflection	2 hydrogen out of plane
	827	s	deflection	2 hydrogen out of plane
	690	m	deflection	2 hydrogen out of plane
<b>CH<sub>2</sub></b>	1453	m	deflection	
<b>C-Cl</b>	608	s	stretching	



Polysiloxane

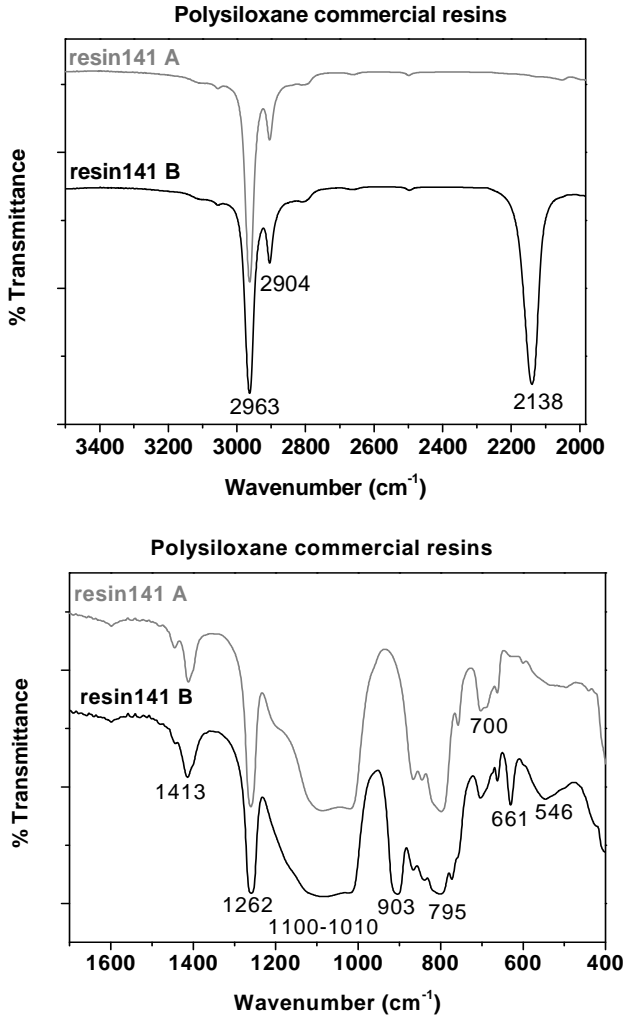


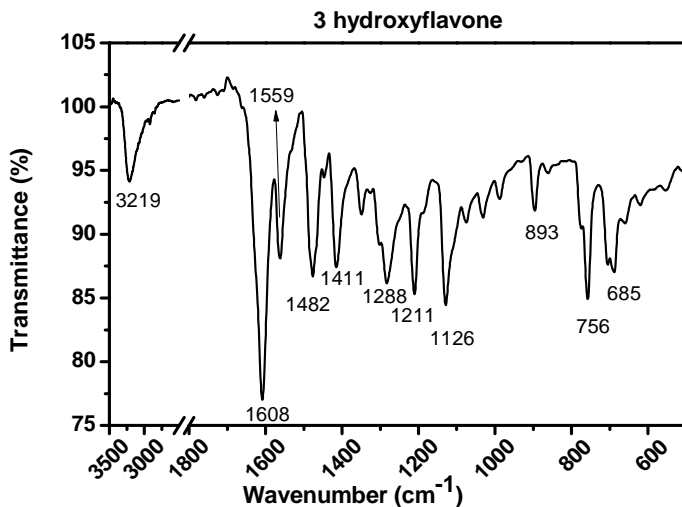
Figure A3: IR spectra of polysiloxane on Si Bayville; the whole spectrum and two enlargements are shown.

**Table A.3: IR peak assignments in commercial polysiloxane**

Bond	Wavenumber cm <sup>-1</sup>	Strength	Type	Comment
<b>Aromatic CH</b>	2963		Stratching	asymmetric
	2904		Stratching	symmetring
<b>Si-H</b>	2138		stratching	
	1413		deflection	asymmetric
	1262		deflection	symmetric
<b>Si-O-Si</b>	1100-1010		stratching	
<b>Si-O-C</b>	1100-1010		stratching	
<b>Si-O-C</b>	903		stratching	
<b>Si-H</b>	795		wagging	

### *3-Hydroxyflavone*

3HF , was widely used in this work; its interaction with matrices was also studied in detail. Its IR spectrum is shown in figure A.4 and in the following table some peak assignments are proposed.



**Figure A.4:** IR spectra of 3HF on Si Bayville. The whole spectrum and two enlargements are shown.

**Table A.4:** IR peak assignments in 3HF.

Wavenumber $\text{cm}^{-1}$	Bond type	Comment	References
3222	OH stretching	Broad	LOOK 61
3099	-CH stretching	Shoulder	LOOK 61
1641	Carbonilic band	Shoulder at 1627 $\text{cm}^{-1}$	LOOK 61
1628	Carbonilic band, shoulder		Know it All
1608	Aromatic Skeletal Vibrations	strong	KATR 59
1563	Aromatic Skeletal Vibrations	strong	KATR 59

Appendix A

1555	Aromatic Skeletal Vibrations	shoulder	KATR 59
1481	Aromatic Skeletal Vibrations	strong	KATR 59
1469	Aromatic Skeletal Vibrations	strong	KATR 59
1445	Aromatic Skeletal Vibrations	strong	KATR 59
1415	Aromatic Skeletal Vibrations	Strong OH in plane deformation	KATR 59
1350	Aromatic pyrone C-H out of plane deformation	Borderline strong- medium OH in plane bend vib	LOOK 61 VARV 08
1305	Aromatic pyrone C-H out of plane deformation	Strong OH in plane bend vib	LOOK 61
1287	Aromatic pyrone C-H out of plane deformation	The third stornger	LOOK 61
1212	Aromatic pyrone C-H out of plane deformatin	strongest	LOOK 61
1131	Aromatic pyrone C-H out of plane deformation	The second more stronger	LOOK 61

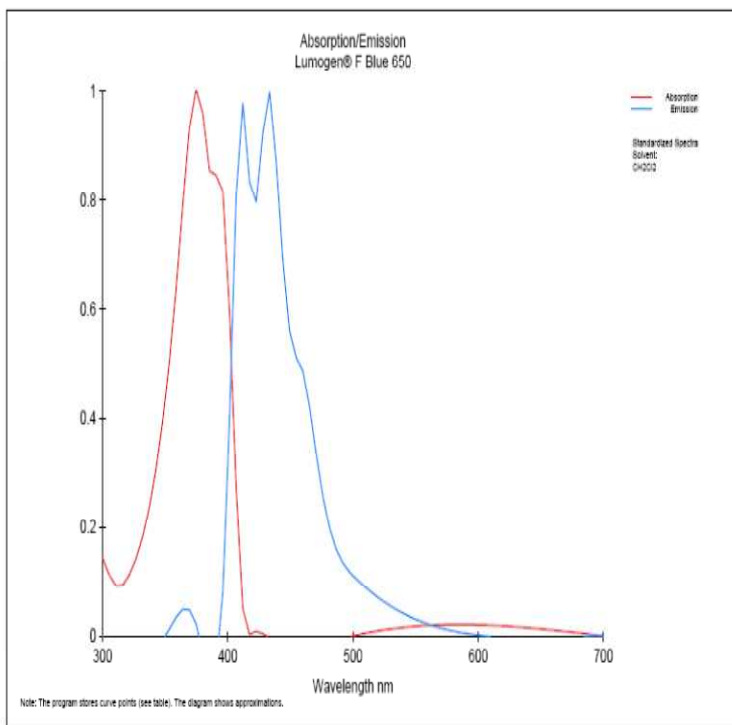
*Infrared Spectra*

1077	Aromatic pyrone C-H out of plane deformation	strong	LOOK 61
1034	Aromatic pyrone C-H out of plane deformation	medium	LOOK 61
989	CH in plane def aromatic		Know it All
896	Deflection 5H adjacent out of plane def		Know it All
776	5H adjacent	Strong I band	LOOK 61
758	4H adjacent		LOOK 61
703	5H adjacent	Strong II band	LOOK 61
689	Out of plane ring bend		Know it All

# APPENDIX B

## UV-Vis OPTICAL SPECTRA

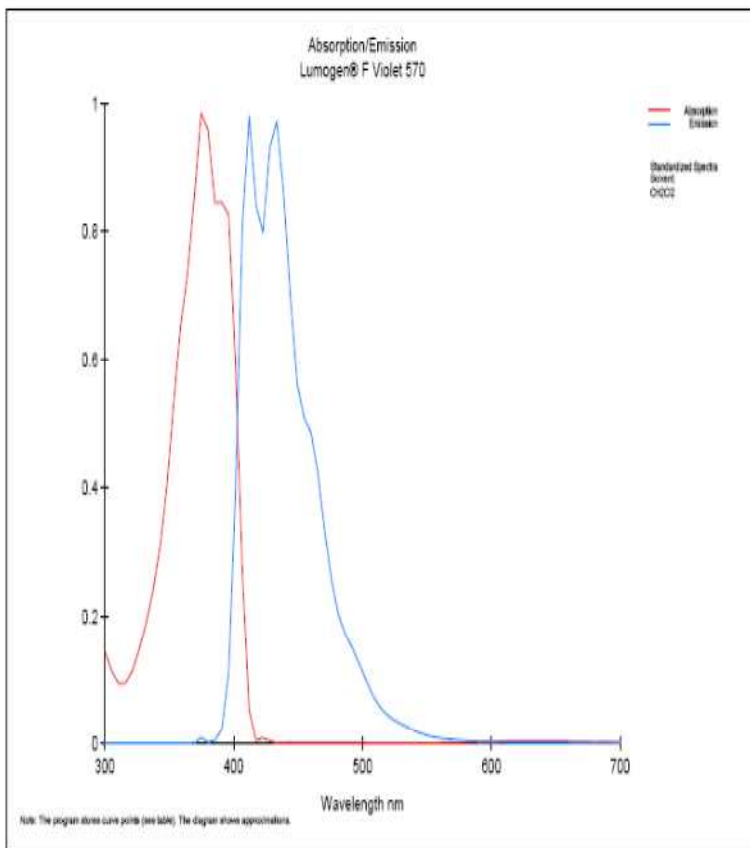
A presentation of Lumogen spectra from literature is provided.



All data is subject to the producer's disclaimer  
LUCOLOR® 3.1 - BASF Colorants for Plastics (Oct.2004) - Printed: 7.12.04

**Figure B.1: Absorption and emission spectra of Lumogen Blue [BASF 12]**

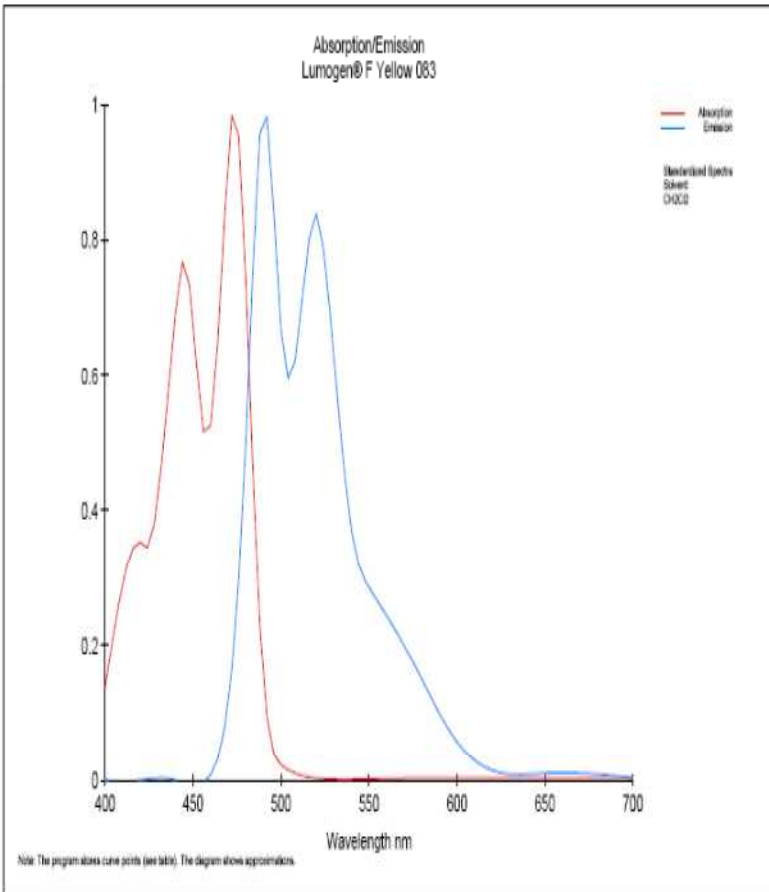
## UV-Vis Optical Spectra



All data is subject to the producer's disclaimer.  
LUCCO.DMSO.3.1 - BASF Colors for Plastics (201304) - Printed: 7/12/04

**Figure B.2: Absorption and emission spectra of Lumogen Violet [BASF 12]**

Appendix B

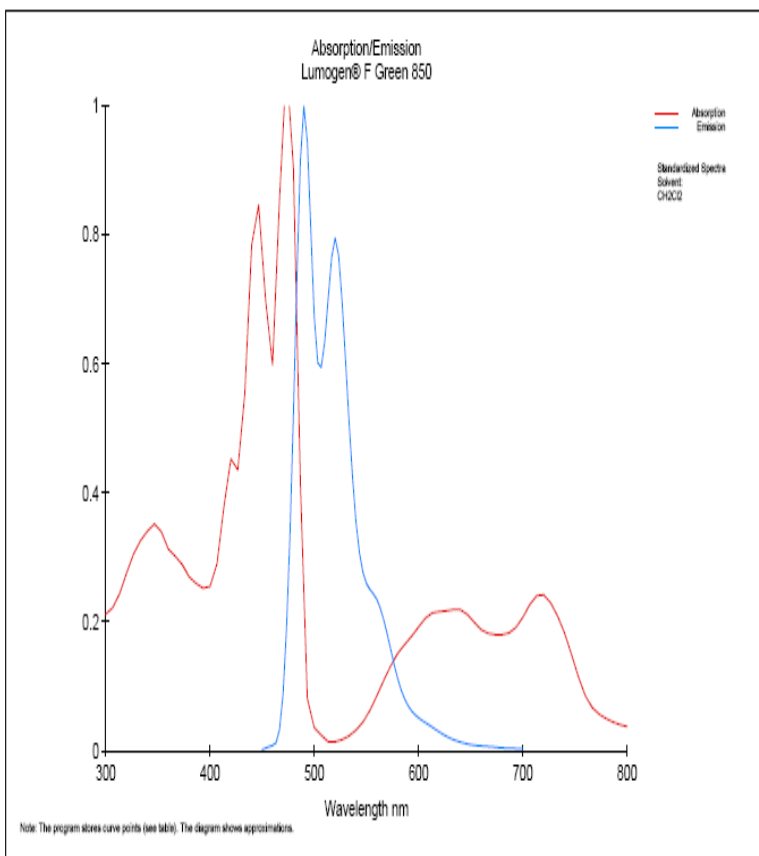


All data is subject to the producer's disclaimer.  
LUCOLON® 11 - BASF Chemicals for Plastics (Oct 2006) - Product 7.12.04

**Figure B.3: Absorption and emission spectra of Lumogen Yellow 083 [BASF 12]**

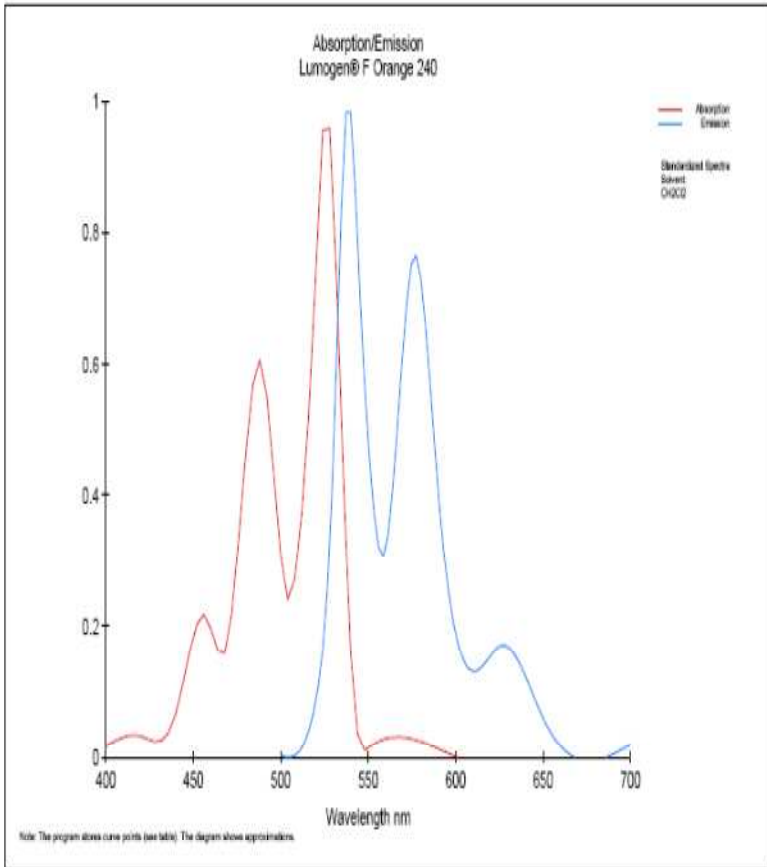


## UV-Vis Optical Spectra



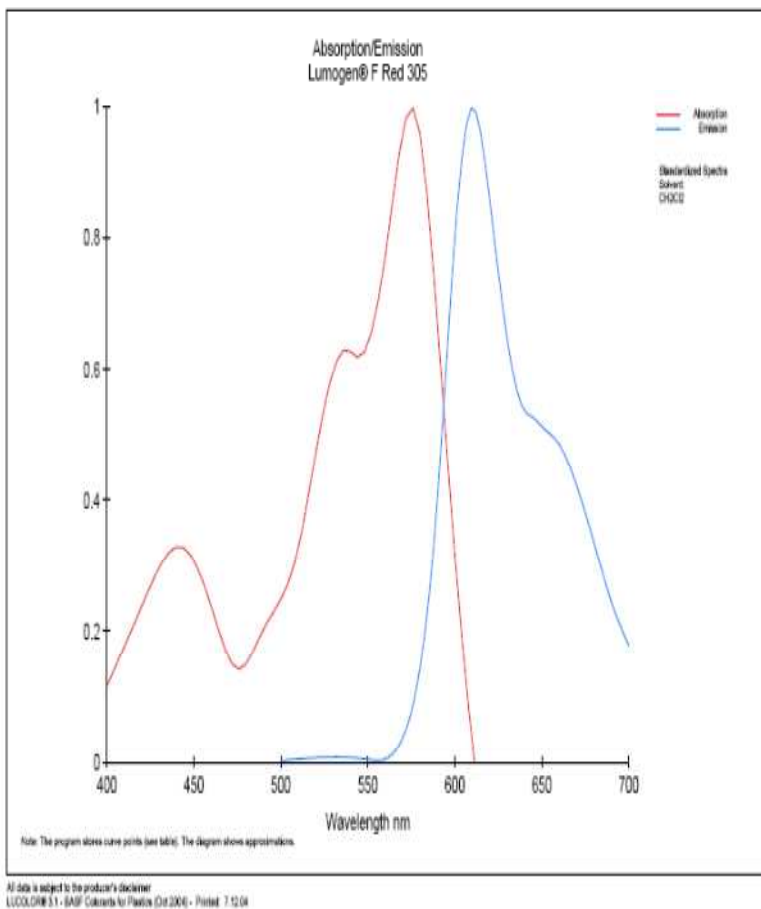
**Figure B.4: Absorption and emission spectra of Lumogen Green 850 [BASF 12]**

Appendix B



**Figure B.5: Absorption and emission spectra of Lumogen Orange 240 [BASF 12]**

## UV-Vis Optical Spectra

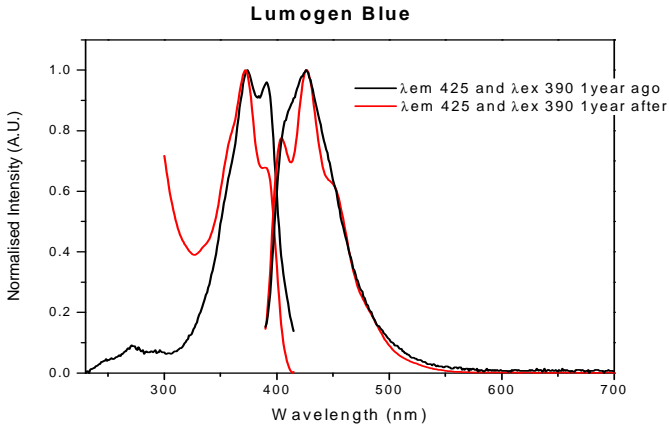


**Figure B.6: Absorption and emission spectra of Lumogen Red 305 [BASF 12]**

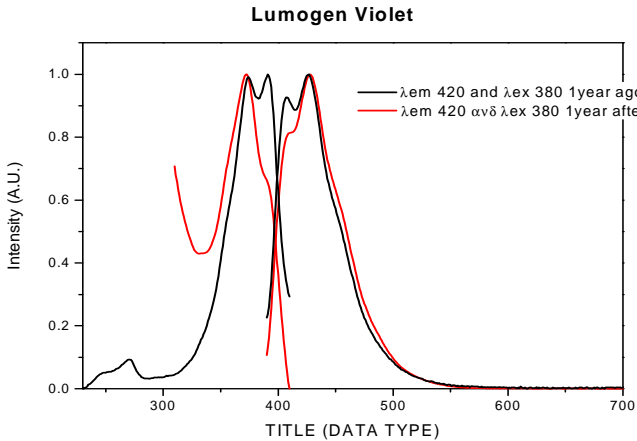
# APPENDIX C: UV-Vis SPECTRA OF LUMOGEN DYES IN POLYSILOXANE

---

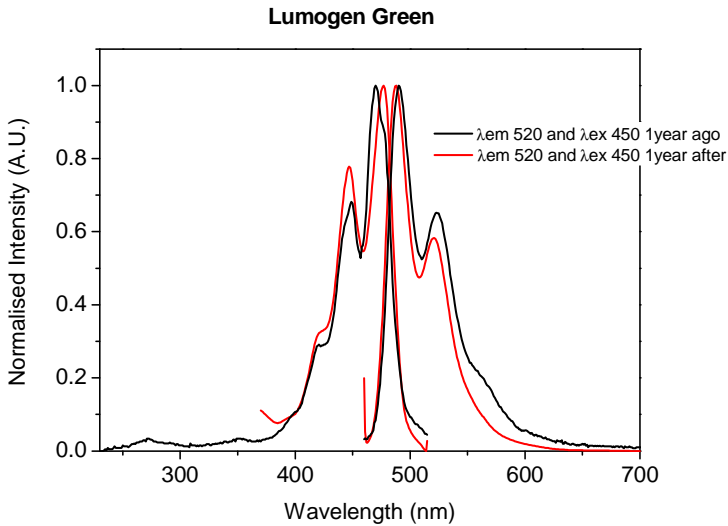
Some optical spectra of Lumogen in polysiloxane are here shown, recorded immediately after the synthesis and one year later. Those samples were never exposed to light so any change is due to an interaction between the dye and the Pt catalyst. All the spectra were normalized to their maximum peak.



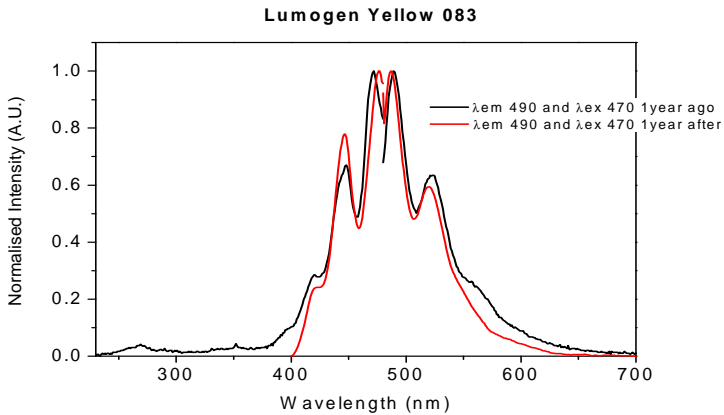
**Figure C.1:** excitation and emission spectra of Lumogen blue in polysiloxane just after polymerization and after one year.



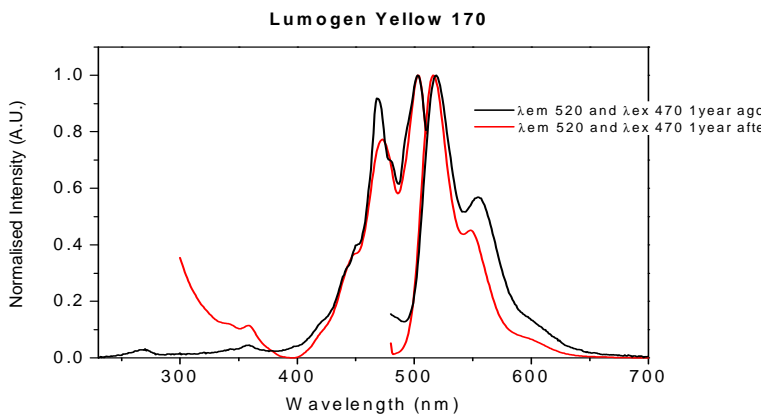
**Figure C.2:** excitation and emission spectra of Lumogen violet in polysiloxane just after polymerization and after one year.



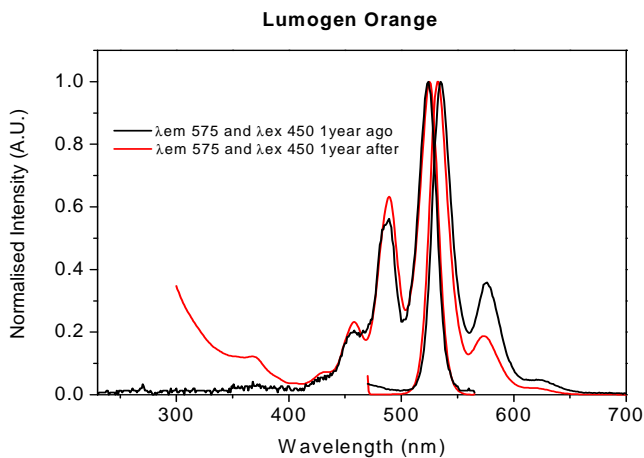
**Figure C.3:** excitation and emission spectra of Lumogen green in polysiloxane just after polymerization and after one year.



**Figure C.4:** excitation and emission spectra of Lumogen yellow 083 in polysiloxane just after polymerization and after one year.

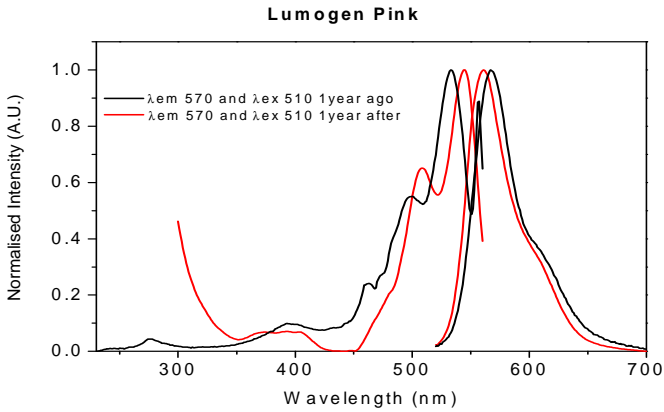


**Figure C.5:** excitation and emission spectra of Lumogen yellow 170 in polysiloxane just after polymerisation and after one year.

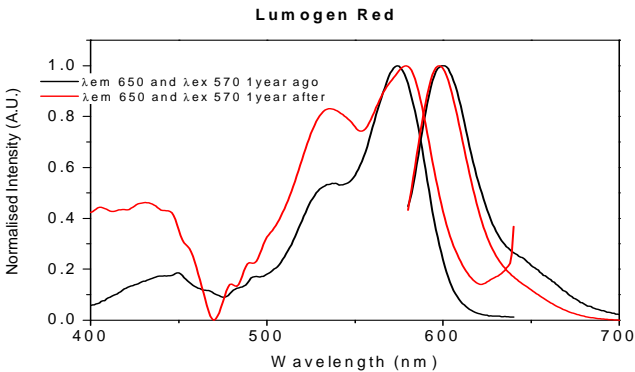


**Figure C.6:** excitation and emission spectra of Lumogen orange in polysiloxane just after polymerization and after one year.

## Appendix C



**Figure C.7: excitation and emission spectra of Lumogen pink in polysiloxane just after polymerization and after one year.**



**Figure C.8: excitation and emission spectra of Lumogen red in polysiloxane just after polymerization and after one year.**



## Bibliography

[KATR 59]

A. R. Katritzky, The infrared spectra of heteroaromatic compounds, *Q. Rev. Chem. Soc.*, 13 (1959) 353-373

[LOOK 61]

J.H. Looker, W.W. Hanneman, Physical and Chemical Properties of Hydroxyflavones. II. 3-Aroyl-5-hydroxyflavones. Synthetic and Infrared Spectral Studies, *J. Org. Chem.*, 27 (1962) 3261–3263

[VARV 08]

Andreas Vavra, Rolf Linder, Karl Kleinermanns, Gas phase infrared spectra of flavone and its derivatives, *Chemical Physics Letters* 463 (2008) 349–352

[wBAS 12]

[<http://www2.basf.us/additives/pdfs/p3201e.pdf> 30-01-2012, retrieved last 30/01/12

[wKNO 12]

<http://www.bio-rad.com>, retrieved last 12/03/12

Part of the present material was submitted for publication to the journals *Optical Materials* and *Solar Energy Materials and Solar Cells*:

- M. Buffa, S. Carturan, A. Quaranta, G. Maggioni, G. Della Mea, **”Spectral properties of 3-hydroxyflavone embedded in polysiloxane: Effects of the polymerization method”** *Optical Materials* 2012, v.34, p.1219–1224
- M. Buffa, S. Carturan, M. G. Debije, A. Quaranta, G. Maggioni, **”Dye-Doped Polysiloxane Rubbers for Luminescent Solar Concentrator Systems”** submitted to *Solar Energy Materials and Solar Cells* on February 2012

## **MARTA BUFFA:**

### **WORKS PUBLISHED IN PEER-REVIEWED JOURNALS**

#### **& CONFERENCE PROCEEDINGS**

- Carturan S., Tonezzer M., Quaranta A., Maggioni G., Buffa M., Milan R., "**Optical properties of free-base tetraphenylporphyrin embedded in fluorinated polyimides and their ethanol and water vapours sensing capabilities**", *Sensors and Actuators B: Chemical*, 2008, DOI: doi:10.1016/j.snb.2008.10.053
- Maggioni G., Carturan S., Tonezzer M., Buffa M., Quaranta A., Negro E., Della Mea G., "**Porphyrin-containing polyimide films deposited by high vacuum co-evaporation**", *European polymer journal*, 2008, v. 44, n. 12-13, p. 3628-3639.
- Quaranta A., Carturan S., Marchi T., Buffa M., Degerlier M., Cinausero M., Guastalla G., Gramegna F., Valotto G., Maggioni G., "**Doped polysiloxane scintillators for thermal neutrons detection**", *Journal of Non-Crystalline Solids*; DOI: 10.1016/j.jnoncrysol.2010.10.043
- M. Buffa, S. Carturan, A. Quaranta, G. Maggioni, G. Della Mea," **Spectral properties of 3-hydroxyflavone embedded in polysiloxane: Effects of the polymerization method**" *Optical Materials* 2012, v.34, p.1219–1224
- M. Buffa, S. Carturan, M. G. Debije, A. Quaranta, G. Maggioni;" **Dye-Doped Polysiloxane Rubbers for Luminescent Solar Concentrator Systems**" subittet to *Solar Energy Materials and Solar Cells* on February 2012
- G. Maggioni, M. Tonezzer, S. Carturan, A. Quaranta, M. Buffa, A. Antonaci, G. Della Mea; **Novel Wavelength-Shifting Materials for Improving Solar Cells Efficiency**; 24th European Photovoltaic Solar Energy Conference, 21-25 September 2009,

Hamburg, Germany; 621 – 623; doi: 10.4229/24thEUPVSEC2009-1DV.4.28

- M. Buffa, S. Carturan, G. Maggioni, M. Tonezzer, W. Raniero, A. Quaranta, G. Della Mea; **Effect of Wavelength-Shifting 3HF-Based Films on Solar Cells Yield**; 25th European Photovoltaic Solar Energy Conference and Exhibition / 5th World Conference on Photovoltaic Energy Conversion, 6-10 September 2010, Valencia, Spain; 763 – 766; doi: 10.4229/25thEUPVSEC2010-1DV.3.95

### **WORKS PUBLISHED IN THE LEGNARO NATIONAL LABS ANNUAL REPORT**

- **Novel Wavelength-Shifting Materials for Improving the Efficiency of Solar Cells**  
M. Buffa, G. Maggioni, S. Carturan, A. Quaranta, M. Tonezzer, G. Della Mea (2009)
- **Novel Materials for Luminescent Solar Concentrators**  
M. Buffa, S. Carturan, G. Maggioni, A. Quaranta, M. Tonezzer, G. Della Mea (2009)
- **Porphyrin-Containing Polyimide Films Deposited by High Vacuum Co-Evaporation**  
G. Maggioni, S. Carturan, M. Tonezzer, M. Buffa, A. Quaranta, E. Negro, G. Della Mea (2008)
- **Meso-tetraphenylporphyrin embedded in soluble fluorinated polyimides as optical vapour sensors**  
S. Carturan, A. Quaranta, G. Maggioni, M. Buffa, M. Tonezzer, R. Milan, G. Della Mea (2007)

## **POSTER SESSIONS**

- ❖ Conference: EUPVSEC Valencia 2010  
**Effect of wavelength-shifting 3hf-based films on solar cells yield**

M. Buffa, S. Carturan, G. Maggioni, M. Tonezzer, W. Raniero, A. Quaranta, G. Della Mea;

- ❖ Conference: EMRS Nice 2011  
**Encapsulation of in-gap solar cells with luminescent coatings improving the conversion efficiency**

M. Buffa, G. Maggioni S. Carturan, A. Quaranta.;

- ❖ Conference: EMRS Nice 2011  
**Dye-doped polysiloxane rubbers for luminescent solar concentrators systems**

M. Buffa, S. Carturan, M.G.Debije, P.C. Verbunt, G. Maggioni, A. Quaranta

*26<sup>th</sup> April 2012*

*I would now like to express my gratitude to Dr Sara Carturan who, although not formally a supervisor of mine, provided me with countless technical suggestions and plenty of advice and support throughout the whole length of this project. It is entirely fair to describe her contribution to this work as invaluable.*

*Marta*